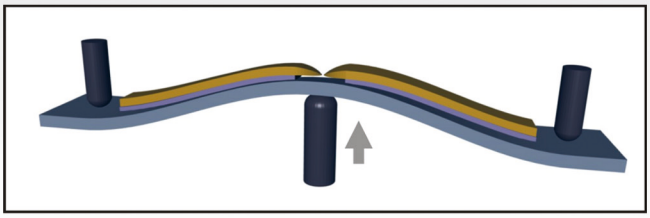

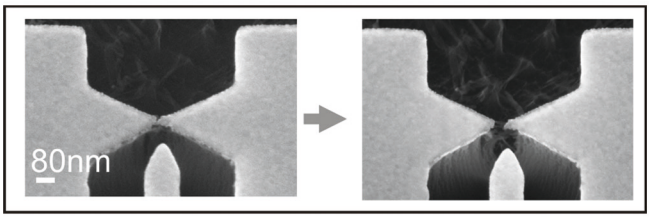

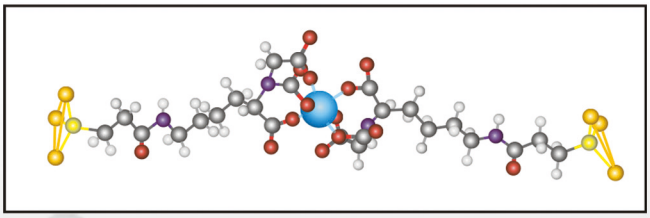

Fabrication and Utilization of Mechanically Controllable Break Junction for Bioelectronics

Dong Xiang

Mitglied der Helmholtz-Gemeinschaft

JÜLICH
FORSCHUNGSZENTRUM

Schriften des Forschungszentrums Jülich
Reihe Schlüsseltechnologien / Key Technologies Band / Volume 36

Forschungszentrum Jülich GmbH
Peter Grünberg Institute (PGI)
Institute of Complex Systems (ICS)
Bioelectronics (PGI-8/ICS-8)

Fabrication and Utilization of Mechanically Controllable Break Junction for Bioelectronics

Dong Xiang

Schriften des Forschungszentrums Jülich
Reihe Schlüsseltechnologien / Key Technologies Band / Volume 36

ISSN 1866-1807 ISBN 978-3-89336-769-6

Bibliographic information published by the Deutsche Nationalbibliothek.
The Deutsche Nationalbibliothek lists this publication in the Deutsche Nationalbibliografie; detailed bibliographic data are available in the Internet at http://dnb.d-nb.de.

Publisher and Distributor:	Forschungszentrum Jülich GmbH Zentralbibliothek 52425 Jülich Phone +49 (0) 24 61 61-53 68 · Fax +49 (0) 24 61 61-61 03 e-mail: zb-publikation@fz-juelich.de Internet: http://www.fz-juelich.de/zb
Cover Design:	Grafische Medien, Forschungszentrum Jülich GmbH
Printer:	Grafische Medien, Forschungszentrum Jülich GmbH
Copyright:	Forschungszentrum Jülich 2012

Schriften des Forschungszentrums Jülich
Reihe Schlüsseltechnologien / Key Technologies Band / Volume 36

D 82 (Diss., RWTH Aachen University, 2012)

ISSN 1866-1807
ISBN 978-3-89336-769-6

The complete volume is freely available on the Internet on the Jülicher Open Access Server (JUWEL) at http://www.fz-juelich.de/zb/juwel

Abstract

In scope of this work, a mechanically controllable break junction (MCBJ) setup was established and used for the investigation of electron transport properties of molecules in four related aspects.

The main feature of MCBJs, fabricated here, is their impressive stability. Spring steel substrates with a length of 44 mm and a width of 12 mm were used for the fabrication of the MCBJ chips. Electrode structures containing a thin suspended bridge with a constriction of 30-50 nm were defined by e-beam lithography. In this way, an attenuation factor of $r \approx 5 \times 10^{-6}$ between the displacement of the push rod and the variation of the gap distance was achieved for our set up. Due to the remarkable attenuation factor, the gap distance between two nano-electrodes can be controlled with sub Angstrom accuracy. The MCBJ was used for the investigation of the electronic properties of molecules. Four critical characteristics of electron transport in the molecular junction were investigated.

1. Noise measurement of single molecule junctions: The characterization of noise is an imporant issue for any kind of nano device, including those based on single molecules, since noise influences the performance and the reliability of future devices. The noise studies allow not only understanding the sources of noise but also give insight into dynamic electron transport processes.

   We studied the noise spectra of molecule-free and molecule-containing mechanically controllable break junctions. Both types of junctions revealed typical $1/f$ noise at different distances between the contacts. An additional Lorentzian-shape ($1/f^2$) noise component was registered only when nanoelectrodes were bridged by individual molecules. The noise properties strongly depend on the electronic structure of the molecules, but are independent of the bonding group. We propose a phenomenological model that correlates the charge transport

via a single molecule with reconfiguration of its coupling to the metal electrodes in order to explain the noise properties.

2. Gap size dependent of electron transport in single molecule junctions: The transport mechanisms are of fundamental importance for application of molecule electronics. In this thesis, charge transport at the single molecule level was investigated and enhaced field emission was observed at high bias. Previously, enhanced field emission was attributed to intermolecular charge transport. Surprisingly, although the interaction between parallel molecules is un-probable in the single molecular junction, enhanced field emission transport was observed as the molecular junction was compressed. I-V measurements with different numbers of molecules in the junction at a given gap size revealed that intermolecular electron transport between adjacent molecules was of minor importance to the electron transport mechanism and molecules can be considered as individual transport channels. Our observations indicate that the distance change between the electrodes and associated alternations of the molecular electronic structure rather than inter-molecules tunneling result in the enhancement of field emission.

3. Molecular junction based on ion coupling: Metal ions play a crucial role, for instance in biological charge transport. It is of fundamental interest to investigate if, and how, metal ions influence electron transport on the level of individual molecules. However, little is known about electron transport via metal ions trapped between ligand molecules.

   Here, metal-molecule-ion-molecule-metal junctions on the single molecule level were realized by mechanically controllable break junction experiments. For the first time, we show the influence of different metal ion species in a system where the ligands remain essentially unchanged. We demonstrate that the conductance of the junctions depends strongly on the kind of integrated metal ion in the order: $Ca^{2+} > Zn^{2+} > Ni^{2+}$.

4. DFT based calculation: To further verify our observation, density functional theory (DFT) calculations were performed with a dmol^3 simulation package. The DFT calculations determined the wave function intensity of the highest occupied molecular orbital (HOMO) and the lowest unoccupied molecular orbital (LUMO). The obtained order of the energy gap value in three types of junctions agreed well with the experimental data.

Kurzfassung

In dieser Arbeit wurde ein mechanisch kontrollierbarer Bruchkontaktaufbau (mechanically controllable break junction = MCBJ) entwickelt und für die Untersuchung von vier Aspekten des Elektronentransports von Molekülen benutzt.

Das Hauptmerkmal der hier hergestellten MCBJ ist deren beeindruckende Stabilität. Federstahlsubstrate mit einer Länge von 44 mm und einer Breite von 12 mm wurden für die Herstellung der MCBJ Chips verwendet. Durch Elektronenstrahllitographie wurden dünne Brücken mit einer Verengung von 20 bis 50 nm definiert. Um eine echte Brückenstruktur zu erreichen, wurde die Isolatorschicht unter dem Metall durch reaktives Ionenätzen entfernt. Auf diese Weise erzeugt man an dieser Stelle einen Dämpfungsfaktors, der durch das Verhältnis zwischen der Schubstange (Push Rod) - Verschiebung und dem dadurch variierenden Spaltabstand zwischen den Elektroden $r \approx 5 \times 10^{-6}$ definiert ist. Aufgrund des bemerkenswerten Dämpfungsfaktors kann die Lücke zwischen zwei Elektroden mit einer Genauigkeit im (sub-Angström)-Bereich kontrolliert werden. Die MCBJ wird für die Untersuchung der elektronischen Eigenschaften von Molekülen verwendet. In den folgenden vier Abschnitten werden die untersuchten Charakteristika des Elektronentransportes in der molekularen Verbindung zusammengefasst.

1. Rauschmessung an den Metall-Molekül-Metall-Brücken: Die Rauschcharakteristik hat eine zentrale Bedeutung für jede Art von elektrischen Bauelementen; einschließlich solche, die auf Basis von einzelnen Molekülen fungieren, da sie die Leistungsfähigkeit und die Zuverlässigkeit der Bauelemente beeinflussen.

Wir untersuchten die Rauschspektren von Molekül-freien und Molekül-haltigen MCBJ. Beide Arten von Verbindungen zeigten typische reziproke Rauschcharakteristika in unterschiedlichen Abständen zwischen den Kontakten. Der zusätzliche Rauschanteil in der Lorentz-Form $(1/f^2)$ wurde nur bei Nanoelektroden registriert, wenn diese durch individuelle Moleküle überbrückt

werden. Die Rauscheigenschaften hängen stark von der elektronischen Struktur der Moleküle ab und sind völlig unabhängig von der Bindungsgruppe. Das wurde zum ersten Mal im Rahmen dieser Arbeit nachgewiesen. Wir haben ein phänomenologisches Modell aufgestellt, das die Korrelation zwischen dem Ladungstransport eines einzelnen Moleküls und der Kopplung mit der Metallelektrode herstellt, um die Rauscheigenschaften zu erklären.

Diese Untersuchungen erlauben nicht nur ein Verständnis der Rauschquellen, sie geben auch Einblick in die dynamischen Prozesse des Elektronentransportes in der Verbindung.

2. Elektronentransport in einzelnen Molekülverbindungen in Abhängigkeit von der Spaltgröße: Der grundlegende Transportmechanismus ist von elementarer Bedeutung für die Anwendungen in der Elektronik sowie für mögliche zukünftige Bauelementherstellung. In dieser Arbeit wurde der Ladungstransport auf Einzelmolekülebene durch die hohe Stabilität der MCBJ untersucht und verstärkte Feldemission für hohe Spannungen gefunden. Bisher wurde die verstärkte Feldemission durch intermolekularen Elektronentransport erklärt. Obwohl die Wechselwirkung zwischen parallelen Molekülen innerhalb der einzelnen Verbindungsstelle unwahrscheinlich ist, konnte überraschend ein erhöhter Feldemissionstransport beobachtet werden, wenn die molekulare Verbindungsstelle komprimiert wird. IV-Messungen mit einer unterschiedlichen Anzahl von Molekülen in der Verbindung bei einer gegebenen Größe der Spaltverbindung ergab, dass der Elektronentransport zwischen den Molekülen von untergeordneter Bedeutung für den Elektrontransportmechanismus ist, denn Moleküle können somit als individuelle Transportkanäle angesehen werden.

Unsere Beobachtungen deuten darauf hin, dass die Abstandsänderung zwischen den Elektroden und die damit einhergehende Änderung der molekular-elektronischen Struktur viel mehr Einfluss auf die Verstärkung der Feldemission hat als das intermolekulare Tunneln.

3. Molekulare Verbindung basierend auf Ionenkopplung: Metallionen spielen eine entscheidende Rolle im biologischen Ladungstransport. Es ist von fundamentalem Interesse zu untersuchen, ob und wie Metallionen den Elektronentransport auf der Ebene einzelner Moleküle beeinflussen. Allerdings ist nur wenig über den Elektronentransport mit Hilfe von Metall-Ionen, die zwischen Ligandenmoleküle eingeschlossen sind, bekannt.

Es wurden Metall-Molekül-Ion-Molekül-Metall-Übergänge auf der Ebene einzelner Moleküle durch die MCBJ-Experimente realisiert. Zum ersten Mal wurde der Einfluss verschiedener Metall-Ionen auf die Leitfähigkeit untersucht; dabei blieben die Liganden hauptsächlich unverändert. Wir konnten zeigen, dass die Leitfähigkeit der Verbindungen stark von der Art der integrierten Metall-Ionen abhängt. Die Reihenfolge der Stärke lautet wie folgt: $Ca^{2+} > Zn^{2+} > Ni^{2+}$.

Zur weiteren Überprüfung der Ergebnisse wurden Simulationen nach der Dichtefunktionlatheorie (DFT) durchgeführt. Dabei wurde das Paket dmol³ mit einer lokalen Näherung der Zustandsdichte (engl. local density approximation, LDA) verwendet. Mit den DFT Simulationen wurden die Werte der Wellenfunktion für das höchste besetzte (engl. highest occupied molecular orbital, HOMO) und das niedrigste unbesetzte Molekülorbtal (engl. lowest unoccupied orbital, LUMO) berechnet. Die errechnete Größenordnung der Bandlücke stimmt sehr gut mit den gemessenen Werten überein.

Acknowledgements

First and foremost I want to thank my advisor Aandreas Offenhäusser. As the head of the institution, he takes part in the every group seminar monthly and offers helpful suggestion for each student. The passion he possesses for the research is contagious and motivational for me, even during tough times of PhD pursuit. The harmonious academic atmosphere and efficient incentive mechanism guided by him is essentially important for me to achieve the goal. The financial support and advanced equipments provided by Offenhäusser guarantee the quality of my scientific research.

Second, I would like to thank our group leader Dirk Mayer. It has been an honor to be a student directly supervised by him. I deeply appreciate all his contributions of, time, profound knowledge and creative ideas to make my PhD experience interesting and productive. The excellent qualities of what a real scientist should possess he has shown to me will benefit my whole academic life.

The Mayer group members have contributed immensely to my personal and professional time at the research center. The group has been a source of friendships as well as collaboration and inspiration. I am especially grateful to the members who argued and debated with me about scientific issues: Zhiwei Yi, Niles Sanetra, Yaqing Liu and Pinggui Li. I would like to acknowledge Martina who provided me with peptides for the biomolecules investigation. I appreciate Jenifer Hou and Vivian Feig who help me to polish my papers and thesis. I would also thank other former and present group members such as Gilles Sandra, and Feliks Pyatkov. Their enthusiasm, intensity, and amazing ability to carry out the experiments set good example for me. It is my pleasure to work with all of them.

In regards to quantized conductance measurements, I appreciate Prof. Yi Zhang, for the nice suggestion to reduce noise level and stabilize the setup. Concerning the noise measurements,

Sydoruk Viktor wrote a spectrum analyzer program and shared the noise measurement with me. I thank to Vitusevich Svetlana who provided a scientific model to describe G-R noise. I thank Niculina Peica for her complete supporting in the tip enhanced Raman scattering (TERS) measurements. I would also like to acknowledge the clean room facility and electronic shop of IPG-8, where I fabricated the chips and electronic circuits.

I deeply acknowledge financial support from the joint scholarship program of the Helmholtz association and the Chinese scholarship council for my fist 3 years. I'm greatly indebted to Prof. Offenhäusser for the additional funding support during the extended half year. I also acknowledge the full support from China University of Geosciences (CUG), epically the department of mathematics and physics in CUG. Without their help, it would be hard to figure out how to finish up my PhD degree.

My time at research center is made enjoyable in large part due to the many friends that had become part of my life. I am grateful for the time spent with roommates and colleagues, for our memorable trips into the mountains, for our interaction in Christmas party, for Niles and Sandra's hospitality as I finished up my degree. My time at research center is also enriched by the federation of Chinese students and scholars, the football team of Juelich, and the table tennis club of research center.

Last, I would like to thank my family for all their encouragement and supports. My parents who raised me with a love of science make a strong backup in all my pursuit. My son Boyuan Xiang accompanies me at Juelich for two month every year. And most of all, I would like to thank my encouraging, patient, and loving wife Qingling Wang whose faithful support during the last four years is so appreciated. Thank you.

Dong Xiang
RWTH Aachen University
November 2011

Contents

Chapter 1

Introduction

With the rapid development of semiconductor technologies, the feature size of the transistors has been reduced to below 50 nm and is gradually approaching the miniaturization limits of silicon technology. The dream of utilizing molecules as functional units in electronic circuits has motivated many researchers for years. As early as 1974, Aviram and Ratner had predicted that individual molecules would someday be used as circuit elements in devices.[1] Today, a single molecule represents the ultimate limit that we can be handled.

The major challenge to the goal of building electronic devices using individual molecules is the ability to measure and control electrical current through a molecule.[2] The prerequisite is to integrate nanometer sized molecules to macroscopic electronic circuits and reproducibly control the molecule-metal interface. There are mainly two approaches for bridge electrodes with molecules. One method is to make top-contact junctions, which includes scanning probe microscopy (scanning tunneling microscopy or conducting atomic force microscopy), cross junctions (cross wire or cross bar), mercury drop electrodes, and nano pore.[3-6] The second way utilizes vertical nanogap electrodes to form metal/molecule/metal juctions.[7-10]

The method to fabricate nanogap electrodes include, mechanical controllable break junctions, electrochemical deposition of nanogap electrodes, electromigration breakdown method.[11-14] Among these methods, only the mechanically controllable break junction (MCBJ) technique, which was invented by J. Moreland and J.W. Ekin in 1985, and further developed by C. Muller in 1988-1992, offers a tunable gap between the two electrodes with additional mechanical

stability, and supply two uncontaminated atom-size nanoelectrodes to characterize even single molecules.[15-22]

Therefore, our first step is to fabricate nano-sized pairs of electrodes by means of mechanical break junction experiments. Different methods, such as electrochemical etching, mechanical cutting and electron beam lithography were tested in order to fabricate chips fitted to the MCBJ setup. Finally, the method of electron beam lithography was chosen to fabricate the chips because of the best stability of the chips. After the chips were well fabricated, individual molecules were integrated into the pairs of electrodes and the electron transport properties of molecule junctions were determined.

The noise characterisation of the molecular junction was first investigated. The characterization of noise is a key issue for any kind of nano devices, including those based on single molecules. Noise properties influence the performance and the reliability of the devices. The noise studies allow not only understanding of the noise sources and providing useful information for improvement of the system and optimization of the performance of the molecule-based devices, but also give insight on dynamic electron transport processes[23-29]

The noise properties of single molecular junction have been investigated by Weber *et al*.[30] In their MCBJ experiment, the Generation-Recombination (G-R) noise was first observed in the single molecular junction. However, the dependence of G-R noise on the binding group and electronic properties of integrated molecules had never been revealed, hence the original source of G-R noise remains unclearly. In this thesis, the noise properties of single molecule junctions were systematically investigated with different kinds of molecules. The relationship between the characterization frequency of G-R nose and the electronic structure of the molecules was revealed. Based on this observation, a model that can explain the source of G-R noise was proposed.

Subsequently, the electron transport pathway of the molecular junction was investigated. The study of electron transport through a metal-molecule-metal junction has been an active area of research for more than a decade now. The underlying transport mechanisms are of fundamental importance for electronic applications and future device fabrication. Many advances have been made in understanding the change of the charge transport mechanism from direct tunneling to

hopping when the molecular length exceeds a certain value.[31] However, possible changes of the transport pathway at short tunneling distances are still under controversial discussion and require clarification.[32-34] For example, by means of transition voltage spectroscopy (TVS), Lee *et al* found that the transition voltage (from directly tunneling to field emission) shifts to lower voltage as the sandwiched molecules were compressed. Lee attributes it to the changed transport pathway between parallel molecules.[35] However, Kushmerick *et al* demonstrate in the cross wire experiments that molecular wires connected in parallel are not strongly coupled along their back bone, and single molecules can be considered as independent conductance channels.[33] This thesis sheds light on this question and contributes to the ongoing discussion about the role of intra-molecular and inter-molecular charge transport pathways of short molecules.

Finally, a more complicated molecular junction (metal-molecule-ion-molecule-metal) was investigated. Metal complexes play an important role in many biochemical processes. For instance respiration (hemoproteins), and photosynthesis are based on charge transport via metal complexes.[36,37] In these systems, the charge transport depends on the nature of ligands but also on the kind of metal ion trapped in the complex.[38,39] Therefore, it is of fundamental interest to understand how metal ions are influencing electron transport on the level of individual molecules. With the increase of atomic number and the positive charge of the metal ion the stability of metal complex will increase. Here, we investigated the influence of metal ion species on conductivity while leaving the ligands mainly unchanged. The observed relation between the type of the metal ion and the conductivity of molecular junctions may help elucidate the biological charge transport mechanism and pave the way for novel design strategies for molecule based devices. To verify our observation, density functional theory (DFT) calculations were performed with the dmol^3 simulation package. The calculated order of the energy gap value in three types of junction agrees well with the experimental data.

The outline of this thesis is as follows: first I will introduce the theory and techniques used in this work, see Chapter 2. This will be followed by a description of the setup and materials employed, see Chapter 3. The results of these experiments and discussions will then be presented in Chapter 4, followed by the main conclusion and further outlook.

Chapter 2

Fundamentals and Method

2.1 Related Techniques for Nano-Fabrication

2.1.1 E-Beam Lithography

If one wants to make a structure smaller than 100 nm, it is not achievable by optical lithography The limitation resolution of the optical lithography is given by $d = \lambda / 2NA$. λ is wavelength of light. NA is numerical aperture of the objective lens. For example, if green light with λ of 550 nm is used, and the highest practical NA is 0.95 with air as medium, in practice the lowest value of d is about 200 nm, which is far away from requirement for the nano-structure fabrication.

Electron Beam Lithography (EBL) refers to a lithographic process that uses a focused beam of electrons to form the circuit patterns needed for material deposition on (or removal from) the wafer. In contrast to optical lithography, electron lithography offers higher patterning resolution than optical lithography. This is possible due to the very small focus spot size of the electrons beam whereas the resolution in optical lithography is limited by the wavelength of light used for exposure. The wavelength of an electron is given by the de Broglie relation ($\lambda = hc/E$), where h is the Planck constant, c is the velocity of light and E is the electron energy. For example, a 1 k eV electron has a wavelength of slightly less than 0.4 nm.[40]

The electron beam can obtain the energy of several hundred k eV from the electron beam exposure system and the corresponding de Broglie wavelength down to pm range. The electron beam has wavelength so small that diffraction no longer defines the lithographic resolution

anymore. Most direct writing systems use a focus electron beam to modify the resist, which is moved with respect to resist surface to expose often only one pixel at a time. Exposed area of the resist will change its properties due to the energy that is deposited.

Electron-Beam Exposure System

A typical EBL system consists of the following parts: 1) an electron gun or electron source that supplies the electrons. Usually, a electron gun is mounted at the top of an UHV chamber in order to maintain a collision free transport electron; 2) an electron column that 'shapes', deflect and focuses the electron beam; 3) a mechanical stage that positions the wafer under the electron beam; 4) a wafer handling system that automatically feeds wafers to the system and unloads them after processing; and 5) a computer system that is used to control the various machine subsystems and transfer pattern information to the beam deflection coils.

Direct writing systems normally can be classified as vector scan or raster scan. A commonly used vector scan is Gaussian vector scanning that means, a circular shaped beam with a Gaussian energy distribution is moved over the resist surface. Please note, only those area which should be exposed are scanned by the electron beam. While, in the raster scan mode, the whole resist surface are canned by the electron beam and the electron beam is blanked in the area where the resist should not be exposed.

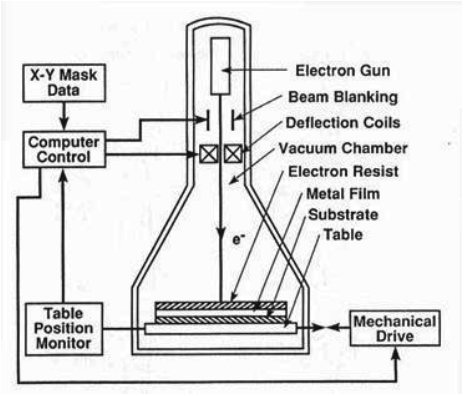

Figure 2.1: Schematic of an electron-beam exposure system[41]

The main parameters that determine the result of the EBL are: beam size, beam step size, acceleration voltage and dose. The beam size should be several times smaller than the structure size in order to define the pattern with sharp edges. The beam size is chosen to be $\sqrt{2}$ times the beam step size in order to expose every part of the design. The acceleration voltage supplies the energy to the electron and mainly defines the wavelength of the electron beam. The dose is the accumulated charge, which is brought into a certain area during the EBL process and measured in Coulombs/cm^2. The dose depends on the material properties and effect the electron beam write time.

An important phenomenon in electron beam lithography is the proximity effect. In the EBL process, the exposure dose distribution, and hence the developed pattern, is wider than the scanned pattern, due to the interactions of the primary beam electrons with the resist and substrate. These causes the resist outside the designed pattern receive a non-zero dose. Important contributions to resist polymer chain scission or cross linking come from electron forward scattering and backscattering. The forward scattering process is due to electron-electron interactions which deflect the primary electrons by a small angle, thus broadening the beam. These electrons can still contribute to resist exposure. The backscattering process originates from a collision with a heavy particle (for example substrate nucleus) and leads to wide angle scattering of the electron. Increase beam energy will reduce the forward scattering width, but since the beam penetrates the substrate more deeply, the backscatter width will increase, which will affects the practical resolution of the EBL process.

Electron Beam Resists

Electron beam resists are the recording and transfer media in the e-beam spin coating lithography process. The usual resists are polymers dissolved in a liquid solvent and can be stored at room temperature. After baking out the solvent, electron exposure modifies the properties of the resist. Like in optical lithography, e-beam resists are grouped into different types : positive tone resists (PTR) and negative tone resists (NTR).[42] For positive tone resists, the resists are removed at exposed regions whereas in the case of negative tone resist the developed region remains behind after development.

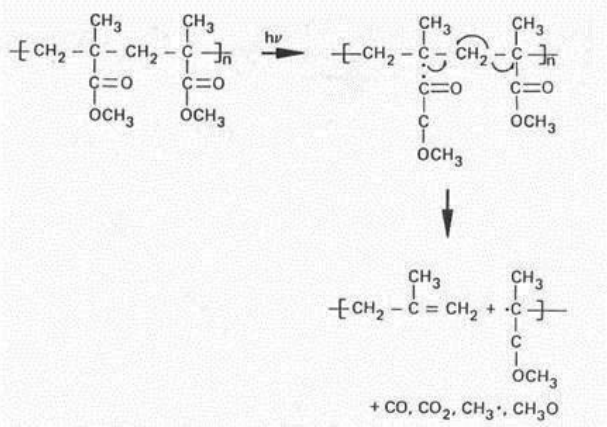

Figure 2.2: Mechanism of radiation-induced chain scission in positive e-beam resists. Electron beam exposure breaking the polymer into fragments. Taken from http:// dot.che. gatech. Edu / henderson/Introductions/intro to e-beam lithography. htm

When the resists is exposed to the high energy electron beam, the properties of resists will completely change. Positive e-beam resists undergo main-chain scission when exposed to e-beam as shown above (Figure 2.2) for polymethyl methacrylate (PMMA), which make it soluble in the develop process. Therefore, the exposed resists can be easily removed just by put the sample into the developer solution. On the other hand, negative tone e-beam resists function on the basis of radiation-initiated cross-linking reactions that result in the formation of inter-chain linkages. Thereby generate a cross-linked and three-dimensional network is generated, which is insoluble within the developing process.

Electron Beam Write Time

The minimum time to expose a given area at a given dose is given by the following formula[43]

$$D \cdot A = T \cdot I \tag{2.1}$$

where D is the dose, T is the time to expose the object, I is the beam current, and A is the area need to be exposed. For example, assuming an exposure area of 1 cm^2, a dose of 10^{-3} Coulombs/cm^2, and a beam current of 10^{-8}A, the resulting minimum write time would be 10^5

seconds (about 1 days). This minimum writing time does not include time for the stage to move backward and forth ward, as well as time for other possible beam corrections and adjustments in the process of writing. So there is a serious limitation for electron beam lithography, especially when writing dense patterns over a big area. Over a large area, optical lithography was normal used at the cost of lower resolution.

Physical Vapor Deposition (PVD)

Physical vapor deposition (PVD) is a general term used to describe any of a variety of methods to deposit thin films, such as Au and Ti, by the condensation of a vaporized form of material onto various surfaces, for instance, onto spring steel substrates. This kind of method involves purely physical processes such as high temperature vacuum evaporation or plasma sputtering rather than involving a chemical reaction at the surface as in chemical vapor deposition (CVD). The term physical vapor deposition appears originally in the 1966 book 'Vapor Deposition' by C.F Powell, J.H Oxley *et al* and is further developed by R.W. Marek *et al*. [44-46]

Electron beam physical vapor deposition (EBPVD) is one kind of PVD. In the EBPVD system, the deposition chamber is evacuated to a pressure of about 0.1 millitorr. The material to be evaporated is in the form of ingots. There are several electron guns, each having a power from tens to hundreds of kW. The generated electron beam is accelerated to a high kinetic energy and focused towards the material to be evaporated. When the accelerating voltage is high enough and the beam current is increased to a few amperes, most of the kinetic energy of the electrons is converted into thermal energy as the beam bombards the surface of the ingot. The surface temperature of the ingot increases dramatically resulting in the formation of a liquid melt. The liquid ingot material evaporates under such vacuum.[47]The evaporated atoms of ingot material then precipitate into solid form, coating everything in the vacuum chamber.

2.12 Reactive Ion Etching (RIE)

The reactive ion etching is one kind of dry etching. The purpose of dry etching is to create an anisotropic etch, which means the etching is unidirectional. The figure below shows a diagram of a common RIE setup. An RIE system contain of two electrodes (1 and 4) as shown in figure 2.3 that create an electric field for acceleration of charged .

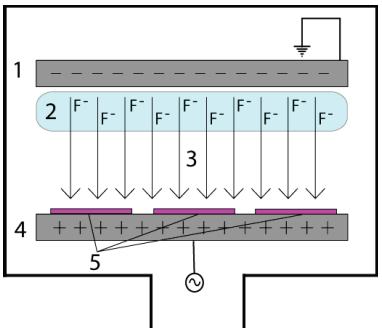

Figure 2.3: Diagram of a common reactive ion etching setup
Taken from http://cleanroom.byu.edu/rie_etching.phtml

The area labeled (2) represents the plasma area that contains both positively and negatively charged ions in equal quantities. These ions are generated from the gas that is pumped into the chamber. In the diagram CHF_3 has been pumped into the chamber, making plasma with many negative ions (F^-). Plasma is initiated in the system by applying a strong radio frequency electromagnetic field to the wafer platter. The field is typically set to a frequency of several megahertz, applied at a few hundred watts. The oscillating electric field ionizes the gas molecules by stripping their electrons, creating plasma. The negative ions are accelerated in the area of (3) toward the surface of the samples (5).

A hard mask (usually a metal layer) is used to protect certain areas from etching, exposing only the areas desired to be etched. The etching process in brief is like this: fluorine ions are accelerated in the electric field and collide into the etching region, where they combine with material atoms to be etched and dispersed. Because the electric field accelerated ions toward the surface in one direction, the etching caused by these ions is much more dominant than the etching because of radicals, thus the etching is anisotropic.

2.1.3 Nano Structure Image Measurement

For a faithful imaging of the nano structure, basically two method can be applied: Scanning Electron Microscope (SEM) and Scanning Pobe Microscopy (SPM) can be applied. SEM has the advantage, that sample can be moved freely in x, y, z direction as well as rotated or tilted. The

disadvantage is that the sample has to be electrically conductive. Therefore, the insulating sample has to be coated with metal layer if a high quality picture is required.

The main advantage of SPM, including AFM and STM is that they allow measuring a height profile with sub-nanometer resolution in the Z direction. In the X-Y scan direction molecular resolution can be achieved also. The shortcoming is that just a small section of the sample can be scanned (e.g. ten by ten micron area) with high resolution, since such a scan may take several minutes. While it takes a few seconds with SEM.

Scanning Electron Microscope (SEM)

The SEM is a novel microscope that uses electrons instead of light to form an image. The SEM has allowed researchers to examine a much bigger variety of specimens with high resolution. As shown in figure 2.4, a beam of electrons is produced similar to EBL at the top of the microscope by an electron gun. The electron beam normally follows a vertical path through the microscope, which is held within a vacuum. Then the beam travels through electromagnetic fields and lenses, which focus the beam down toward the sample. Once the beam hits the sample, Auger electrons, secondary electrons, back scatter electrons and X-rays are ejected from the sample.

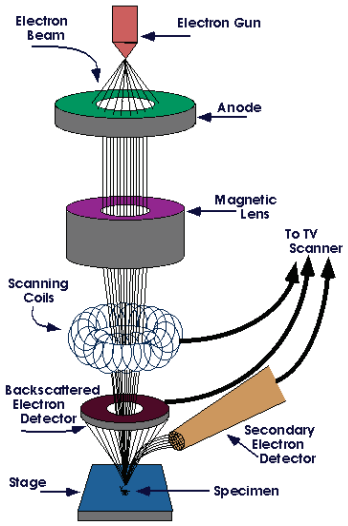

Figure 2.4: Configuration of the SEM system[48]

The so called secondary electrons are the electron, which ejected from the specimen atoms by inelastic scattering interactions with beam electrons. Because of their low energy, these electrons originate within a few nanometers from the sample surface and can be used to produce SEM images.. The secondary electrons are detected by the secondary electron detector which is normally a type of scintillator-photomultiplier system. The amplified electrical signal output by the photomultiplier is displayed as a two-dimensional intensity distribution that can be viewed and photographed on an analogue video display or saved as a digital image.

The principle to obtain topography using the secondary electron is like this: the brightness of the signal depends on the number of secondary electrons reaching the detector. The number of secondary electrons dependents on the angle between the incidence beam and sample surface. For example, if the beam enters the sample perpendicular to the surface, then the activated region is uniform along the axis of the beam and a few numbers of electrons "escape" from the sample. As the angle of incidence beam increases, the "escape" distance of one side of the beam will decrease, then more secondary electrons will be emitted. Therefore steep surfaces and edges tend to be brighter than flat surfaces. Before, the beam moves to its next dwell point these instruments count the number of second electrons and display a pixel on a Crystal Ray Tube whose intensity is determined by this number (the more reactions the brighter the pixel). This process is repeated until the grid scan is finished. After the beam scanning the whole surface of the sample, an image with a well-defined, three-dimensional is generated. With such technique, image resolution less than 0.5 nm is possible.[49]

The so called back-scattered electrons (BSE) represent high-energy electrons that are reflected from the sample by elastic scattering. Since heavy elements (high atomic number) backscatter electrons more strongly than light elements (low atomic number), and thus appear brighter in the image. Because the intensity of the BSE signal is strongly related to the atomic number and the element of the specimen, BSE images can provide information about the distribution of different elements in the sample, hence are used to determine crystal structures and orientations of minerals.

Atomic Force Microscopy (AFM)

A standard AFM contains a microscopic tip (curvature radius of ~10-50nm) attached to a cantilever spring. The underlying principle of AFM is the detection of the bending of this cantilever spring as a response to external forces. In the case of adhesive interaction between the tip and a surface, the forces are normally very small in the order 0.1 - 1 nN. In order to measure such small forces one must use not only very sensitive force-measuring springs but also very sensitive ways for measuring their bending.

The stiffness of the cantilever are mainly determined by the value of thin and length, which are designed enable the cantilever very sensitive to the applied force. In the AFM system, a laser beam is focused on the back of the cantilever in order to detect this bending, which is as small as 0.01 nm, see figure 2.5. From the cantilever, the laser beam is reflected towards a position-sensitive photo-detector. Depending on the cantilever deflection the position of the reflected beam changes. In such a way, the deflection of the cantilever is amplified. The photo-detector converts this change into an electrical signal. To acquire a surface image the AFM tip is brought down to the surface and a Piezo actuator is used to scan the tip line by line across the sample surface.

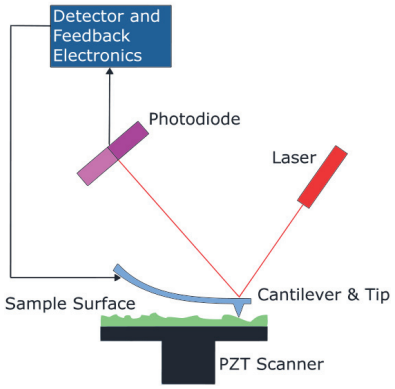

Figure 2.5: Diagram of atomic force microscope. [a]

[a] Taken from http://en.wikipedia.org/wiki /Atomic_force_microscopy.

Basically two different operation modes are used: contact mode and tapping mode. In the contact mode, the end of the tip is in mechanical contact with the sample. An electronic feedback control keeps the resulting deflection constant by adjusting the z position of the cantilever. The contact mode has a disadvantage: the tip exerts forces to the sample. Although these forces are only of the order of 1pN - 1 nN, the pressure applied to the sample is huge up to 1000 bar because the contact area is so small. This may lead to structure damages, especially, on soft surfaces.

Another mode used in general is tapping mode. In this mode the cantilever tip is stimulated to vibrations near its resonance frequency (~300 kHz). During approach to the sample surface, the vibration amplitude of the cantilever will decrease because of the interaction force with the surface, which also shifts the resonance frequency. Instead of scanning the sample surface at constant deflection, the surface is scanned at constant reduction of the oscillation amplitude. The tapping mode is less destructive than the contact mode, because the exerted forces are in the low pN range.

2.2 Molecular Electronics

The original ideas from which molecular electronics was developed were the theories of molecular conduction. These theories was proposed in the late 1940s by R. Mulliken and A.Szent-Gyorgi.[50] They proposed the concept of donor-acceptor charge transfer complexes and the possibility that proteins might in fact not be insulators. The investigations of conduction in proteins were carried out by D.D. Eley *et al*.[51] In the famous lecture ‘‘There’s Plenty of Room at the Bottom for Chemists’’, Feynman put forward the idea to build up structures at the molecular level in 1959, which attract the attention to operate single molecules as function elements in information-processing systems.[50]

The biggest contribution which generalize molecular conduction into molecular electronics was done by A. Aviram and Ratner in 1974.[1] They proposed electron donor-acceptor molecule as a molecular diode. Although conducting polymers and preliminary organic electronics were emerging at that time, the papers of Aviram and Ratner generated significant excitement by outlining a model, which indicated that a single molecule could exhibit preferential electronic conduction along its molecular axis.

The subsequent development of self-assembled monolayer (SAM) and scanning probe microscopy (SPM) in the 1980's provided the initial and useful experimental tools for investigating electron transport across molecules junction. Large number of reports of special molecular electronic behavior began to appear in the 1990's, such as negative differential resistance, switches, and memory behavior.

These rapid growths in the field of molecular electronics were motivated, in part, by a multitude of advantages that might be possible when integrating molecular components into microelectronic devices. At first, the numerous degrees of freedom inherent in molecular structure may present new, previously unavailable functions, as far recognition. At second, the promise of lower cost compared to semiconductors is attractive in manufacturing. At third, the much smaller size of molecules may enable heightened capacities, faster performance and provides means to extend Moore's Law beyond the foreseen limits of conventional silicon integrated circuits.

A particularly characterization of the research in molecular electronics is the highly interdisciplinary nature that results from the diverse chemical, physical, and electronic phenomena involved. Every disciplinary have different views and emphasis even to the same issue. For example, in the eyes of a physicist, a molecular junction might be considered a parallel plate capacitor with a special dielectric layer. However, a chemist may focus on the structure of the molecule between two plates. The device may have a variety of I-V characteristics depending on the structure and thickness of molecules. A molecular junction may also be viewed as an organic electronic device in which the critical dimension between the contacts is short enough for electron tunneling to occur, without the thermally activated transport. Alternatively, an electrochemist might look a molecular junction as a very thin electrochemical cell with possibly redox active components or even mobile ions. Contributions from physicists, chemists, materials scientists and engineers, electrical engineers, etc. are all invaluable for the development of molecular electronics.

2.2.1 Approaches for Molecular Electronic Junction

The ability to measure and control electrical current through a molecule junction is a critical issue toward the ultimate goal to building electronic devices using single molecule or molecular monolayer. This ability offers us a unique opportunity to understand charge transport, an important phenomenon that occurs in many chemical and biological processes, and opens a door to chemical and biosensor applications.

Typically, molecular junctions are grouped as two types: ensemble and single molecular. They may be further categorized by the method of fabrication the electrical contact between the electrodes and molecules since the electrodes–molecule bonds have important effects on the electronic properties and stability of the junction. Not only the trapped number of molecules but also the electrodes geometry, electrical field, and interaction between molecules are different in the two types of junctions. Here we focus on the single molecule approach. One kind of the single molecule approach (mechanical controllable break junction, related to my work) will be described in detail in section 2.2.2.

Nanopores and Mercury-Droplet

Compared to the single molecule approach, $\sim 10^3$ to 10^{12} molecules are assembled in parallel between two conducing contacts in the ensemble approach. Commonly four kind of approaches are used: nano-pores, mercury-droplet, cross bar and cross wire. The later two will be described in the next chapter.

A typical nanopores was proposed by Chen et al.[52,53] Combined with optical lithography and reactive ion etching, a single hole with 30nm diameter was made through the silicon membrane. A gold contact of 200 nm thickness was evaporated onto the top side of the membrane, which filled the pore with Au, and works as the top electrode later. The sample was then transferred into a solution to self-assemble the molecules on the top electrode. After evaporating another gold layer at the bottom of the membrane, the metal-molecules-metal junction was fabricated.

With the nanopore approach, one can obtain a defined size of the junction, as well as clean electrodes. While, such method is not usable for bio-molecules since the contact is fabricated by evaporated metal method and the shorts are always exist in the junctions.

In the Mercury-Droplet method, two droplets of mercury are covered with SAMs and brought close each other. When a metal/molecule/metal tunneling junction is formed between two mercury droplets, the current across the molecules layer can be measured. Some group use mercury droplet as a top electrode and use a flat substrate as a bottom electrodes to make a metal/molecules/metal junction. [54] The Mercury-Droplet method can be used to investigate the properties of double molecular layer with a fresh and clean surface. While the active contact area between the molecules and electrode can not be precisely controlled.[55]

Crossbars and Crossed-Wires

In crossed-wire and crossbar methods electrodes are placed on top of each other having a molecular layer in between. Within this 'ensemble' molecule' technique, the electronic response represents that of $10^3 \sim 10^{12}$ molecules in parallel. [56-58]

Kushmerick et al proposed a kind of crossed-wire tunnel junction, where a molecular monolayer was sandwiched between two macroscopic gold wires.[59] The wires are mounted in a test stage so that they are crossed and the wire spacing is controlled by the Lorentz force: a DC current is conducted in one wire and deflects it toward the second wire in a magnetic field, see figure 2.7.

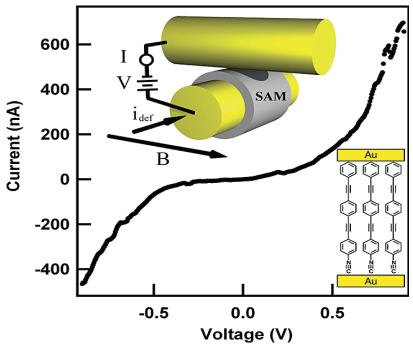

Figure 2.7: *I–V* characteristics of the cross wires junction [59]

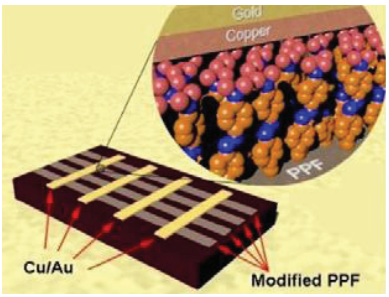

Figure 2.8: Cross-bar junction made by evaporating a metal layer onto a molecular layer covalently bonded to a carbon substrate. [60]

A crossbar is a set of wires with microscopic or macroscopic dimension crossing each other with a functional layer in the cross-points. The concept of crossbar fulfills the major requirement of future nano-scale devices: the dimension of wires can be scaled down to molecular dimensions; It can be switched a current on and off to address a single cross-point. Cross bar with N wires on each electrodes layer can address 2^N cross-point. Combined with external systems it can be used to perform memory, logic functions and even information processing. The simple physical structure makes the fabrication feasible and potentially widely applying. The disadvantage of cross bar and cross wire is the unconfirmed contact since the electrode corrugation is larger than the molecules size.

Scanning Probe Techniques

The single-molecule approach was firstly enabled by the development of scanning probe microscopy in 1980's. This kind of techniques made it possible to image individual molecules on surface, or rather the electronic structure of the molecules. To date, STM and conductive AFM have revealed many interesting phenomena, which is important for the development of molecular electronics. For examples, reversible redox switching,[38] an electromechanical molecular amplifier, [61]the negative differential resistance-like effect, [62] molecular switching, [63]and the study of field effects on electron transport in molecules [64] had been reported by the scanning probe techniques.

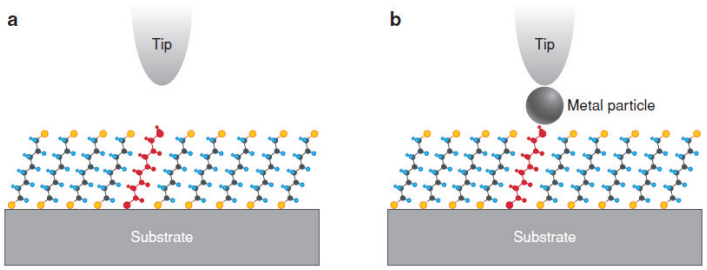

Figure 2.9: (*a*) STM study of electron transport through a target molecule inserted into an ordered array of reference molecules. (*b*) STM measurement a molecule with one end attached to a substrate and the other end bound to a metal nanoparticle.[2]

In the STM or AFM method, a metal/molecues/metal junction is formed between the substrate and the tips when the tips contact with the molecules which bond to the substrate. The advantage of the SPM method is that the surface imaging can be obtained, hence the arrangement of molecules as well as the structure of molecules can be revealed. The main obstacle is that: a molecule adsorbs onto a substrate to form a well-defined molecule-substrate contact, but the tip-molecule contact is often less well defined, which prevents one from investigating the absolute properties of the molecule. Many ideas had been put forward. One way to reduce this problem is to embed a molecule of interest into the matrix of another kind of molecules, often less conducting molecule (figure 2.9 *a*).[2] Another approach is to attach one end of a molecule onto a substrate and the other end to an Au nanoparticle covalently (figure 2.9 *b*).[2]

2.2.2 Mechanical Controllable Break Junction

One of the challenges in the bioelectronics is to fabricate electrodes separated with a gap which can fit a sample molecule precisely and measure the properties of various type of molecules. This difficulty may be overcome by bringing two electrodes mechanically together or separating them apart. The idea of mechanically controllable break junction (MCBJ) was invented by J. Moreland and J. W. Ekin in 1985 and further developed by C. Muller in 1988-1992. .[65]

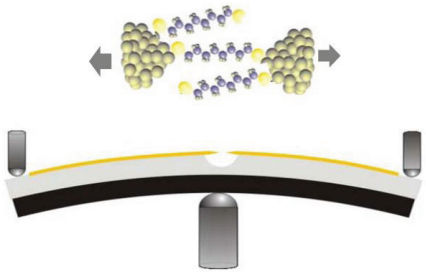

Figure 2.10: Schematics of a mechanically controllable break junction. The movement of push rod will result in the break of metal-molecule-metal junction.

The principle of this method is presented in figure. 2.10. A small piece of a metallic wire is fixed at two points on a flexible substrate, which can be called bending beam also. The cross section of the wire is reduced between two fixed points by making a notch near the middle of the wire. The bending substrate is fixed at both ends by counter supports. A vertical movement of the push rod, which can be precisely positioned with a piezo actuator or stepping motor, will exert a force to the bending beam. As the beam is bent, the sample wire starts to elongate between the two fixed points, which results in the reduction of the cross section at the notch, and finally the wire completely raptures.

After break the wire, two clean facing nano-electrodes were generated. The distance between the electrodes for both the opened and the closed directions was controlled by bending or relaxing the substrate, respectively. After integrating the molecules into the gap, they may bridge the two electrodes and the electronic properties of the molecules can be determined.

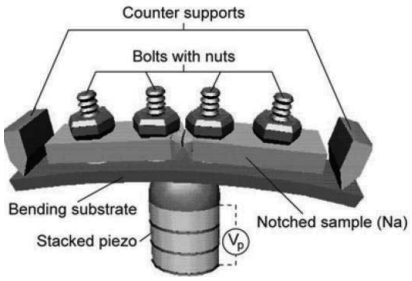

Figure 2.11: The set up of a mechanically controllable break junction[66]

The advantage of MCBJ was that: firstly, the MCBJ set up can be easily integrate into other system, for instance, high vacuum system and Raman spectrometer. Secondly, the probability of contamination is reduced because a fresh break cross section of the gold bridge is created and used in the MCBJ experiment. Thirdly, combined with the lithography technique, the electrode can be scaled down to molecule dimensions, which make single molecule measurements possible.

However, the biggest advantage of the break junction technique is the high mechanical stability of the system. The electrodes are rigidly fixed to the substrate at a short separation (about 0.5 mm by traditional fabrication, and ~ 1μm by lithography fabrication), so the length of the free standing parts is much shorter than in a typical STM setup. This is why the junction is insensitive to mechanical vibrations. On the other hand, due to the mechanical configuration of the bending beam, the vertical motion of the push rod (Δz) causes only a highly reduced horizontal displacement (Δx) of the electrodes ($\Delta z / \Delta x > 100$). This means that any bad effect from the push rod (for instance vibration, thermal expansion or voltage instability on the Piezo element) has been strongly reduced on the junction. Moreover, using a piezoelectric transducer (PZT) or other mechanical actuation mechanisms, one can control the gap with sub-angstrom precision, which is impossible for other devices.

Beside the important advantages of the MCBJ technique, the main disadvantage are the uncontrollable details of the breaking process, for instance, the exact shape of the electrodes is always unknown as well as the detail atom configuration of the electrodes. MCBJ cannot scaled like a crossbar to address a specially cross-section, which limits the potential application in the

information processing. However, as a fundamental research technique, MCBJ show unique advantage, especially in the single molecule measurement.

Followed the development of lithography techniques, some new generation of MCBJ appeared. For example, a micro-fabrication of a mechanically controllable break junction based on silicon was demonstrated by Reed et. al.[67]. The attenuation factor ($\Delta x/\Delta z$) can reach 10^{-5} in this new kind of MCBJ set up. Now, mechanically controllable break junction had been widely used for the molecular electronics.

For the micro-fabricated mechanically controllable break junction, a nano-wire is commonly defined by lithography, see figure 2.12. Typical nano-wires exhibit big aspect ratios (length/width ratio) of 100 or more. As such they are often referred to as one-dimensional materials. Nano-wires have many interesting properties that are not observed in bulk or 3-D materials. This is because electrons in nano-wires are quantum confined laterally and thus occupy energy levels that are different from the traditional continuum of energy levels or bands found in bulk materials. Dependent on the material, nano-wire shows discrete values of the electrical conductance. Such discrete values arise from a quantum mechanical restraint on the number of electrons that can travel through the wire at the nanometer scale. These discrete values are often referred to as the quantum of conductance and are integer values of G_0 , $G_0 = 2e^2 / h \approx 77\mu S$.

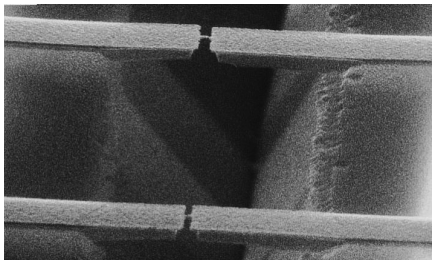

Figure 2.12: Mechanically controllable break junction based on silicon substrate. Each device shows two cantilevers which are covered and bridged by the gold wire.[67]

2.2.3 Electron Transport in Molecular Junction

Electron Tunneling Through a Barrier

Tunneling is a quantum mechanical effect. A tunneling current occurs when electrons move through a barrier that they classically shouldn't be able to move though. In classical terms, as long as partical energy is smaller than barrier energy no transmission is possible. However, in the quantum mechanical world, electrons have wavelike properties which make the electron tunneling through the barrier.

One example is the electron tunneling through a rectangular barrier. The energy of the electron is: $E = \frac{1}{2}mv^2$, and the distribution of barrier is:

$$V(x) = \begin{cases} \Phi_0, a_1 < x < a_2 \\ o, \quad else \end{cases} \qquad (2.2)$$

Here, Φ_0 is the value of energy barrier. If we use (unknown) mathematical function $\varphi(x,t)$ to describe the quantum state of the system, development of the quantum state can be described by the time-independent Schrödinger equation:

$$H \cdot \varphi = E \cdot \varphi \qquad (2.3)$$

E : total energy of the system. H : Hamilton operator

$$H(x) = -\frac{\hbar^2}{2m}\frac{\partial^2}{\partial x^2} + V(x) \qquad (2.4)$$

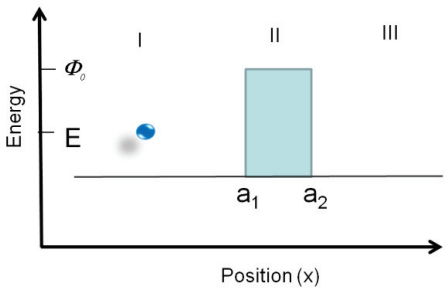

Figure 2.13: The barrier distribution in one dimensional picture

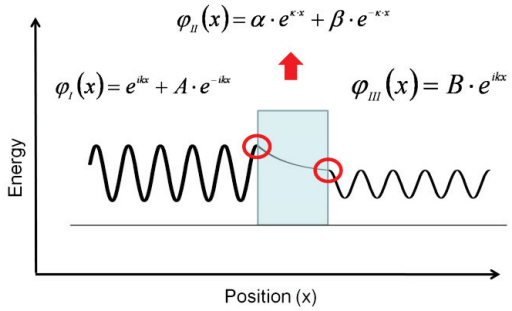

Figure 2.14: Electron tunneling through a rectangular barrier

Put equation (2.2) and (2.3) into 2.4, one can obtain the solution: in the barrier regime,

$$\varphi_{II}(x) = C \cdot e^{\kappa \cdot x} + D \cdot e^{-\kappa \cdot x}, \quad \kappa = \frac{\sqrt{2m\Phi_0 - E}}{\hbar} \tag{2.5}$$

Out side the barrier regime,

$$\varphi_{I}(x) = e^{ikx} + A \cdot e^{-ikx}, \quad \varphi_{III}(x) = B \cdot e^{ikx}, \tag{2.6}$$

Here,

$$k = \frac{\sqrt{2mE}}{\hbar}, \quad B = \frac{1}{1 + \frac{k^2 + \kappa^2}{4k^2\kappa^2}\sinh(\kappa L)} \tag{2.7}$$

L is the barrier width, and $T = |B^2|$ was defined as transmission probability.

Electron Tunneling Through a Metal/Molecule/Metal Junction

Going to metal/molecule/metal junctions the classical barrier has to be replaced by molecular orbital of the molecule. An approximation is, that the barrier height becomes $\phi_B = (E_{LUMO} - E_F)$ or $\phi_B = (E_F - E_{HOMO})$ for tunneling through the LUMO or HOME. Holmlin *et al* modified the Simmons model, which is original used to describe electron transport behavior in one-dimensional rectangular barrier and take use of it to describe the behavior of electron tunneling through molecular junction. The modified Simmons model expresses the tunneling current density through a barrier in the regime $V < \phi_B / e$ as

$$J = \frac{e}{4\pi^2 \hbar d^2}\left\{(\phi_B - \frac{eV}{2}) * \exp\left[-\frac{2(2m)^{\frac{1}{2}}}{\hbar}\alpha(\phi_B - \frac{eV}{2})^{\frac{1}{2}} d\right] - (\phi_B + \frac{eV}{2}) * \exp\left[-\frac{-2(2m)^{\frac{1}{2}}}{\hbar}\alpha(\phi_B + \frac{eV}{2})^{\frac{1}{2}} d\right]\right\}, \tag{2.7}$$

where ϕ_B is the barrier height, which can be approximated by the energy offset between the Fermi level of the nanoelectrode and the nearest molecular orbital, m is the electron mass, d the barrier width, and V is the applied bias. For molecular systems, the Simmons model has been modified with a parameter α. α is a adjustable parameter that is introduced to provide either a way of applying the rectangular barrier tunneling to a nonrectangular barrier tunneling , or an adjustment to account for the effective electron mass (m^*) in a rectangular barrier, or both.[68] α = 1 corresponds to the case for a rectangular barrier and bare electron mass. By fitting individual *I (V)* data using equation 2.7, ϕ_B and α values can be obtained.

But please note some assumptions underlying this model are the following: (i) the barrier height of this junction is constant over the entire tunneling distance, and the barrier is rectangular; (ii) the dielectric constant of the medium make the barrier is uniform and does not affect the shape of the barrier; (iii) the electron transport is independent of temperature; and (iv) the image potential effect to the height and width of the barrier was not taken into account. Equation can be approximated in two limits: low bias and high bias compared to ϕ_B. In case of low bias range, the current density is given by

$$J \approx (\frac{(2m\phi_B)^{1/2} e^2 \alpha}{\hbar^2 d})\ V \exp\left[\frac{2(2m)^{\frac{1}{2}}}{\hbar}\alpha(\phi_B)^{\frac{1}{2}} d\right]. \tag{2.8}$$

The decay constant is given as

$$\beta_0 = \frac{2(2m)^{\frac{1}{2}}}{\hbar}\alpha(\phi_B)^{\frac{1}{2}} \quad . \tag{2.9}$$

In case of high bias, the first term of equation (2.7) is dominant and the current density is given by

$$J \approx \frac{e}{4\pi^2 \hbar d^2}\left\{(\phi_B - \frac{eV}{2}) * \exp\left[-\frac{2(2m)^{\frac{1}{2}}}{\hbar}\alpha(\phi_B - \frac{eV}{2})^{\frac{1}{2}} d\right]\right\} \tag{2.10}$$

The decay constant is

$$\beta_V = -\frac{2(2m)^{\frac{1}{2}}}{\hbar}\alpha(\phi_B - \frac{eV}{2})^{\frac{1}{2}} \tag{2.11}$$

At high bias regime (attention $V < \phi_B / e$ should be satisfied) the decay constant decreases as bias increases, which results from barrier bowering effect due to the applied bias.

The Simmons equation assumes a trapezoidal barrier when the applied bias is smaller than the barrier height. In the zero-bias limit the barrier is rectangular and the Simmons equation reduces to $I \propto \exp(-2d\sqrt{2m\phi}/\hbar)$. As an opposite limit one can consider the case of when the applied bias exceeds the barrier height. For this assumption, the electron transport mechanism will change from direct tunneling to field emission and the Simmons equation transforms to $\ln(I/V^2) \propto -\frac{4d\sqrt{2m\phi^3}}{3\hbar q}(\frac{1}{V})$. In the field emission (Fowler-Nordheim tunneling) regime, $\ln(I/V^2)$ depends linearly on $1/V$ for a fixed d.[69]

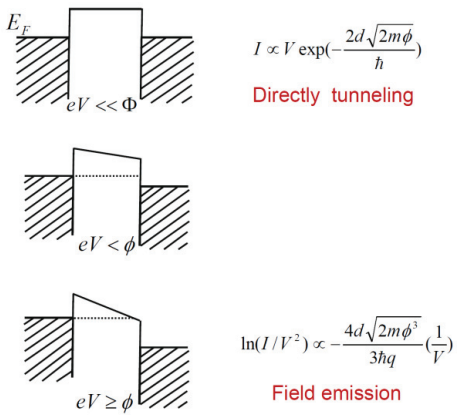

Figure 2.15: Simmons model. A molecule is depicted as a tunnel barrier of height ϕ and length d. when a bias is applied the barrier is tilted. The corresponding I-V characteristic behavior was shown by formula on the right side.

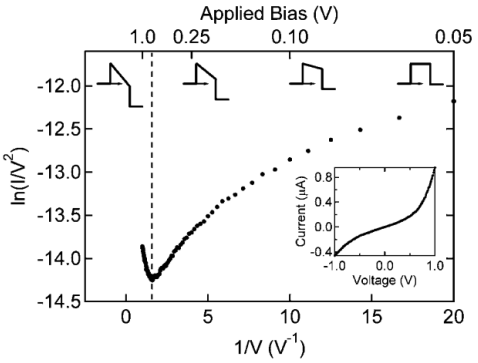

Figure 2.16: Solid circles represent the average of 100 *I-V* curves for a Au-anthracenethiol-Au junction measured by CP-AFM. The dashed line corresponds to the voltage at which the tunneling barrier transitions from trapezoidal to triangular (*V*trans). Also shown are representations of the barrier shape at various values of applied bias. The inset shows current-voltage data on standard axes.[69]

Beebe take a original approach to plot I-V data in the form $\ln(I/V^2)$ *vs* $1/V$.[69] Interesting such FN-plot yield a well-defined minimum at a voltage V_m, see figure 2.4. Referring to the Simmons model, Beebe et al. suggest that: (i) V_m scales linearly with $\phi = E_F - E_{HOMO}$ (or $E_{LUMO} - E_F$); (ii) V_m is independent of molecular length d for constant ϕ; (iii) V_m equals the voltage at which there is a transition to the field emission regime (hence "transition voltage"). The so called transition voltage spectroscopy(TVS) remarkably advanced the measurement of the relative barrier height in molecular junctions.[34,69-73]

However, the Simmons model is just a simple model to describe the $I(V)$ characteristic. For instance, such model do not take the coupling between the molecule and electrode into account, which is always different at both end of the molecules, hence always present a symmetric $I(V)$ characteristic.

An important consideration when working with single molecules is the strength of the coupling between the electrons in the electrodes and those in the molecule. If the coupling between the molecules and the electrodes is strong rather than weak, the energy levels in the molecule - which are relatively narrow in the weak coupling case or in isolated molecules in the gas phase -

become significantly broader. The coupling between electrode and molecules strong affect the electron transport through the junction.

The effect of coupling is taken into account in the single-level model. Within this model the current through molecular junction is given by the Landauer formular:

$$I(V) = \frac{2e}{h}\int_{-\infty}^{\infty} T(E,V)\left[f(E-e/2) - f(E+e/2)\right] dE \tag{2.12}$$

$T(E,V)$ is the transmission function that depends both on the energy E and voltage V. $f(E) = 1/\left[1+\exp(E-\mu)/K_B T\right]$ is the Fermi function with μ as the lead chemical potential and $k_B T$ being the thermal energy. In this model, the transmission is given by the Breit–Wigner formula:

$$T(E,V) = \frac{4\Gamma_L \Gamma_R}{\left[E - E_0(V)\right]^2 + \left[\Gamma_L + \Gamma_R\right]^2} \tag{2.13}$$

Here, E_0 is the energy of the molecular level, which can depend on the bias voltage, Γ_L and Γ_R are the scattering rates related to the probability of injecting an electron into the molecule from the left (L) and right (R) electrodes. A asymmetric I (V) response can be described successfully by the single-level model assuming unequal coupling parameters $\Gamma_L \neq \Gamma_R$.

Actually, many parameters effect the electron transport behavior. A detail transport model which take the electrode, molecule structure and the coupling between metal and molecules into consideration was proposed by Kiguchi *et al*[74]. In his model the conductance of a single molecular junction determined by not only the molecule-metal bond strength and the local density states of the electrodes but also depend on the degree of π-conjugation, and can be presented as

$$G = A(t^2 \rho / \Delta E)^2 P \ , \tag{2.14}$$

where G is the conductance of the molecular junction. A and t, are constant, hopping integral between the metal and molecular orbital (MO) which mainly dependent on the bond strength. ΔE is the energy difference between the Fermi level of the electrode (E_F) and conduction orbital of molecule(MO), please see Figure 2.17. The conduction MO can be the highest occupied molecular orbital (HOMO) or the lowest unoccupied molecular orbital (LUMO).

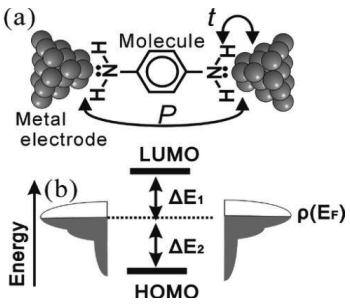

Figure 2.17: Schematic view and energy diagram of the single molecular junction and the important parameter which determine the conductance o f the single molecular junction.[74]

Because the conduction MO is not always delocalized over the whole molecule in the real molecular junctions of π-conjugated molecules, an additional parameter (*P*) is added to represent the degree of π-conjugation. From the formula 2.14, large ρ, *t*, and *P* values and a small ΔE value lead to large conductivity.

Compared with different electron transport model, Huisman *et al* give a full interpretation of transition voltage. In his papers three different electron transport models were taken into account and compared each other: Simmons model, Simmons model including image potential, Stratton model, and Landauer approach model.

After theory calculation with Simmons model and Stratton model, Huisman *et al* found that V_m is scales linearly with $\phi^{1/2}$ in stead of ϕ. More important, all the three model show that the V_m is strongly dependent on molecular length *d,* see Figure 2.18.

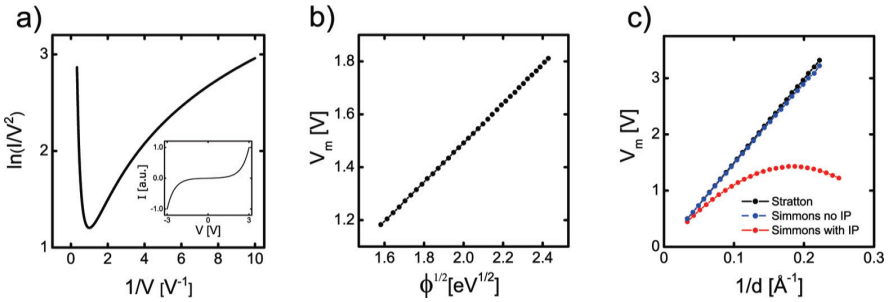

Figure 2.18 (a) Fowler-Nordheim plot for a barrier with ϕ = 4 eV and d =10 Å, as predicted by the Simmons model. Inset: corresponding $I(V)$ curve on a linear scale. (b) V_{m} versus $\phi^{1/2}$ for the Simmons model. (d =10 Å). (c) V_{m} versus $1/d$ for ϕ=4 eV, using various tunnel models: black, Stratton model ; blue, full Simmons model without image potential; red, full Simmons model including image potential . Clearly, V_{m} depends strongly on d in all cases.

In order to explain the experimental data obtained by Beebe, one also take molecular transport model (Landauer approach) into account. For the molecular transport model, Huisman *et al* demonstrate $V_m \propto \phi$ for a range of realistic values of ϕ, and V_m is independent of molecular length for large distance.

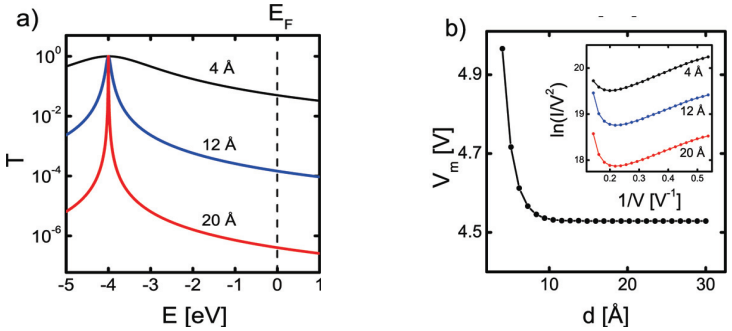

Figure 2.19 Molecular transport model applied to alkane junctions . (a) Transmission function for three different lengths . (b) V_{m} versus molecular length d. V_{m} becomes length independent for d > 8 Å, consistent with the experiments by Beebe et al. Inset: FN plots for the junctions in (a).[71]

Molecular model is radically different from those obtained for various Simmons models. The voltage profile is radically different. In the Simmons model, the potential decreases linearly with distance, whereas in the "molecular" model, the voltage drops at the contacts only. It is easily visualized that the latter will result in V_m being independent on *d*.

As shown in table 1, transport mechanisms are grouped into four groups according to the characteristic of current-voltage dependences, and the conduction-temperature dependence [53]. Based on whether thermal activation is involved, the transport mechanisms fall into two distinct groups: (i) thermionic or hopping conduction which has temperature- positive dependent *I (V)* behavior. (ii) Direct tunneling or Fowler–Nordheim tunneling (field emission), which does not have temperature-dependent *I (V)* behavior.

All of the four kind of transport mechanisms had been experimental demonstrated, for example, thermionic and hopping conductions have been observed for 4-thioacetylbiphenyl SAMs [75,76]. But for those molecules with the large HOMO–LUMO gap and short length, such as alkanethiol molecular system, directly tunneling and field emission have been revealed.[77] Transport mechanism is depend on the molecule length. Frisbie et al reported that they observed the theoretically predicted change from tunneling to hopping as a function of systematically controlled molecular wire length.[78]

Table 1: Possible conduction mechanisms [53]

Conduction mechanism	Characteristic behaviour	Temperature dependence	Voltage dependence
Direct tunnelling[a]	$J \sim V \exp\left(-\frac{2d}{\hbar}\sqrt{2m\Phi}\right)$	None	$J \sim V$
Fowler–Nordheim tunnelling	$J \sim V^2 \exp\left(-\frac{4d\sqrt{2m}\Phi^{3/2}}{3q\hbar V}\right)$	None	$\ln\left(\frac{J}{V^2}\right) \sim \frac{1}{V}$
Thermionic emission	$J \sim T^2 \exp\left(-\frac{\Phi - q\sqrt{qV/4\pi\varepsilon d}}{k_B T}\right)$	$\ln\left(\frac{J}{T^2}\right) \sim \frac{1}{T}$	$\ln(J) \sim V^{1/2}$
Hopping conduction	$J \sim V \exp\left(-\frac{\Phi}{k_B T}\right)$	$\ln\left(\frac{J}{V}\right) \sim \frac{1}{T}$	$J \sim V$

2.2.4 Ligand Field Theory

In chemistry, a coordination complex or metal complex, is a structure consisting of a central atom or ion (usually metallic), bonded to a surrounding array of molecules or anions. The ions or molecules surrounding the central atom are called ligands. Ligands are generally bound to the central atom by a coordinate covalent bond. In coordination chemistry, a structure is first described by its coordination number, the number of ligands attached to the metal (more specifically, the number of σ-type bonds between ligand(s) and the central atom).[79,80] For instance, linear structure for two-ligands and octahedral structure for six-ligands.

Ligand field theory (LFT) describes the bonding, orbital arrangement, and occupation of coordination complexes.[81] It represents an application of molecular orbital theory to metal complexes. A transition metal ion has nine valence atomic orbitals, one (n+1)s, five nd , and three (n+1)p orbitals. These orbitals are of appropriate energy to form bonding interaction with ligands. The LFT analysis is highly dependent on the geometry of the complex, and most explanations begin by describing octahedral complexes, where six ligands can coordinate to the metal ion.

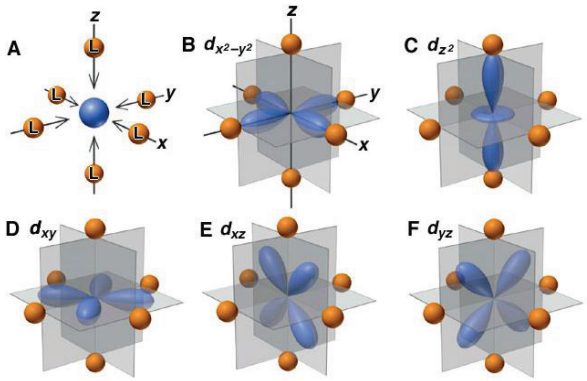

Figure 2.20: Orbitals in an octahedral field of ligands.[a]

[a] Martin Silberberg. Chemistry: The Molecular Nature of Matter and Change. 2nd edition. 2008.

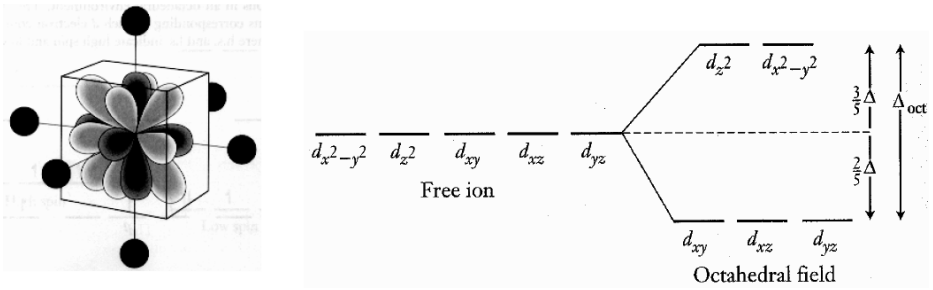

Figure 2.21: Crystal Field Splitting.[a].

To derive a quantilive picture the simplified crystal field can be used. According to crystal field theory, metal ion and its ligands exhibit electrostatic attractions along X,Y,Z axes. However, electrons in d-orbitals of metal ion are repelled by negative charges of the ligands and therefore experience increase in potential energy. The degree of repulsion between ligands and d-orbital electrons depend on the orientation of the d-orbitals. d-Orbitals with lobes directed between ligands suspend weaker repulsion while d-orbitals with lobes towards ligands feel stronger repulsion. For octahedral arrangement, two of the d-orbitals point towards the ligands. Repulsion between the ligand electrons and electrons in these two d-orbitals destabilizes them. The 6 ligands split d-orbitals into 3 lower energy levels (d_{xy},d_{yz},d_{xz}) and 2 higher energy levels ($d_{x^2-y^2}$,d_{z^2}), as shown in the Figure 2.21. Δ_{oct} is referred to as the ligand field splitting for the octahedral complex.

An important parameter which describes the metal complex properties was the stability constant. The stability constant is an equilibrium constant for the formation of a complex in solution. It is a measure of the strength of the interaction between the reagents that come together to form the complex. The formation of a complex between a metal ion, M, and a ligand, L, is in fact usually a substitution reaction. The stability constant is usually give by

$$K_1 = \frac{[ML]}{[M][L]} \qquad (2.15)$$

[a] Martin Silberberg. Chemistry: The Molecular Nature of Matter and Change. 2nd edition. 2008.

Usually the stability constant depend on ionic strength, temperature and ionic radius. The theoretical studies on a series of isoelectronic complexes which are carried out with DFT method shown that with increase of the atomic number of the center atom M, the energy interval between HOMO and LUMO increases, and the chemical stability of the complex increases.[82]

2.3.5 Density Functional Theory

Density functional theory (DFT) is widely quantum mechanical modeling method used in physics and chemistry in the past 30 years to compute the electronic structure of matter.[83] Its applicability ranges from atoms, molecules and solids to nuclei and quantum and classical fluids. In chemistry: DFT predicts a great variety of molecular properties: molecular structures, vibrational frequencies, atomization energies, ionization energies, electric and magnetic properties, reaction paths, etc.

With this theory, the properties of a many-electron system can be determined by using functionals, i.e. functions of another function, which in this case is the spatially dependent electron density. Hence the name density functional theory comes from the use of functionals of the electron density. In this part we introduce the basic concepts underlying density functional theory.

The Solution of the Schrödinger Equation

At first, the calculation of the ground state energy of a collection of atoms will be primarily concerned. The energy may be computed by solution of the Schrödinger equation – Born-Oppenheimer approximation is, [a]

$$\hat{H}\psi(r_1, r_2, ..., r_N) = E\psi(r_1, r_2, ..., r_N) \tag{2.16}$$

Here $\psi(r_1, r_2, ..., r_N)$ is the wavefunction which described the stationary electronic state. The Hamiltonian operator, $\hat{H}$, consists of a sum of three terms; the kinetic energy, the interaction of

[a] 4 R. G. Parr, and W. Yang, Density-Functional Theory of Atoms and Molecules, OUP, Oxford, (1989)

electrons with the atomic nuclei(V_{ext}) and the electron-electron interaction of the N-electron system ;

$$\hat{H} = -\frac{1}{2}\sum_{i}^{N}\nabla_i^2 + \hat{v}_{ext} + \sum_{i<j}^{N}\frac{1}{|\vec{r}_i - \vec{r}_j|} \tag{2.17}$$

$$\hat{v}_{ext} = \sum_{\alpha}^{N_{at}}\frac{Z_\alpha}{|\vec{r}_i - \vec{R}_\alpha|} \tag{2.18}$$

Here, r_i is the coordinate of electron *i* and the nucleus charge at R_α is Z_α. The lowest energy eigenvalue, E_0, is the ground state energy and the probability density of finding an electron with any particular set of coordinates $\{r_i\}$ is $|\Psi_0|^2$. The average total energy for a state specified by a particular Ψ, and is the expectation value of $\hat{H}$, that is;

$$E[\psi] = \int \psi^* \hat{H} \psi dr \equiv \left\langle \psi \middle| \hat{H} \middle| \psi \right\rangle \tag{2.19}$$

The notation [Ψ] emphasizes the fact that the energy is a functional of the wave function. The ground state wavefunction and energy may be found by searching all possible wavefunctions for the one that minimizes the total energy. Assume there are N electronics in the system, Hartree-Fock put forward an ansatz for the structure of Ψ - it is assumed to be an antisymmetric product of functions (ϕ_i) each of which depends in the coordinates of a single electron, that is: [a]

$$\psi_{HF} = \frac{1}{\sqrt{N!}}\begin{vmatrix} \phi_1(r_1) & \phi_1(r_2) & \dots & \phi_1(r_N) \\ \phi_2(r_1) & \phi_2(r_2) & \dots & \phi_2(r_N) \\ \vdots & \vdots & & \vdots \\ \phi_3(r_1) & \phi_3(r_2) & \dots & \phi_3(r_N) \end{vmatrix} \tag{2.20}$$

Substitution equation 2.20 into the Schrödinger equation results in an expression for the Hartree Fock energy;

[a] 5 A. Szabo and N. S. Ostlund, Modern Quantum Chemistry, Macmillan, New York, (1982)

$$E_{HF} = \int \phi_i^*(\vec{\mathrm{r}}) \left(-\frac{1}{2} \sum_{\mathrm{i}}^{\mathrm{N}} \nabla_{\mathrm{i}}^2 + \mathrm{V}_{\mathrm{ext}} \right) \phi_{\mathrm{i}}(\vec{\mathrm{r}}) \mathrm{d}\vec{\mathrm{r}}$$
$$+ \frac{1}{2} \sum_{\mathrm{i,j}}^{\mathrm{N}} \int \frac{\phi_{\mathrm{i}}^*(\vec{\mathrm{r}}_1) \phi_{\mathrm{i}}(\vec{\mathrm{r}}_1) \phi_{\mathrm{j}}^*(\vec{\mathrm{r}}_2) \phi_{\mathrm{j}}(\vec{\mathrm{r}}_2)}{\left| \mathrm{r}_{\mathrm{i}} - \mathrm{r}_{\mathrm{j}} \right|} \mathrm{d}\vec{\mathrm{r}}_1 \mathrm{d}\vec{\mathrm{r}}_2 \qquad (2.21)$$
$$- \frac{1}{2} \sum_{\mathrm{i,j}}^{\mathrm{N}} \int \frac{\phi_{\mathrm{i}}^*(\vec{\mathrm{r}}_1) \phi_{\mathrm{j}}(\vec{\mathrm{r}}_1) \phi_{\mathrm{i}}^*(\vec{\mathrm{r}}_2) \phi_{\mathrm{j}}(\vec{\mathrm{r}}_2)}{\left| \vec{r}_{\mathrm{i}} - \vec{\mathrm{r}}_{\mathrm{j}} \right|} \mathrm{d}\vec{\mathrm{r}}_1 \mathrm{d}\vec{\mathrm{r}}_2$$

Here, V_{ext} is simply the interaction of the electrons with the atomic nuclei as shown in equation (2.17). In equation (2.21), the right second term is simply the classical Coulomb energy written in terms of the orbital and the third term is the exchange energy. The ground state orbital are determined by applying the variation theorem (the energy is higher than that of the ground state unless ψ corresponding to ψ_0) to this energy expression under the constraint that the orbitals are orthonormal. This leads to the Hartree-Fock (or SCF) equations;

$$\left[-\frac{1}{2} \nabla^2 + v_{ext}(\vec{r}) + \int \frac{\rho(\vec{r}')}{\left| \vec{r} - \vec{r}' \right|} d\vec{r}' \right] \phi_i(r) + \int v_x(\vec{r}, \vec{r}') \phi_i(\vec{r}') d\vec{r}' = \varepsilon_i \phi_i(\vec{r}) \qquad (2.22)$$

Here, $\rho(\vec{r})$ was determined by $\rho(\vec{r}) = \sum_i^{occ} \left| \phi_i(\vec{r}) \right|^2$, so called electron density. For non-local exchange potential v_{ext} was determined by such equation,

$$\int v_{ext}(\vec{r}, \vec{r}') \phi_i(\vec{r}') d\vec{r}' = -\sum_j^N \int \frac{\phi_j(\vec{r}) \phi_j^*(\vec{r}')}{\left| \vec{r} - \vec{r}' \right|} \phi_i(\vec{r}') d\vec{r}' \qquad (2.23)$$

Therefore, the Hartree-Fock equations describe non-interacting electrons under the influence of a mean field potential consisting of the classical Coulomb potential and a non-local exchange potential. A better approximations (correlated methods) for ψ and E_0 are readily obtained. However, the computational cost of such improvements is very high and scales prohibitively quickly with the number of electrons treated. In addition, accurate solutions require a very flexible description of the wavefunction's spatial variation, i.e. a large and basis set is required which also adds to the expense for practical calculations. This is a major motivation for the development and use of density functional theory.

The Hohenburg-Kohn Theorems

In 1964 Hohenburg and Kohn published a very important paper and proved the two theorems in this paper [a]. The first theorem may be stated as follows; The electron density determines the external potential. If this statement is true then it immediately follows that the electron density determines the Hamiltonian operator (please see equation 2.17). This follows as the Hamiltonian is specified by the external potential and the total number of electrons, N, which can be computed from the density simply by integration over all space. Thus, in principle, given the charge density, the Hamiltonian operator could be uniquely determined and all material properties can be computed.

To the second theorem, a variation principle was established: the density that minimises the total energy is the exact groundstate density.

$$\int \rho_t(\vec{r})d\vec{r} = N \text{ then } E[\rho_t] \geq E_0 \tag{2.24}$$

This theorem restricts density functional theory to studies of the ground state. An extension allows variation to excited states that can be guaranteed orthogonal to the ground state but in order to achieve this knowledge of the exact ground state wave function is required. This two theorems lead to the fundamental statement of density functional theory,

$$\delta\left[E[\rho] - \mu\left(\int \rho(\vec{r})d\vec{r} - N\right)\right] = 0 \tag{2.25}$$

Here, μ is the electronic chemical potential. The above discussion establishes the fact that there is a universal functional $E[\rho]$, which if we know its form, could be inserted into the above equation and minimized to obtain the exact ground state density and energy.

[a] P. Hohenburg and W. Kohn, *Phys. Rev.* **136** B864 (1964)

The Energy Functional

From equation (2.16) and (2.17), it can be see that the energy functional contains three terms, which are the kinetic energy, the interaction with the external potential and the electron-electron interaction. Therefore the functional can be write as,

$$E[\rho] = T[\rho] + \mathrm{v}_{ext}[\rho] + \mathrm{v}_{ee}[\rho] \tag{2.26}$$

The interaction with the external potential is trivial. Here, we focuses on other two terms. Kohn and Sham proposed the following approach to approximating the kinetic and electron-electron functionals[a]. They introduced a fictitious system of N noninteracting electrons to be described by a single determinant wavefunction in N "orbitals" ϕ_i. In this system the kinetic energy and electron density are known exactly from the orbitals,

$$T_S[\rho] = -\frac{1}{2}\sum_{i}^{N}\left\langle \phi_i \middle| \nabla^2 \middle| \phi_i \right\rangle \tag{2.27}$$

Here, the T_s emphasizes that this is not the true kinetic energy but is that of a system of non-interacting electrons. The true ground state density can be written as:

$$\rho(\vec{r}) = \sum_{i}^{N} \left|\phi_i\right|^2 \tag{2.28}$$

Please note that a significant component of the electron-electron interaction will be the classical Coulomb interaction as shown in equation (2.21);

$$V_H[\rho] = \frac{1}{2}\int \frac{\rho(\vec{r}_1)\rho(\vec{r}_2)}{\left|\vec{r}_1 - \vec{r}_2\right|} d\vec{r}_1 d\vec{r}_2 \tag{2.29}$$

Now, the energy functional can be write as;

$$E[\rho] = T_S[\rho] + V_{ext}[\rho] + V_H[\rho] + E_{xc}[\rho] \tag{2.30}$$

[a] W. Kohn and L. J. Sham, *Phys. Rev.* **140** A1133 (1956)

where the exchange-correlation functional $E_{xc}[\rho]$ is introduced ;

$$E_{xc}[\rho] = (T[\rho] + T_S[\rho]) + (V_{ee}[\rho] - E_H[\rho]) \tag{2.31}$$

E_{xc} is simply the sum of the error made in using a non-interacting kinetic energy and the error made in treating the electron-electron interaction classically. Combined equation (2.30) and (2.24), we can get so called Kohn-Sham equations,

$$\left[-\frac{1}{2}\nabla^2 + v_{ext}(\vec{r}) + \int \frac{\rho(\vec{r}')}{|\vec{r} - \vec{r}'|} d\vec{r}' + v_{xc}(\vec{r}) \right] \phi_i(\vec{r}) = \varepsilon_i \phi_i(\vec{r}) \tag{2.32}$$

$v_{xc}(\vec{r})$ is the functional derivative of the exchange correlation energy with respect to the density,

$$v_{xc}(\vec{r}) = \frac{\delta E_{xc}[\rho]}{\delta \rho} \tag{2.33}$$

The Kohn-Sham equations describe the behavior of non-interacting "electrons" in an effective local potential. For the exact functional and thus exact local potential, the "orbitals" yield the exact ground state density by equation (2.28), and exact ground state energy via Equation (2.30). The charge density and energy of the many-body and the non-interacting system is only exact if the exact functional is known. In this sense Kohn-Sham density functional theory is an empirical method-we do not know the exact functional. But, the functional is universal since it does not depend on the materials being investigated. In principle, for any particular system we could solve the Schrödinger equation exactly determining the energy functional and associated potential. The ability to determine exact properties of the universal functional in a number of systems allows excellent approximations to the functional to be developed.

The Local Density Approximation (LDA) for $E_{xc}[\rho]$

The development of approximations for E_{xc} has lead to a large and still rapidly expanding field of research. There are now many different flavors of functional available, such as LDA, generalized gradient approximation (GGA) and Meta-GGA. Each of them is more or less appropriate for any particular study with different advantages. Here, we focus on the LDA. The early stage of implementations of density functional theory was dominated by one particular

system for which near exact results could be obtained – the homogeneous electron gas. In these systems the electrons are subject to a constant external potential and thus the charge density is constant. The system is thus specified by a single parameter - the value of the constant electron density $\rho = N/V$.

If the electronelectron interaction is approximated by the classical Hartree potential, in which the exchange and correlation effects are neglected, then the total energy functional can be readily computed according to Thomas and Fermi studied.[a] It suggests that in the inhomogeneous system we might approximate the functional as an integral over a local function of the charge density. Using the kinetic and exchange energy densities of the non-interacting homogeneous electron gas will leads to:

$$T[\rho] = 2.87\int \rho^{5/3}(\vec{r})d\vec{r} \tag{2.34}$$

and

$$E_{x\,c}[\rho] = 0.74\int \rho^{4/3}(\vec{r})d\vec{r} \tag{2.35}$$

These results are highly suggestive of a representation for E_{xc} in an inhomogeneous system. The local exchange correlation energy per electron might be approximated as a simple function of the local charge density, $\varepsilon_{xc}(\rho)$. That is, an approximation of the following form,

$$E_{x\,c}[\rho] \approx \int \rho(\vec{r})\varepsilon_{xc}(\rho(\vec{r}))d\vec{r} \tag{2.36}$$

A choice is then to take $\varepsilon_{xc}(\rho)$ to be the exchange and correlation energy density of the uniform electron gas of density ρ . This approach is known as local density approximation (LDA). Within the LDA $\varepsilon_{xc}(\rho)$ is a function of only the local value of the density.

List of software for quantum chemistry

Quantum chemistry computer programs are used in computational chemistry to implement the methods of quantum chemistry. Most of them include the density functional theory (DFT), molecular mechanics or semi-empirical quantum chemistry methods. They may also include

Hartree–Fock (HF) and post-Hartree–Fock methods. They have been usually developed over many years. The following table illustrates the capabilities of the most versatile ten software packages.[b]

Table 3.1: List of quantum chemistry software

Package	Language	Basis set	Mol. Mech[1]	Semi-emp[2]	HF	Post-HF	DFT
CASTEP	Fortran	PW[3]	Yes	No	Yes	Yes	Yes
DMol[3]	Unknown	NAO[4]	No	No	No	No	Yes
ErgoSCF	C++	GTO[5]	No	No	Yes	Yes	Yes
GAMESS	Fortran	GTO	No	Yes	Yes	Yes	Yes
GAUSSIAN	Fortran	GTO	Yes	Yes	Yes	Yes	Yes
MISSTEP	C++	PW	No	No	No	No	Yes
MOLPRO	Unknown	GTO	No	No	Yes	Yes	Yes
ONETEP	Fortran	PW	Yes	No	Yes	No	Yes
Q-Chem	Fortran/C++	GTO	Yes	Yes	Yes	Yes	Yes
TURBOMOLE	Fortran	GTO	Yes	No	Yes	Yes	Yes

[1] Mol. Mech: Molecular mechanics. [2] Semi-emp: Semi-empirical. [3] PW: Plane wave. [4] NAO: Numerical atomic orbitals. [5] GTO: Gaussian type orbitals.

Doml[3] package

Doml[3] is a kind of density functional code for molecules, surfaces, and crystals. Dmol calculates variational self-consistent solutions to the density functional theory (DFT) equations, expressed in a numerical atomic orbital basis. The solutions of these equations provide the molecular wavefunctions and electron densities, which can be used to evaluate the energetic and the electronic and magnetic properties of the system. In addition, evaluation of the energy gradients provides a convenient method for determining the equilibrium geometry of the system. The relatively low computational requirements of the method allow the study of larger molecular systems than would be possible with other *ab initio* methods.

[a] E. Fermi *Z. Phys.* **48** 73 (1928); L. H. Thomas, *Proc. Camb. Phil. Soc.* **23** 542 (1927)
[b] http://en.wikipedia.org/wiki/List_of_quantum_chemistry_and_solid_state_physics_software

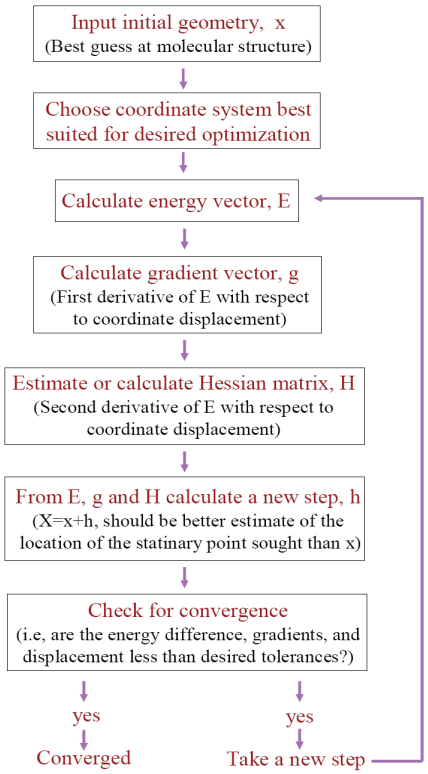

Figure 2.22: Dmol^3 algorithmic process for the geometry optimization. The structure optimization of the molecular junction was performed by minimizing the total energy and the ionic force.

Capabilities of Doml^3 includes but not limited to items such as: (1) energies and binding energies; (2) vibrational frequencies, IR absorption, and constrained optimizations; (3) structural optimizations; (4) polarizabilities; (5) intrinsic reaction coordinate (IRC) finding; (6) densities of states; (7) display of orbitals, densities, and potential; (8) fermi surface. It can be applied to all types of molecular systems, insulating crystals, and surfaces. [a] Dmol^3 algorithmic process for the geometry optimization is shown in figure 2.22.

[a] http://people.web.psi.ch/delley/dmol3.html

2.3 Noise Spectroscopy

2.3.1 Noise-generation Mechanisms

The mechanisms of noise generation can be distinguished by two different phenomena: the spectral density $S_{II}(f)$ depend on the frequency, or not. There are two sources of noise, where the spectral density is independent of the frequency. One is so-called thermal noise, also known as Johnson–Nyquist noise. The second one is known as shot noise.

Thermal Noise and Shot Noise

Thermal noise is generated by the thermal agitation of the charge carriers (usually the electrons) inside an electrical conductor at equilibrium, which happens regardless of any applied voltage. This noise results from fluctuations in the quantum mechanical occupation of electronic states and, as a consequence, from the temperature-dependent statistical distribution of the kinetic energy of the electrons. It leads to a variance of the current despite the fact that the mean value of the current is zero. The resulting spectral density of the auto-correlation is constant for the frequencies relevant in our experiments. The well known Johnson–Nyquist theorem is:

$$S_{II}(f) \approx 4K_B T / R \tag{2.37}$$

In contrast to thermal noise, shot noise is a non-equilibrium effect, i.e. it occurs only when a net current flows. It has its origin in the discrete nature of charge and thus occurs in situations where the current is flowing across a defined barrier. This is the case for example in diodes or vacuum tubes. When an electron hits the barrier, it is either transmitted or reflected, there is no third possibility. As a consequence, the probability distribution of the number of transmitted electrons is binomial and this fact leads to $S_{II}(f) \approx 2eI(1-\alpha)$. For the case of a very small transmission coefficient a, one reaches the Poisson regime and the spectral density is described by the well known Schottky relation:

$$S_{II}(f) \approx 2eI \tag{2.38}$$

Flick noise

One frequency-dependent noise is the so-called flicker noise, often referred as $1/f$ noise. In contrast to the frequency-independent noise (described above) there is no physical theory that describes the flicker noise in a global way. It occurs though in all electronic devices, resistances, semiconductor devices, and so on. There are several processes that can be responsible for this noise: fluctuating particle numbers, e.g. generation–recombination processes in a p–n transition, varying mobility of charge carriers, or fluctuating impurities.[30]

In order to explain the flicker noise behavior, one uses the model of a Lorentz oscillator. The fluctuations arise from elementary processes each having their own time-constant τ. A single process leads to an auto-correlation function proportional to $e^{-t/\tau}$. Hence its Fourier transform represents a Lorentz curve:[30]

$$S_V(f) \propto \frac{1/(\pi\tau)}{4\pi^2 f^2 + (1/\tau)^2} \tag{2.35}$$

After the so called characteristic $f_0 (= 1/2\pi\tau)$ was introduced, the Lorentz curve can be write as

$$S_V(f) \propto \frac{1}{1 + (f/f_0)^2} \tag{2.36}$$

This shows that the single noise density of a single fluctuation is proportional to f^{-2} for $f >> f_0$. For few fluctuators the summation leads approximately to $S_{II} \propto f^{-1}$,see figure 2.23.

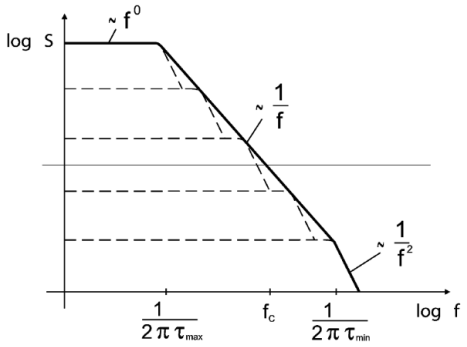

Figure 2.23: Schematic view of the superposition of several Lorentz fluctuators. The $1/f^2$ dependence of the noise of a single process with time-constant t leads effectively to a $1/f$ dependence of the superposition.[30]

Generation-Recombination Noise

An example of a single Lorentz fluctuation is generation-recombination noise, which always appears in semiconducting material. In the solid state physics of semiconductors, carrier generation and recombination are process by which mobile charge carriers (electrons and holes) are created and eliminated.

This type of noise is due to fluctuations in the number of free charge carriers. Impurities in semiconductor material cause discrete energy levels in the band gap and therefore they are able to trap either electrons or holes, or both types of charge carriers. The impurities may act as recombination centers. The term impurity will be assumed to refer both to chemical impurities and to lattice defects such as vacancies and interstices.

The distribution of electrons over the electron states in the impurity levels and the valence or conduction band is governed by Fermi-Dirac statistics. Since this distribution depends on temperature the average number of free charge carriers (holes in the valence band and electrons in the conduction band) is not necessarily a constant. Since the trapping of charge carriers by the impurities or, in other words, since the electronic transitions between the impurity levels and the valence or conduction band occur at random the number of free charge carriers will fluctuate.[84]

These number fluctuations can be probed by applying an electric field and will then cause different Lorentzian shaped *g-r* noise contributions in the spectrum. Such a g-r noise contribution is characterized by two parameters, namely its low frequency plateau value and its characteristic time.

Meanwhile, g-r noise had been found in the metal-insulator-metal tunnel junction. C.T. Rogers *et al* studied the conductance fluctuations of very small area metal-insulator-metal tunnel junction, they have found that the measured voltage noise spectrum can be uniquely resolved into a limited number of distinct Lorentzian conductance noise spectra.[85] They attribute the g-r noise to the slow filling and emptying of localized electron states in the tunneling barrier. Changes in the occupation of such states result in changes of local tunneling barrier and thus in the conductance.

2.3.2 Noise Detection

As in any measurement of electric conductance, the current is not constant in time but exhibits stochastic fluctuations around a mean value. When all external contributions, such as e.g. radiation, are eliminated by screening, the remaining fluctuations are referred to as noise. The corresponding physical quantity (at constant voltage) is the autocorrelation function of the current $K_{II}(t)$ and accordingly its Fourier transform, the spectral density $S_{II}(f)$:

$$K_{II}(t) = \left\langle \Delta I\left(t'\right)\Delta I\left(t'+t\right)\right\rangle \tag{2.37}$$

$$S_{II}(f) = 2\int_{-\infty}^{\infty} K_{II}(t)e^{-i2\pi ft}dt \tag{2.38}$$

Normally, shunt resistance R_S is inserted into the circuit for the current measurement, converting the current into a voltage signal. Then the voltage signal is detected by a spectrum analyzer. The measured voltage fluctuations were accumulated and fast Fourier transformed by the spectrum analyzer, resulting in a voltage noise power spectrum S_V over the bandwidth of interested.

Chapter 3

Material and Devices

In the scope of this thesis, a variety of different chemicals, bio-molecules, solid materials and setups are used. All chemicals were purchased and used without further purification. Purified water with a resistance of 18.2 MΩ (Elix and MilliQ system of Millipore) was used to make aqueous solution and for rinsing. 99.8% nitrogen was used to dry the sample and blow off dirt. Standards solvent such as acetone and ethanol (purity ≥ 99.0%) were purchased from KMF Labochemie and SIGMA-ALDRICH. All lithographic work was done in a class 100 clean room with permanently controlled particle number, temperature and humidity.

3.1 Chemical

Most of the special chemicals are ordered from the company SIGMA-ALDRICH in Germany, as shown in Table 3.1. Here, ethanolic solution of 1mM 11-mercaptoundecanoic acid (MUA), 1,4-benzenediamine(BDA), 1,4-benzenedithiol(BDT), and 1,8-octanedithiol(ODT) were prepared respectively. 10 mM solutions of $ZnSO_4$, $CaCl_2$, and $NiSO_4$ in purified water were also prepared. chloride-free phosphate buffered saline (PBS) was fabricated with Na_2HPO_4 and NaH_2PO_4 (both Fluka ≥ 99.5 %), 100 mM, pH 7.4. To obtain high purity electrolytes, glassware was stored in caroic acid (H_2SO_4, and H_2O_2, 3:1), rinsed and boiled with MilliQ before use. Peptides were dissolved in chloride-free PBS with a peptide concentration of 1mM and stored at -20 ^{0}C.

Table 3.1: Molecules and Chemical

Chemical name	Formula	Purity	ACS number	Company
11-mercaptoun decan-oic acid	$HS(CH_2)_{10}CO_2H$	99%	71310-21-9	Aldrich
1,4-benzenedi-amine	$C_6H_4(NH_2)_2$	99.0%	106-50-3	Aldrich
1,8-octanedi-thiol	$HS(CH_2)_8SH$	97.0%	1191-62-4	Aldrich
1,4-benzenedi-Thiol	$C_6H_4(SH_2)_2$	99.0%	624-39-5	Aldrich
1,4-benzenedi-thiol	$C_{12}H_{10}S_3$	$\geq$ 99.0%	19362-77-7	Aldrich
zinc sulfate monohydrate	$ZnSO_4 \cdot H_2O$	99.9%	7446-19-7	Aldrich
copper(II) sulfate	$CuSO_4$	99.0%	7758-98-7	Aldrich
nickel(II) sulfate	$NiSO_4.H_2O$	99.99%	231-793-3	Aldrich
calcium chloride	$CaCl_2$	$\geq$ 99.0%	233-140-8	Aldrich
dithiobis (C_2-NTA)	$C_{26}H_{42}N_4O_{14}S_2$	96.8%	Code:D550	Dojindo
peptides '3D'	$C_{18}H_{23}N_5O_{11}S_2$	$\geq$ 90%	No	Iris biotech
peptides '4D'	$C_{22}H_{30}N_6O_{14}S_2$	$\geq$ 90%	No	Iris biotech
thiobisben-zenethiol	$S(C_6H_4SH)_2$	98.0%	19362-77-7	Aldrich

The target molecules were integrated between the nanoelectrodes by a self assembly process to generate a metal/molecules/metal junction. For this purpose, 1 mM ethanolic solution of BDT (MUA, BDA, and ODT), was prepared respectively. Also 1 mM peptides in PBS were prepared. For the metal complex experiments, samples were incubated in 0.1mM dithiobis (C_2-NTA) solution for 30 minutes at room temperature followed by washing with deionized water (MilliQ Gradient). After drying with N_2, one set of samples was used without further modification as ion free reference samples. A second set of samples were additionally modified by a 1mM solution of metal ions for 10 minutes. Afterwards, the solution was rinsed off by deionized water and the sample was dried in a N_2 stream.

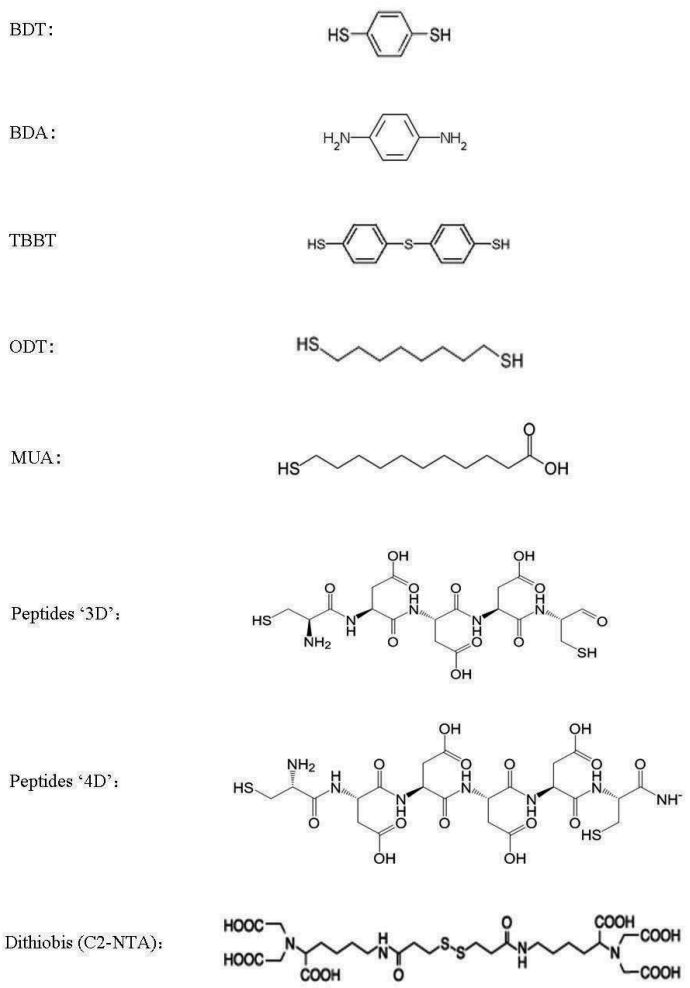

Figure 3.1: The schematic structure of the investigated molecules

In order to fabricate the MCBJ chips, a polyimide layer (HD-4100, HD Microsystem) was used as an isolating layer between the gold electrodes and the substrate. The positive tone resist (PMMA, Polymethylmetacylate 649.04) ordered from ALLRESIST was employed to defined the pattern of the nanoelectrodes. The AR 600-55 brought from ALLRESIST are used for development of patterned e-beam resists.

3.2 Setup and Devices

Clean Room Setup

In order to fabricate the chips for the MCBJ experiment, many devices were employed in the clean room. The Leica Vistec EBPG-5000 Plus lithography system was used for the electron beam writer. PLS 500 evaporation chamber from Balzers was employed for the gold layer deposition. PECVD Plasmalab 100 from Oxford Instruments was used for the Si_3N_4 deposition. Plasma Lab 100 (RIE) from Oxford Instruments was utilized for the polyimide (isolating layer) etching. The software Clewin 4.0 was used for the pattern design.

Mechanically Controllable Break Junction Setup

The main part of the MCBJ set up was fabricated from steel. The overall demission of the system was 90mm × 80mm × 70mm, see figure 3.2. Spring steel was used as the substrate for the chip bending. The two outer posts of the three-point bending apparatus were fixed during the experiment, but their initial position and the distance between them could be adjusted before hand. A Piezo Mikes was chosen as a push rod which can be controlled by a Piezo actuator to move in the Z direction. A beam which can only move up and down along the ditch was inserted between the chip and push rod in order to protect the push rod from mechanical damage and apply a uniform force over the sample width.

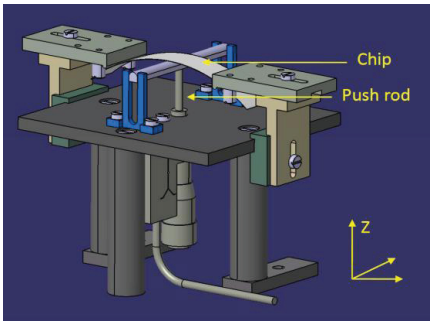

Figure 3.2: The design of MCBJ set up

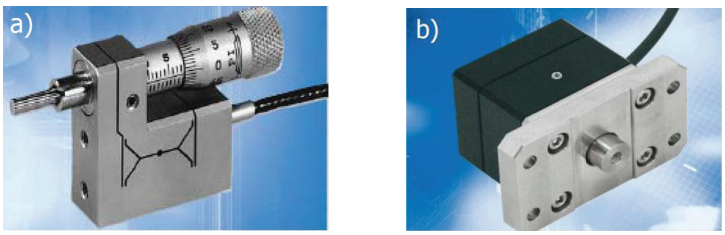

Figure 3.3: a) The picture of push rod, PI P-854. b) The picture of push rod, PI N-110.[a]

Two different piezo drives were employed, see figure 3.3. P-854 (Physik Instrumente PI, GmbH) is a micrometer crew with integrated high-resolution piezo linear drives. It can be operated manually, like standard micrometer screws. The resolution is 10 μm. By controlling the piezo voltage, the micrometer tip moved in and out (up to 25 μm) relative to the manually set position. Resolution of the piezoelectric motion is in the sub-nanometer range. The advantage of such a drive is low price and can the simple operation. The disadvantage is that both manual and automated actuation is needed to break the metal wire.

The second driver is a stand alone piezo driver N-110 (Physik Instrumente PI, GmbH) which facilitates long travel ranges, high stiffness, and high resolution (better than 0.1 nm). Coordinated motion of shear and longitudinal piezo elements is what allows it to break away from the limitations of conventional nanopositioning actuators. The motion in two different modes is possible: a high-resolution mode, and a step mode with theoretically unlimited travel range. In the high resolution mode, motion is provided by high-stiffness shear piezo elements.[b] A generated active force of up to 30 N and a holding force larger than 50 N meet the requirements of our experiment.

[a] http://www.physikinstrumente.com/en/index.php

[b] Please see http://www.physikinstrumente.com/en/products/prdetail.php?sortnr=1000730

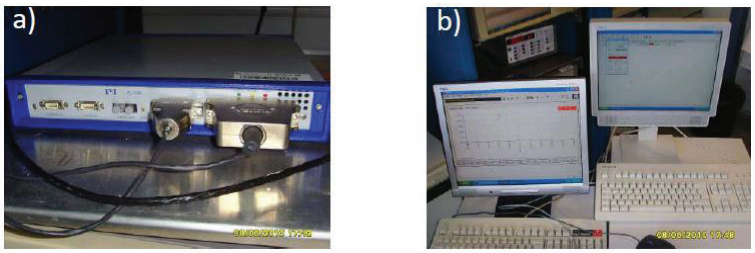

Figure 3.4: a) Piezo actuator of PI E-755 for the push rod of N-110, b) Interface of PI Micromove PIE-755 to control the movement of push rod.

Electrical Characterization Measurement

For electrical measurement, the chip was connected to an external probe station, from which the voltage was applied to the chip and the corresponding current was measured. Here, a drop of metal glue (LEITSILBER 200, DEMETRON GmbH) was used to fix the wire onto the pads. The other side of the wire was connected to the probe station for electrical measurement.

The Karl Suss PM 5 probe station comprises of a stereo microscope, a 6-inch vacuum chuck , 4 micromanipulators, and a light tight enclosure. It can be coupled to various test equipment such as I-V measurements setups. All the current-voltage responses and current-time responses were recorded by the Keithley Multichannel Parameter Analyzer-Keithley 4200 SCS semiconductor characterization system-bought from SÜSS MicroTec. The 4200-SCS performs lab grade DC and pulse device characterization, real-time plotting, analysis with high precision, and sub-femtoamp resolution. Optional Instrumentation include Model 4225-PMU Ultra-Fast I-V Module, which can further improve the performance of the device. With the integrated amplifier, low current as far pA can be measured.

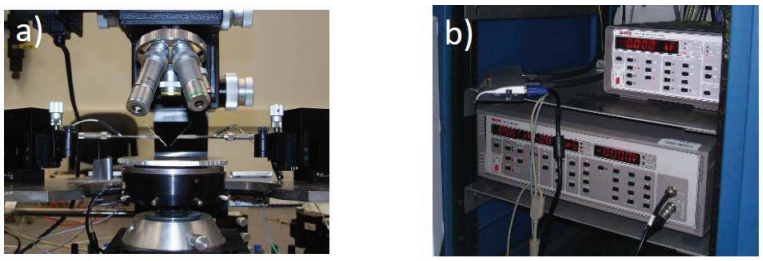

Figure 3.5: a) Karl Suss PM 5 probe station, b) Keithley 4200 SCS Semiconductor Characterization System including Keithley 595 Quasistatic CV meter, Keithley 590 CV analyzer.

Noise measurement system

The noise properties were measured at room temperature in air as well as in the vacuum (10^{-3} mbar) The measurement system was shown in figure 3.6. The bias voltage was applied to the sample using a lead-acid battery and variable 1kΩ resistor. Such low-noise power source allows us to considerably reduce the 50Hz device noise usually registered in conventional units with a 220V source. A capacitance is connected in parallel to the variable resistor to remove its influence on the measured spectra. The sample is connected in series with load resistance, R_{load}. We measured the voltage at the sample, V_S, and the total voltage V_M using a 34401A Digital Multimeter. The current through the sample was estimated by following formula:

$$I_s = (V_M - V_S) / R_{load} \qquad (3.1)$$

Noise signal from the sample was amplified by a home-made preamplifier with a gain of 177 and commercial amplifier (ITHACO 1201) with variable gain. The intrinsic thermal noise of the preamplifier and ITHACO amplifier are measured to $2x10^{-18}$ V^2Hz^{-1} and $2x10^{-17}$ V^2Hz^{-1}respectively. The noise spectra were registered using a dynamic signal analyzer (HP35670A) and the data were transferred through GPIB interface to the computer. If the two multi-meter are switched on and the preamplifier is switched off, the system works under evaluation mode. Under evaluation mode the resistance of the junction can be calculated using $Rsample=V_S/I_S$ as

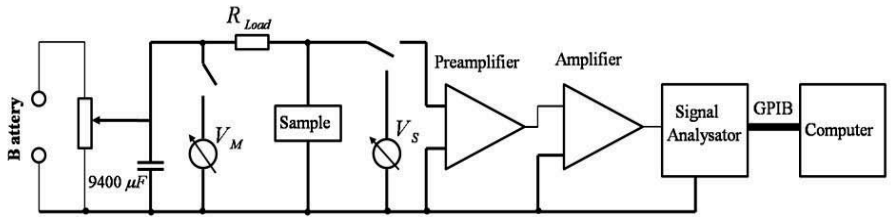

Figure 3.6: The schematic diagram of our measurement system.

a means to evaluate the contact status. On the contrary, If the two multi-meter are switch off and the preamplifier is switch on, the system works under noise measurement mode.

Special software

Doml[3] package, we used to do the DFT calculation, is included in the Materials studio. Materials Studio is software for simulating and modeling materials developed and distributed by the company of Accelrys. Materials Studio offers user-friendly access to a complete range of computational materials science methods. It is designed for research personnel in chemicals and materials. It provides tools for modeling crystal structure and crystallization processes; for property prediction for molecules, polymers, catalysts, and other materials; and for the development of structure-activity relationships. [6]

Materials studio components include but not limited the following items: (1) CASTEP, to predict electronic, optical, and structural properties; (2) ONETEP, to perform linear-scaling density functional theory simulations; (3) DMol[3], quantum mechanical methods to predict materials properties; (4)Adsorption Locator, to find the most stable adsorption sites for various materials, including zeolites, carbon nanotubes, silica gel, and activated carbon; (5) QSAR /QSAR Plus, to identify compounds with optimal physicochemical properties. Here, we use material studio 4.0 to simulate the properties of the ion bridged molecular junction

COMSOL 4.0a was employed to simulate the electrical distribution when the nano gap size was changed. COMSOL Multiphysics (formerly FEMLAB) is a finite element analysis, solver and Simulation software. Multiphysics also offers an extensive interface to MATLAB and its

toolboxes for a large variety of programming, preprocessing and post processing possibilities.[a] The company was founded in July 1986 in Stockholm, Sweden.

[a] http://www.comsol.co-m/

Chapter 4

Experiments Results and Discussion

4.1 Fabrication and Calibration of MCBJ

4.1.1 Marco-wire Fabrication

In this thesis, pair of microelectrdes as well as macroelectrodes was fabricated for the electrical investigation of the molecules. In order to fabricate a pair of macroelectodes, a marcowire was employed. Here, a metal wire with diameter less than 0.25 mm is fixed on the substrate (spring steel) by means of glue or screw. A notch should be made in the middle of the wire in order to make it easy to break when integrated into the MCBJ set up and a force is exerted on it. Usually, there are two methods to make a notch: one is mechanical cutting and another one is electrochemical etching.

Electrochemical Etching

The chemical etching method is shown in figure 4.1. A tungsten wire (diameter 0.5 mm) was immersed in 0.5 M KOH etchant solution at the middle of a platinum loop (Alfa Aesar, 99.8%), which was set at the solution surface. An AC voltage (40 V, 40K Hz) was applied between the tip and the loop, so that the tip was the anode and the loop was the cathode. Due to the applied voltage, the tungsten wire was electrochemically etched. [86]

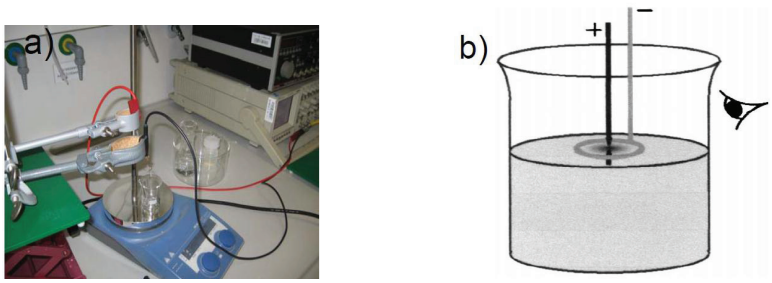

Figure 4.1: a) The set-up for electrochemical etching. b) The electrochemical apparatus for tungsten etching to make a notch.

The etching speed and configuration of the notch not only depend on the AC voltage but also on the concentration of the KOH solution. Because of the chemical etching, a notch normally appeared after about 10 minutes. The metal wire was released from the set-up before the complete break from the notch part. After etching, the diameter of the notch can be reduced to less than 0.05 mm.

The configuration of the tungsten notch is shown in figure 4.2. The wire was fixed on the substrate and the chip was integrated into the MCBJ set-up. Actually, by the electrochemical method, different kinds of metal wire can be etched, for instance, a AC voltage (50V, 40k Hz) combined with $CaCl_2$ and HCl solution can be used to etch Pt wire;[87] and a AC voltage (30V, 50k Hz) combined with HCl and ethanol solution can be used to etch gold wire.[88]

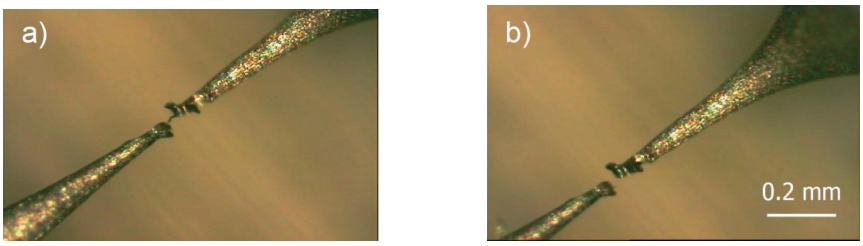

Figure 4.2: The configuration of the tungsten notch before break (a), and after break (b) using MCBJ set up.

Mechanical Cutting

Another traditional method to make a notch is to use the mechanical cutting. This method is more suitable for metal wire with less stiffness, such as gold and silver wire. Here, a gold wire with 50 μm diameter was mechanical cut in order to make a notch.

Since the diameter of the gold wire was so in the sub-millimeter range, the operation of mechanical cutting was done under the microscopy, see figure 4.3. A knife with sharply blade was used to cut the gold wire. Control of the force exerted on the knife allowed the gold wire to be mechanically cut down without completely breakage.

Figure 4.3: a) The set up for mechanical cutting a gold wire in order to make a notch. b) SEM picture of the gold wire with a notch in the middle by mechanical cutting.

4.1.2 MCBJ Chip Fabrication

Spring steels sheets (length of 44 mm, width of 12 mm and thick of 0.2 mm) were used as the substrates the similar to the traditional method. All the fabrication process was done based on such a substrate. A flexible isolating layer consisting of polyimide was spin coated onto the spring substrate. Electrode structures containing a thin bridge with a constriction of 30-50 nm were defined by e-beam lithography. After the lift off of a 40 nm thick gold film, the polyimide was locally removed by reactive ion etching in order to generate a suspended metal bridge. The fabrication process is shown in figure 4.5.

Isolating Layer

At first, the substrate was cleaned in propanol solution followed by washing in an acetone baths with ultrasonic agitation. Then a polyimide layer (HD-4100, HD Microsystem) about 2 μm thick, was spun on the substrate in two steps. First, the polyimide layer was spin coated at a speed of 3000 rpm. To complete the imidization of the polyimide, the substrate was baked in the oven at 200 ^{0}C for half an hour. A second layer of polyimide was spun on to the substrate at the speed of 4000 rpm in order to reduce the probability of shorts and defects through the polyimide. Finally the substrate was annealed for two hours at 350 ^{0}C and 0.01 mbar.

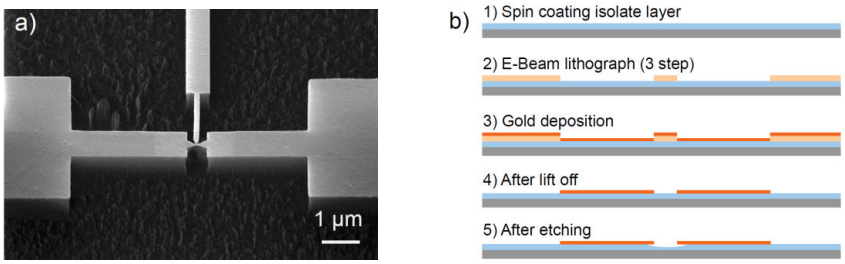

Figure 4.5: a) The SEM picture of the chip fabricated by E-beam lithography, and the b) schematic of five steps to fabricate MCBJ chip.

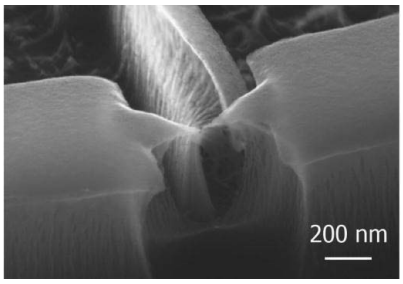

Figure 4.6: the SEM picture of the chips without the anneal process at high temperature. After etching, a strong deformation of the polyimide layer was observed.

The two hours anneal process at 350 ^{0}C was necessary in order to harden the polyimide layer. Otherwise, the polyimide layer, which support the electrodes, would have some deformation after the RIE, especially in the parts below the reference electrode as shown in figure 4.6.

The polyimide was used for few reasons: first, it planarizes the spring steel substrate surface; second, it serves as an insulating layer between the metallic pattern and the substrate; third, it can be reactive iron etched to get a free standing bridge, and finally the polyimide conserve its mechanical properties in a large temperature range. Another kind of polyimide (PI 2610 HD Microsystem) was also tested. Only small difference was observed in the thickness after spin coating and the roughness after reactive iron etching process. Later, Si_3N_4 was also tested as the isolating layer in the Raman scattering experiment (see supporting imformation), from which the back ground signal from polyimide was excluded.

E-beam lithography process

The e-beam lithography process consists of three steps. First, 200 nm positive resist (PMMA, Polymethylmetacylate 649.04 from ALLRESIST) was spin coated onto the substrate, and baked at 180 ^{0}C for 2 minutes. Second, the designed pattern was written by a Leica Vistec EBPG-5000 plus lithography System. Finally, a standard development procedure was applied by inserting the substrate into development solution (ALLESIST AR 600-55) for 50 S, after which the substrate was transferred into propanol to stop the development.

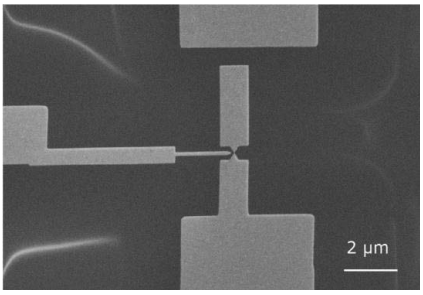

Figure 4.7: The magnetic field effect in the e-beam writing process.

The pattern was written in two steps: the first fast e-beam writing step was used to define the coarse structure layer (see appendix B). The second slow e-beam writing step was used to define the fine structure layer. During the e-beam writing process, the electron beam drifted because of magnetic field effects from the spring steel substrate. In some cases, the two layers mismatched each other since different beam current were used to define the two layers, see figure 4.7. We overcame this problem by two strategies: one was to increase the thickness of the isolating layer to reduce the magnetic field effect; and the other was to increase the overlap area between the two layers in the pattern design process.

After development the resist layer served as a mask for the metal deposition. At this step, 2 nm Ti and 40 nm Au layers were deposited on the substrate surface by physical vapor deposition (Pfeiffer PLS 500 Aufdampfanlage). After deposition of the metal, the sample was immersed in acetone to remove the PMMA mask. The acetone can be warmed to improve the lift-off process.

Reactive-Ion Etching

In the final step, the polyimide was reactive-ion etched to obtain a suspended metal bridge. This was done by reactive iron etching for 10 minutes under the following conditions: 32 sccm of O_2 and 8 sccm of CHF_3; a power of 100W; a pressure of 0.025 torr and bias voltage -365 V.

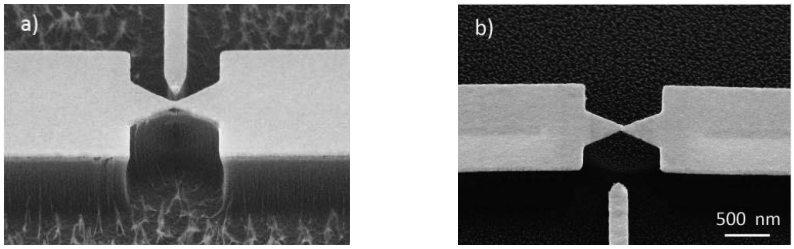

Figure 4.8: Top view SEM picture of the chips. a) Polyimide layer was etched by O_2 and CHF_3, grass like geometry above the residual layer was observed. b) A smooth surface was obtained when the polyimide layer was etched by pure O_2.

The surface roughness of the polyimide was largely determined by the etching process, especially by the gas composition of the etchants. A grass like surface was observed when the polyimide layer was etched by a mixture containing 80 % O_2 and 20% CHF_3, while, a smoother surface was obtained when the polyimide was etched by pure O_2, see figure 4.8. We attribute the grass-like surface to the reaction between the polyimide and fluorine-containing gas CHF_3, which resulting the Teflon formation.

Cell Fabrication

Since electrical measurements in a liquid environment were necessary, a cell above the chip was fabricated, which could hold 50 μL of solution. At first, a 10mL silicone elastomer (Dow Corning, LOT: 0006148926) and 1mL silicone elastomer curing agent (Dow Corning, USA) were mixed. Then the mixture was put into a low pressure vacuum to get rid of air bubbles. After loading the mixture in the home-made mold, it was cured at 150 ^{0}C for 2 hours. The cell with an opened window was fabricated after it was peel off from the mold.

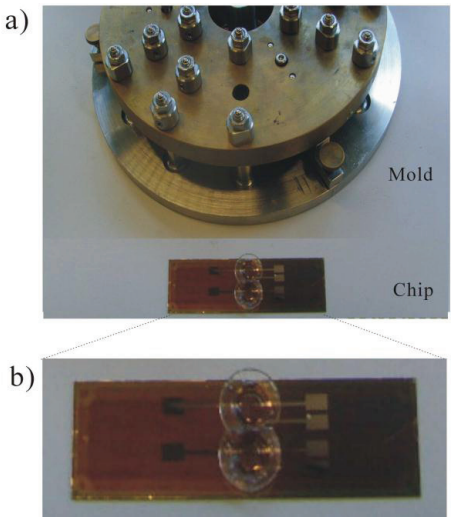

Figure 4.10: Cells fabrication and attached at the chip surface. a) The mold for the cell fabrication and b) the chip with fabricated cell on the surface

A silicone adhesive was needed to attach the cell to the substrate of the chip. Here, 10 mL silicone adhesive (Dow Corning, USA) and 1mL silicone adhesive curing agent were mixed. After getting rid of air bubble in vacuum, the mixture was used to glue the cell to the chip, which was then cured at 100 ^{0}C for 3 hours. Since every chip was fabricated with two junctions in parallel, each chip was attached with two cells also, see figure 4.10.

When a metal electrode is introduced into an electrolyte solution, a electrochemical double layer (compact layer and diffuse layer) will form at the solid/liquid interface.[89] With each change of electrode potential, the rearrangement of ions in the double layer at the electrodes surface causes a transient current through the electrode. These processes are termed ‘‘non-Faradaic processes’’ or, since they are similar to charging and discharging currents of an ideal capacitor, called ‘‘capacitive currents’’. On the other hand, chemical reactions may occur between ions in the electrolyte and the electrode surface. These processes are called ‘‘Faradaic processes’’. These flow across the solid/liquid interface for example when reduction or oxidation of the surface material occurs.

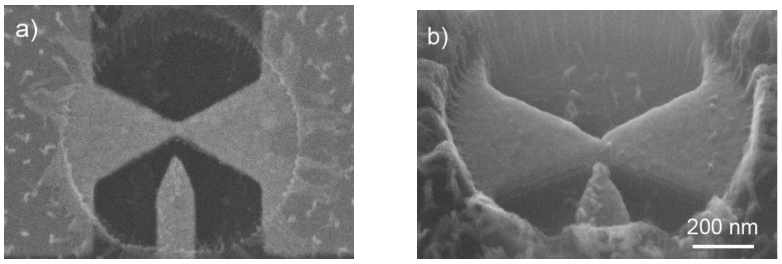

Figure 4.11: SEM picture of the chip with an opened window above the chip, the area beyond the window was coved by PMMA. a) Top view of the chip. b) Side view (45 degree) of the chip.

In order to reduce the parasitic charging or Faradaic currents, the electrode surface area exposed to liquid should be minimized. Therefore, a second e-beam writing step was performed, in which the main part of the electrodes were covered by PMMA and only a very small part (micrometer square area) were exposed to the liquid. In the second e-beam writing process, 1.2 μm positive resist (PMMA, Polymethylmetacylate 671.07 from ALLRESIST) was spin coated onto the substrate, and baked at 180 ^{0}C for 2 minutes. After the second e-beam writing process, an opening window was generated at the junction area and the area beyond the window was coved by PMMA, see figure 4.11.

4.1.3 Attenuation Factor Calibration and Stability Test

Attenuation Factor Calibration

The biggest advantage of the MCBJ is the outstanding stability because of the geometry of the setup. The chips were mounted into a home-made three-point bending apparatus. The two outer posts of the three-point bending apparatus are fixed while the third one works as push rod in Z direction. When the push rod exerts a bending force on the substrate, the movement in Z direction causes an elongation of the constriction until the break of the bridge resulting in formation of two separated nanoelectrodes, as illustrated in figure 4.12.

Precision of the gap control is determined by the attenuation factor, $r = \Delta x / \Delta z$, where Δx is the gap change and Δz is the push rod displacement.

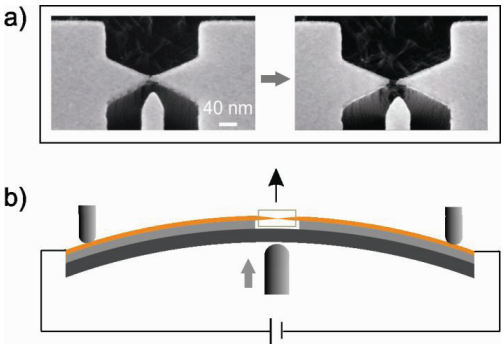

Figure 4.12: Working principle of the MCBJ and calibration of attenuation factor. a) Top view: scanning electron microscope (SEM) image of a micro-fabricated MCBJ chip consisting of a freestanding metal bridge, with a central constriction, on top of an insulating spring steel substrate. A nano-gap appeared after the central constriction broke as the push rod applied a force to bend the substrate. b) Side view: schematic of the MCBJ sample mounted into a three-point bending mechanism. The push rod exerts a bending force to bend the substrate. The bending force breaks the metal bridge at the smallest constriction resulting in the formation of a break junction.

The attenuation factor will is: $a = \Delta x / \Delta z \approx 6ut / L^2$, according to Zhou *et al.*[90] Here, a is attenuation factor; Δz is the displacement of the push rod; Δx is the gap size change between the two nano electrodes; u is the length of the suspend bridge; t is the thickness of the steel substrate; L is the length between the two out support point. The schematics structure of the MCBJ and chips were shown in figure 4.13.

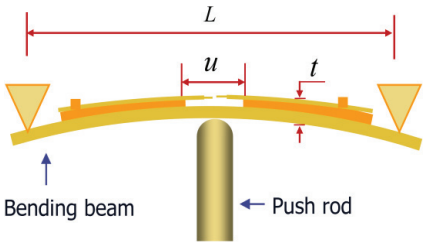

Figure 4.13: The schematic structure of the MCBJ.

For our device, u was approximately 900 nm, t was approximately 0.22 mm, and L was 18 mm, so $a \approx {6ut}/{L^2} \approx 4\times10^{-6}$ was obtained. Another method to calibrate the attenuation factor is to analyze the tunneling current/distance curves of the bare gold/air/gold junction.

The tunneling current changes with the displacement of the push rod was shown in figure 4.14. At low bias voltages the tunneling current can be described by the equation:

$$I \propto \exp(-2d\sqrt{2m\phi}/\hbar) \tag{4.1}$$

Here, d is the gap size, m is the electron effective mass, ϕ is the barrier height. Equation 4.1 can be written as:

$$I \propto \exp\left[-1.02d\sqrt{\phi}(eV)^{-0.5}\,\mathring{A}^{-1}\right] \tag{4.2}$$

After the gap size was changed from d_1 to d_2, the turrrenting current changd accordingly from I_1 to I_2. We can obtain:

$$\frac{I_1}{I_2} \propto \exp\left[1.02(d_1-d_2)\sqrt{\phi}*(ev)\dot{A}^{-1}\right] \tag{4.3}$$

According to 4.3, a gap size change of $\Delta d = d_1 - d_2 = 1.5\,\mathring{A}$ will result in a one order decrease of the tunneling current, if we fixed ϕ_B to a value of 2.0 eV.[91] The responding displacement of the push rod was determined to be 30 μm as shown in figure 4.14. So the attenuation factor

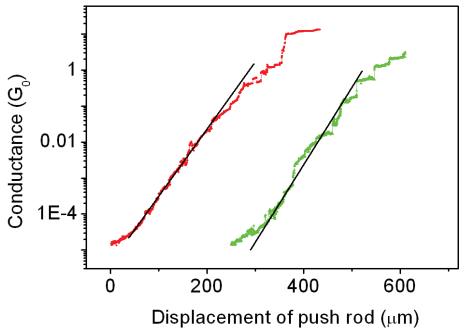

Figure 4.14: Attenuation factor calibration by the measurement of tunneling current.

should be $a = \Delta x / \Delta z = 1.5\,\mathring{A} / 30\,\mu m = 5 * 10^{-6}$. This value agrees with the result determined by the structure estimation of MCBJ.

Stability Testing

Although a notch can be fabricated by mechanical cutting or electrochemical etching based on a macrowire. These samples were not suitable for the measurements of molecule properties because of their stability. The method to attach the metal wire on the substrate by gluing did not fix the wire on the substrate completely. Actually, shifting of I-V curves in the tunneling regime was observed even when the push rod position was fixed for these chips. This means that the gap size was not constant over time. We attribute this observation to the plastic deformation of the glue under the external force. Figure 4.15 reveals that we can not control the gap size between the two electrodes precisely with such a chip. The chips fabricated by the electron beam lithography can overcome this disadvantages described above.

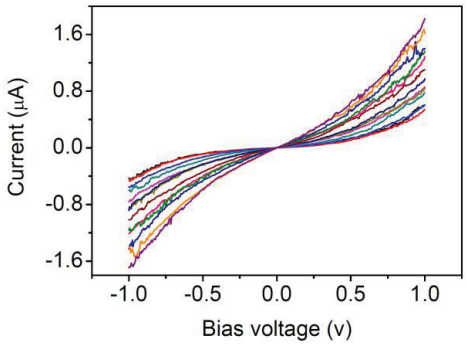

Figure 4.15: Fixed the push rod position, The shift of I-V curves was observed, indicating the gap size is not constant.

In contrast, MCBJ fabricated by lithography shows outstanding stability. The stability of MCBJ was demonstrated in two aspects: individual gold atoms, bridging two nanoelectrodes before the complete break of the gold wire, can be maintained longer than one minute at room temperature. After breaking of the gold wire, the gap size can be kept almost unchanged for several hours ($\Delta d < 1\mathring{A}$).

Right before the break occurs, the two electrodes are bridged by a single or few gold atoms. Typically the conductance decreases discontinuously as a function of time. Many conductance traces show plateaus near integer multiples of $G_0 (G_0 = 2e^2 / h)$, and often the last plateau in the contact regime is approximately $2e^2/h$, which corresponds to single conductance channel. This quantized conductance was only observed in the case when the length of the conductor is smaller compared to the mean free path of the electron.[92]

This quantum conductance could be maintained for longer than one minute with our setup even at room temperature demonstrating that we have achieved very high mechanical stability, see figure 4.16. After breaking the constriction, the electron transport is controlled by a tunneling process. The two electrodes can be bought close to each other again by relax the substrate. When the electrodes are brought closer enough together, a direct Au-Au contact can be formed again. Such a breaking and reconnecting process can be repeated hundred times.

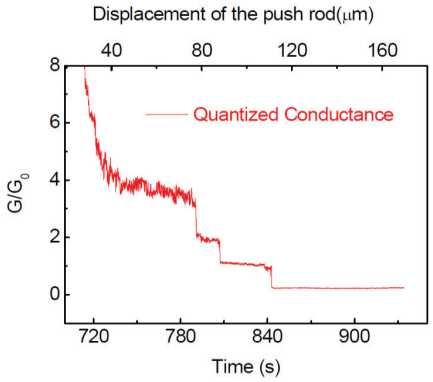

.

Figure 4.16: During the breaking process of the constriction, the two emerging nanoelectrodes were bridged by only few gold atoms right before the final breaking occurs. The corresponding quantized conductance can be observed.

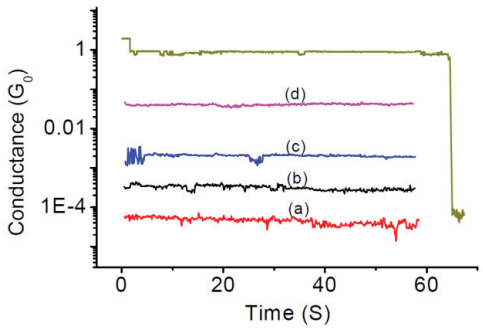

Figure 4.17: The conductance G_0 can be maintained more than one minute by controlling the movement of the push rod. After the breaking of the constriction, two separated nano electrode were created. The two electrodes can be bought close to each other and the corresponding tunneling current increase was monitored (a-d).

Like STM, the junction gap can be set to a certain size by adjusting a corresponding tunneling current. This current can be hold constant for a longer time when the push rod is fixed as shown in figure 4.17. The absolute value of the gap size is difficult to determine since the gold atoms rearrange after complete breaking of the metal constriction. However, relative changes can be made with high accuracy.

4.2 Noise Spectroscopy of Molecular Junctions

Employing MCBJ set up, a pair of nano electrodes with precisely controlled gap can be obtained. Integrating the target molecules, which have bonding group at both ends, into the nano gap, a metal/molecule/metal junction can be achieved.[75] The noise properties of metal/molecule/metal junctions were investigated in this work. As a reference to molecule containing junctions, the molecule free junctions were investigated firstly.

4.2.1 Noise Spectroscopy of Molecule Free Junctions

The noise characteristics of bare metal break junctions were precisely investigated from the diffusive to the ballistic transport regime by Z. M. Wu et al.[29] Here, we focus on the investigation of noise properties of MCBJ samples at room temperature (T~298K) in the tunneling regime, after the formation of the gap. Voltage fluctuations were measured and Fourier transformed using a dynamic signal analyzer.

Firstly, the junctions were connected to the measurement system under evaluation mode where the resistance of the junction was measured and the status of the junction can be evaluated. Then the system was switched to noise measurement mode. The measured voltage fluctuations were accumulated and fast Fourier transformed by a spectrum analyzer, resulting in a voltage noise power spectrum S_V over a bandwidth from $1\,Hz$ to $100\,kHz$. After the noise response of a certain configuration was determined, the setup was switched back to evaluation mode and the status of junction was evaluated again. Only those data were further analyzed where the status of junction before and after noise measurements were consistent.

The noise spectroscopy at different gap size was shown in figure 4.18. For small gap sizes, the spectra follow exclusively $1/f^{\alpha}(0.9 \le \alpha \le 1.2)$ noise behavior which agrees with results previously reported. For larger gap sizes, the thermal noise becomes dominant over the $1/f$ noise at high frequencies. The total noise can be expressed by the following empirical equation:

$$S_V(f) = \frac{A}{f^{\alpha}} + 4kTR \tag{4.4}$$

Here, k represents the Boltzmann constant, T the temperature, R the effective resistance of the gap, and A the level of $1/f$ noise at 1Hz. The first term of equation (1) describes the $1/f$ noise while the second frequency independent term corresponds to the thermal noise. With increasing gap sizes (decreasing tunneling current), A becomes smaller and R becomes bigger, both resulting in a dominant thermal noise component at high frequencies

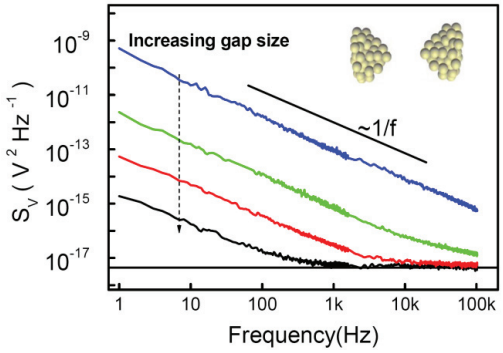

Figure 4.18: The voltage power spectra density in the tunneling regime, with a variable gap size between bare gold nanoelectrodes. The fixed bias voltage applied to the junction is V_B = 20 mV. The horizontal black line represents the theoretically calculated thermal noise (4kTR). The spectra follow exclusively $1/f^{\alpha}(0.9 \le \alpha \le 1.2)$ noise behavior. The noise component decreases to the thermal noise level as the gap size is increased**.**

4.2.2 Noise Spectroscopy of Molecule Containing Junctions

The noise spectroscopy of single molecular junction was initial investigated by H.B.Weber group, and the generation-recombination (G-R) noise was revealed for the first time. While the underneath mechanism which cause the G-R noise is still unclearly so far. In order to clarify what is causing G-R noise, the molecules with varied bonding groups and different electronic structure are employed. For this purpose, an ethanolic solution of 1 mM 1,4-benzenedithiol (BDT), 1,8-octanedithiol, 1,4-benendiamino, 11-mercaptoundecanoicacid(MUA) were prepared. All these molecules contain two thiol termini or one thiole as well one amino or carboxy termini as binding groups. The junctions were prepared under protective atmosphere with an oxygen level of less than 0.6 ppm.

The molecular junction with 1,4-benzenedithiol (BDT) was firstly investigated. The solution contain BDT was placed on the junction area under argon atmosphere, while the two electrodes were kept a few nanometers apart. After self-assembly of the molecules on the gold surface of the nanoelectrodes, the samples were thoroughly rinsed with ethanol and dried in nitrogen stream.

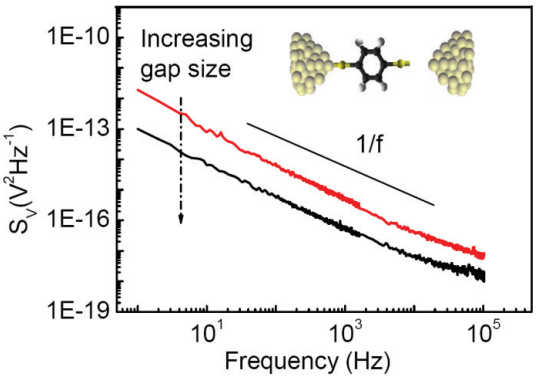

Figure 4.19: The noise power spectral density measured for the case when the gap size between nanoelectrodes is larger than the molecule dimension. The spectra follow $1/f^{\alpha}(0.9 \le \alpha \le 1.2)$ noise behavior similar to molecule free junctions. The noise decrease as the gap size was increased.

The junctions were subsequently connected to the noise measurement system. Using the push rod, we can easy precisely control the gap size between the electrodes. In the case of the gap size being larger than the size of the molecule, only $1/f$ and thermal noise component were observed, similar to molecule free junctions, as shown in figure 4.19.

When the two separated electrodes were brought closer together until the gap had the dimension of the length of the molecules, the tunneling current suddenly jumped to a stable lock-in state where the current became almost independent of the gap size, see figure 4.20. The resistance of the junction in this configuration was determined to be 1.4 ± 0.3 $M\Omega$ for BDT, corresponding to the resistance of a single molecule, as reported earlier.[93] It can be assumed that in this configuration a single molecule is bridging the nano-gap by establishing a covalent bond to both opposing electrodes.

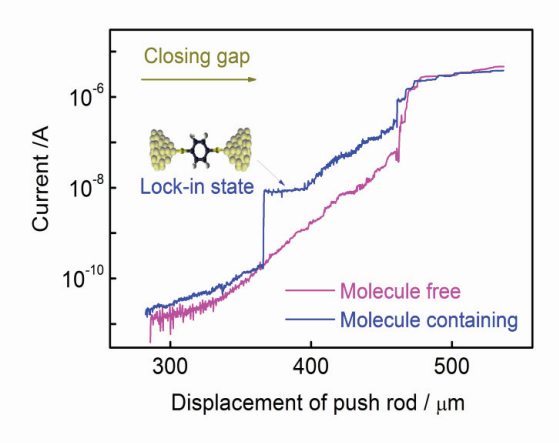

Figure 4.20: The curves present the tunneling current change in closing periods of junctions. In the case of molecule containing junction (blue curve), and the current jumps to a lock-in state during the closing period. In the lock-in state the current is almost independent of the gap size. In contrast, the lock in state was absent in the molecule free junction (gray curve).

In this state the setup was switched to noise measurement mode and the noise characteristics were recorded. Surprisingly, in additional to the $1/f$ response, a new noise component was revealed for the BDT bridged nanogap, see figure 4.21. In order to analyze the resulting noise spectra, a $1/f^2$ dependent noise component was introduced corresponding to a single Lorentz oscillator. The noise characteristics can be now described as the superposition of a $1/f$ noise, a $1/f^2$ dependent noise and thermal noise component in the form:

$$S_V(f) = \frac{A}{f} + \frac{B}{1+(f/f_0)^2} + 4kTR \qquad (4.6)$$

Here, B represents the level of $1/f^2$ noise for $f \to 0$. f_0 , the so called characteristic frequency or corner frequency, is derived from the inflection position of the noise spectra. Equation 4.6 provides a perfectly fitting model of the experimental data, see figure 4.21(a). For BDT we determined the characteristic frequency f_0 to be 1200 Hz by plotting $(f * S_V)$ versus f (not shown).

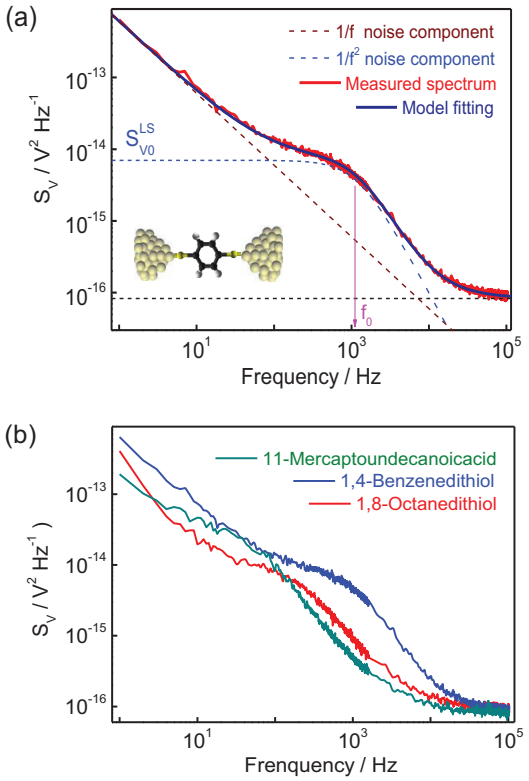

Figure 4.21: (a) The voltage noise power spectral density of the molecule containing junction in the lock-in state, corresponding to a single benzendithiol bridging two electrodes (cartoon). The solid red curve is the measured noise density and solid blue curve presents the model fitting. The fitting curve is described as the superposition of a $1/f$ noise, a $1/f^2$ noise and thermal noise components, shown by brown dash line, blue dash curve, and black dash line, respectively. (b) The noise spectra measured for MCBJ with different molecules at single molecule level. The characteristic frequency, f_0, was obtained by plotting $(f * S_V)$ *vs* f, and found to be of $1200\,Hz$, $270\,Hz$, $70\,Hz$ for 1,4-benzendithiol, 1,8-octanedithiol, 11-mercaptoundecanoicacid (MUA), respectively.

We performed similar study of the current and noise characteristics for different molecules bridging the nanocontacts, see Figure 4.21 (b). For each type of molecules we measured at least

3 different MCBJs with the same molecule. Each noise spectrum was obtained by averaging of 100 curves using spectrum analyzer. For flicker noise component, we registered that the noise spectral density scales quadratically with current in both molecule free and molecule contain junctions. For the Lorentzian-shape noise component, the linear dependence on current was obtained. The results are shown in figure 4.22.

For all studied molecules, a $1/f^2$-noise component was registered. The measured characteristic frequencies f_0 are summarized in Table 4.1 together with characteristic parameters for studied

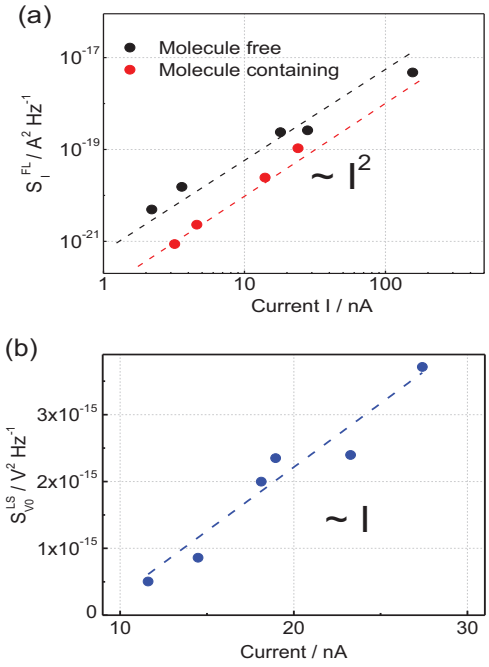

Figure 4.22: The noise spectral density, obtained at f=1Hz from measured noise spetra, of (a) flicker component of noise, S_I^{FL} , has quadratic dependence on current in molecule free as well as molecule containing junctions, (b) the Lorentzian-shape noise component, $\boldsymbol{S_{V0}^{LS}}$, plateau has linear dependence on current. Results are shown for 1,4-Benzenediamine molecule bridged the nanogap of MCBJ at fixed gap size between two nanoelectrodes.

molecules**.** Analyzing the data listed in the table, one can see that there is no correlation between the characteristic frequencies and the bonding energy of the binding groups and gold nanoelectrodes. While the characteristic frequencies increase as the energy gaps $(E_F - E_{MO})$ of the molecule junctions decrease. Moreover, we found that $\ln(f_0)$ is a linear function of $(E_F - E_{MO})$, i.e., the characteristic frequency depends exponentially on the energy gap. Note, the current transferred via a single molecule is also affected by the energy gap.

Table 4.1: The molecules with different bonding groups and the electronic structure parameters investigated by measuring the current and noise spectra

Molecules[a]	E_F-E_{HOMO} (eV)[b]	f_0 (kHz)[c]	ln (f_0) (Hz)	Bond strength (kJ/mol)[27]	Bond type
MUA	1.8 [c]	0.07 ± 0.01	4.2	20	Au-COOH
ODT	1.4	0.27 ± 0.03	5.6	134	Au-S
BDT	1.2	1.2 ± 0.2	7.0	134	Au-S
BDA	1.0	1.4 ± 0.2	7.2	36	Au-NH_2

[a] MUA, ODT, BDT, BDT represent 11-mercaptoundecanoicacid, 1,8-octanedithiol, 1,4-benzenedithiol, 1,4-benzenediamine, respectively. [b] $E_F - E_{HOMO}$ is the energy gap between the Fermi level of the gold electrodes and HOMO state of the molecules, obtained by fitting measured I-V curves using Simon's equation. The values are in the range reported in the literature for ODT There was no found reported value of the energy gap for MUA in the literature.[94-96] [c] Characteristic frequency, f_0, was measured at fixed bias voltage.

Furthermore, we have measured and analyzed the character of time-dependent voltage fluctuations of the nanojunction bridged by a single molecule. Results obtained for the case of the octanedithiol (ODT) molecule trapped into the junction gap are shown in figure 4.23. From measured voltages fluctuating in time (shown in inset to figure 4.23) we calculated the probability of finding voltages with certain amplitudes. The probability curve has two well resolved maxima, A and B, corresponding to low-voltage and high-voltage states, respectively. The relative probability of finding the system in states A and B is $P_A/P_B \approx 11$. The low-voltage and high-voltage states differ by ≈ 14 μV at the applied bias voltage 20 mV.

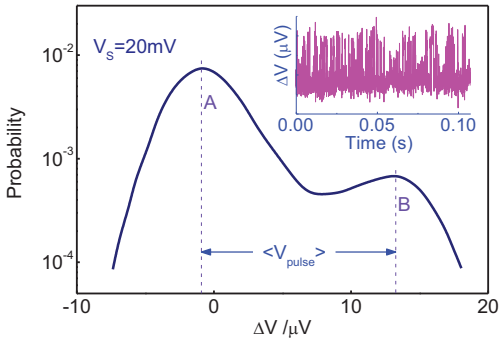

Figure 4.23: Voltages fluctuating in time and calculated the probability of finding voltages with certain amplitudes demonstrating two well resolved maxima, A and B. Inset: voltage dependence on time measured at applied voltage V_S=20 mV. Results are shown for ODT molecule bridged the nano gap of MCBJ. The histogram was built based on measured 160000 points and analyzed with 50 nV bin size. The total probability sums to 1.

We measured noise characteristics for stable in time lock-in state of the current, which is attributed to the charge transfer via individual molecules. Separating the $1/f$ noise of the gold electrodes and the thermal noise from the whole noise spectrum, we found $1/f^2$ noise component that specifically inherent for a single bridging molecule. The values of f_0 do not correlate with the energies of the bonding strength between molecules and gold electrodes. While, frequencies f_0 correlates with the electronic structure of the molecules, particularly, $\ln(f_0)$ is a linear function of $(E_F - E_{MO})$. It is worth to note, that the current transferred via a single molecule is also essentially determined by the same value $(E_F - E_{MO})$. Analysis of time-dependent voltage noise has shown that voltage fluctuates mainly between two values. Difference between two most probable voltage amplitudes is relatively small (about three orders of magnitude smaller than the average voltage in the lock-in state).

Kim with coauthors have shown that the trapping and detrapping events via localized states can be neglected when the applied bias to the molecular junction is below 400 mV.[97] Registered in

our experiment $1/f^2$ noise component in a low-bias range relevant to a single bridging molecule can be understood as a result of a dynamic reconfiguration of molecular coupling to the metal electrodes. It should be noted, that different electric properties of single-molecule-junction systems were explained by the dynamic reconfiguration in these systems (see, for example [98-100]). For the molecule bridged junctions studied in this work, low values of the characteristic frequencies, absence of correlations between f_0 and the bonding strengths and small amplitudes of the voltage fluctuations specify the following physical picture responsible for the single molecule noise. The coupling reconfiguration of the bonds occurs, rather, without total bond breaking. Instead, the coupling group has two near positions, i.e., stable and metastable configurations with different but close conductance. These configuration states are separated by a low energy barrier in comparison with the bonding strength. Thermal motion of the electrode atoms and charge transfer via the molecule induce random and rare in time transitions between these configuration states. Furthermore, the flowing current induces additional energy and momentum into the system which can trigger conformational changes of the molecule and metal contact atoms.[28] These structural fluctuations are feed back to the electron transport probability, which can be considered as reason of the observed voltage fluctuations.

Rare in time transitions between stable and metastable coupling configurations allow to describe resulting electric noise by the phenomenological model of a single Lorentz fluctuator. Indeed, as it was shown the system almost all the time is nearby the stable configuration. Thus, to consider revealed fluctuations one can analyze small changes in the coupling configuration. We start with discussion of the surprising fact of small frequencies of observed $1/f^2$ noise. All existing times characterizing motion of electrons and nuclei in molecules and metal contacts under equilibrium, as well as relaxation times in contacts, are smaller than registered characteristic noise times ($\sim 1/f_0$) by many orders of values. We shall assume that large values of the characteristic noise times are related to non-equilibrium processes in molecules induced by low currents. These processes can be considered as follows. When current flows through a molecule, the electron subsystem of the latter becomes polarized. The processes induce small structural/configuration changes. The charge transfer and structural/configuration changes are coupled. Small currents determine smallness of the forces inducing the changes and, thus, large characteristic times of these changes. Let $X(t)$ be the configuration coordinate, generally dependent on time t. The

junction resistance is supposed to be a function of X: $R=R[X(t)]$. Then, fluctuations of X lead to changes in the resistance: $\Delta R(t) = (dR/dX)\ \Delta X(t)$. Assume the current J is constant, then fluctuations of the voltage V is $\Delta V(t) = J\ \Delta R(t)$. In frequency domain, the spectral density of voltage fluctuations is $S_V(f) = (\Delta V)_f^2 = J^2\ (\Delta R)_f^2$.

To write down an equation for $X(t)$, one can follow the phenomenological approach developed in Reference (Landau, and Lifshits).[101] The approach is based on the existence of a system with two sets of strongly distinct characteristic times: due to short relaxation times the system reaches the so-called "incomplete equilibrium", then it slowly ("quasistationary") relaxes during a longer time. For this situation the Lorentz fluctuator can be introduced. According to the above analysis, the system under consideration just possesses very distinct characteristic times and we can apply the approach of Landau and introduce the following equation for the configuration coordinate, $X(t)$,

$$dX/dt - \lambda X = \xi(t). \tag{4.7}$$

Here λ (>0) describes slow relaxation of X, $\xi(t)$ is a ''random force'', the correlator which is proportional to λ, $\langle\xi(0)\xi(t)\rangle = 2\ \lambda\langle X^2\rangle\ \delta(t)$ with $\langle X^2\rangle$ being total thermal fluctuation of the quantity X. From these equations we readily obtain the spectral density of voltage fluctuations in the Lorentz form:

$$S_V(f) = 2J^2\left[\frac{dR}{dX}\right]^2 \frac{\langle X^2\rangle}{\pi f_0}\frac{1}{1+(f/f_0)^2} = \frac{B}{1+(f/f_0)^2} \tag{4.8}$$

where $f_0 = \lambda/(2\pi)$. Since non-equilibrium processes (i.e. the current) are responsible for the large times and λ describes the rate of relaxation, we can assume that λ is proportional to J. Then, the proposed model predicts that $f_0 \sim J$ and $S_V(f) \sim J$. The first relation explains the correlation between the characteristic frequencies f_0 and the electronic structure (energy gap) of the molecules determining the current in the system.

Thus, the developed phenomenological model, bases on the assumption of a correlation between charge transfer via a single molecule and structural changes in molecular coupling to the electrodes, allows us to describe the low frequency $1/f^2$ noise of a single molecule. The obtained

results should be taken into account for development of molecular electronics including extremely important case of individual electrically addressed molecules.

4.3 Transition Voltage Spectroscopy (TVS) of Molecular Junctions

The study of electron transport through metal-molecule-metal junction has been an active area of research for more than a decade now. The underlying transport mechanisms are of fundamental importance for electronics applications and future device fabrication. Furthermore, biological charge transport is a central topic in science with high relevance for disease research and identifying origins of medical malfunctions.[102-104] Many advances have been made understanding the change of the charge transport mechanism from direct tunneling to hopping when the molecular length exceeds a certain value. However, possible changes of the transport pathway are still under controversial discussion and require clarification. Here, we take use of the transition voltage spectroscopy (TVS) to investigate the transport mechanism, which can help us to better understand the electron passport pathway at short distance.

4.3.1 Gap Size Dependent on TVS in Single Molecule Junction

Beebe *et al*. demonstrated that metal-molecule-metal junctions can exhibit current-voltage characteristics that correspond to a transition from direct tunneling to field emission as the applied bias exceeds a threshold voltage.[69] The voltage at which this transition occurs (transition voltage V_T) is linearly correlated with the energy offset between the metal Fermi level and the highest occupied molecular orbital (HOMO), a feature that allows probing of the effective energy barrier of charge transport by measuring V_T . The correlated transition voltage spectroscopy (TVS) has became a widely used method to measure relative barrier height in molecular junctions.[69,71,73,105]

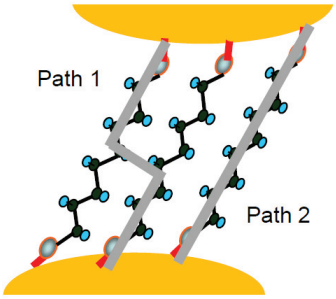

Figure 4.24: Two pathway: tunneling through chain to chain (path 1), tunneling through back bone of the molecule (path 2)

Later Lee *et al.* found that the transition point (V_T) is not fixed for a definite molecule.[34] Using AFM technology, they demonstrated that V_T shifts to lower voltages when the metal-molecules-metal junction is compressed. Lee attributed the shifting of V_T to the enhanced interaction between parallel molecules (intermolecular electron transport) as the sandwiched molecules within the self assembled monolayer (SAM) were compressed. However, the relation between intermolecular interaction and charge transport mechanism is still under debate.

In this chapter, the charge transport characteristics of single molecule junctions instead of molecule layer junctions were investigated to evaluate the influence of neighboring molecules on the charge transport mechanism. Although the interaction between parallel molecules was unavailable in the single molecular junction, the shifting of V_T was surprisingly observed as the molecular junction was compressed, which indicates that the gap size of the junction rather than the intermolecular interaction strongly affects the electron transport mechanism.

Single Molecule Junction

The target molecules octanedithiol (ODT), which contains two thiol termini as binding groups at both end, were integrated between the nanoelectrodes by a self assembly process to generate a metal/molecules/metal junction. For this purpose, 1 mM ethanolic solution of 1, 8-octanedithiol, a molecule, was prepared in a protective atmosphere where the oxygen level was less than 1

ppm. A 10 μL droplet of this solution was placed on the junction area under argon atmosphere. After a self-assembly period of five minutes on the gold surface of the electrodes, the sample was thoroughly rinsed with ethanol and dried in a nitrogen stream.

After calibration of the molecule free junction, 1,8-octanedithiol molecules were adsorbed and self-assembled on the gold wire from solution, dried and mounted into the MCBJ setup. The whole breaking process of the junction can be followed by monitoring the conductance of the molecular junction during the junction breaking process. From figure 4.25 one can observe the breaking process of the metal wire, which causes discreet conductance values of multiples of G_0. Further elongation of the junction results in a breaking of the gold-gold contact and a sharp drop of the conductance can be observed.

After breaking the metal wire, two separated nanoelectrodes are generated. Due to the two thiol termini of ODT, the molecule is able to bind covalently to both generated nanoelectrodes and a metal-molecule-metal junction is formed. The molecular junction finally transforms into a single molecule junction as the gap size increases further. The last plateau (lowest conductance value) of the breaking trace can be assigned to the single molecule conductance. More than 200 metal-molecule-metal junctions were analyzed and the histogram was drawn as shown in figure 4.25. From the histogram single molecules conductance determined statistically to $2.5\times10^{-4} G_0$, which is consistent with earlier reports.[106] In contrast, the typical plateaus at values below $1G_0$ are absent for molecule free junctions.

To establish single molecule junctions, we stopped the push rod right before the conductance reached the value of $2.5x10^{-4}$ G_0 and waited until a stable junction was formed. Under this conditions, the gap size effect on the transport properties of a single molecule junction was investigated.

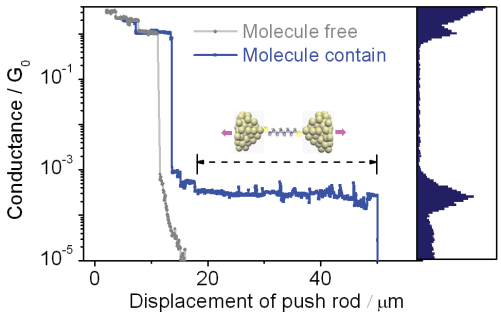

Figure 4.25: The conductance of a molecule free junction and a molecule containing junction as a function of push rod displacement. For the molecule containing junction, typical plateaus were observed after the breaking of the metal bridge, which indicates that a metal-molecules-metal junction was formed. For the molecule free junction, no pronounced plateau was observed at values below $1G_0$. The insert shows a stretched molecular junction before the finally rupture of the junction. The conductance histogram show a typical peak at $2.5\times10^{-4}G_0$

Gap Size Dependent on TVS in Single Molecule Junction

Three sets of *I*/*V* curves were acquired at varied gap size, Figure 4.26. Curves B, and curves C were obtain after the gap size was reduced by 0.2 nm and 0.4 nm respectively based on curves A (conductance plateau at $2.5\text{x}10^{-4}$ G_0). The process of decreasing the gap size from one set to the other was performed in ten sub-steps at a fixed bias voltage of 13mV. Only those data were further analysis where no sharp jumps or drops of the current were observed, indicating that no new bonds between molecule and electrode were formed or broken.

$ln(I/V^2)$ versus $1/V$ curves of three different gap sizes are shown in the insert of figure 4.26. At the initial gap size (red curve), the $ln(I/V^2)$ versus $1/V$ plot exhibit no significant voltage dependence. The curve reveals that only direct tunneling mechanism was present within the bias range between -1 V and 1 V. After the junction was compressed by approximately 0.2 nm, a transition from direct tunneling to field emission occurred at a transition voltage of 0.75 V. A additional decrease of the gap size by 0.2 nm lead to a shift of the transition point towards lower voltages, now 0.68 V. The insert picture explicitly demonstrates that the energy barrier of the junction decreases as the gap size decreases.

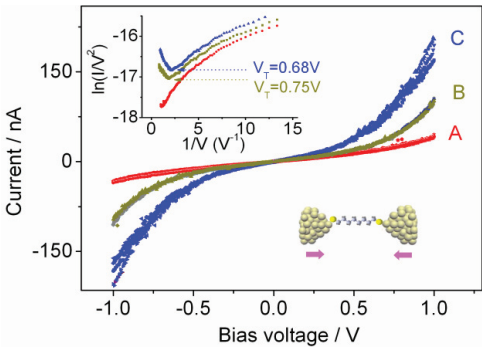

Fig. 4.26: *I*/*V* curves of single molecule junctions with three different gap sizes. Curves B and C were recorded after the gap size was decreased by approximately 0.2 and 0.4 nm based on curves A. The insert shows corresponding $\ln(I/V^2)$ versus $1/V$ characteristics. An inflection point can be observed, which shifts to lower biases as the gap size decrease. The cartoon display a single molecule junction during reducing the gap size.

In other words, field emission is enhanced as the gap size is reduced in the single molecule junction. It should be noted that intermolecular tunneling between parallel molecules was improbable since the junction was bridged by only a single molecule, and adjacent molecules were linked to only one of the two facing nanoelectrodes. Thus, an explanation that attributes the enhanced field emission only to changed transport pathways including intermolecular electron transport (chain-to-chain tunnelling in parallel molecules) seems to be inappropriate.

Direct tunneling from electrode to electrode without involving molecules has to be considered as well to explain the enhanced current at high bias for narrow electrode gaps. M. L. Trouwborst and co-workers demonstrated that V_T falls within a range between 1.4 V and 2.2 V if direct tunneling was dominate in Au–vacuum–Au junctions. In their publication it was shown that the *I*/*V* curves have an almost linear shape for biases below 1V and turn into S-shape at biases above V_T (higher 1.4V). However, in our case V_T shifts in a bias window between 0 V and ±1 V. Therefore, we believe that a contribution from direct tunneling between the electrodes is leading to a rather linear increase of the tunneling current within the investigated bias regime (0V to 1V) and cannot explain the observed strong nonlinear increase of the *I*/*V* curves for the molecule containing junctions, manifested in V_T below 1V.

4.3.2 TVS Independent on the Number of Bridged Molecules

In order to further evaluate the role of intermolecular charge transport, an additional experiment was performed where the number of trapped molecules was altered, but the final gap size was kept mainly unchanged. The experiments were performed in a way that we first established a stable junction. The junction conductance should be in the range of single molecule conductance (known from literature). At this stage, the position of the push rod was noted. Starting from this configuration we recorded *I*/*V* curves and altered afterwards the gap size by pushing the electrodes closer together (approximately by 6 Å to 10 Å). After releasing the junction to the original gap size, an additional *I*/*V* characteristics was recorded. This procedure was repeated until the junction collapses or jumps to contact ($G > 1G_0$).

During each approaching and withdrawing process there was a certain probability that either new bonds between molecules and electrodes were formed or existing bonds were broken. Therefore, it can be assumed that the two nanoelectrodes were bridged by different numbers of molecules after this procedure, although the final gap size was nearly the same. Finally, the *I*/*V* curves were analyzed. After analyzing the data one can estimate how many molecules were bridging the junction. The main assumption here is, that the *I*/*V* response with lowest conductance corresponds to a single molecule junction.

We found that 90% of the *I*/*V* characteristics fall into three distinct sets of curves. The three sets represent multiples of each other and can be deduced from the (fundamental) characteristics of a single molecule junction.

It can be assumed that each set of curves corresponds to nanoelectrodes bridged by 1, 2, or 3 molecules, respectively. The insert in figure 4.27 shows that no field emission was observed for all three sets of *I*/*V* characteristics within the bias window between -1V and +1V. A correlation between transition voltage and number of molecules in the junction was not found for this type of molecule.

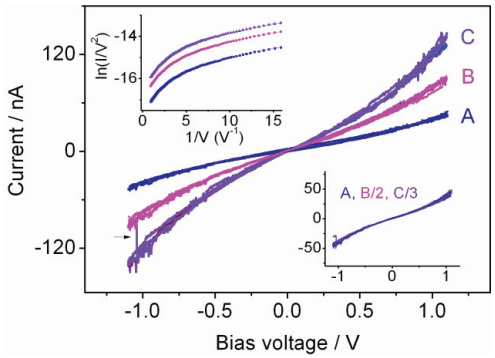

Figure 4.27: *I*/*V* curves of the molecular junction with varied number of trapped molecules at a fixed gap size. The measured *I*/*V* responses fall mainly into three sets of curves. The sets represent multiples (B=2, C=3) of the fundamental characteristics (A=1). The arrow indicates the change of number of trapped molecules in the junction. Top insert: no field emission was observed independent of the number of entrapped molecules. Bottom insert verifies that the *I*/*V* curves are multiples of each other.

This kind of experiments with a fixed gap size can be reproduced by several different samples (the same kind of molecules), however the actual *I*/*V* characteristics might deviate to some extent from sample to sample. Each sample has an unique arrangement of atoms and molecules, which leads to a certain variation of the tunneling response, however the $\ln(I/V^2)$ versus $1/V$ characteristics remains unaffected and no field emission was observed for all *I*/*V* characteristics.

Actually, the TVS behavior is dependent on the type of the investigated molecules. For instance, molecules containing phenyl groups allow pi-stacking and larger coupling between neighboring molecules which leads to higher probability of inter-molecules transport. In order to evaluate this assumption, an additional set of experiment has been performed including penyl group containing molecules (4,4' –thiobisbenzenethiol). Again the number of entrapped molecules was changed for a given gap size by approaching and withdrawing the nanoelectrodes. However, for this type of molecule the recorded *I*/*V* curves were not multiples of each other. Even more important, the transport mechanism changes as the number of entrapped molecules increases, as shown in figure 4.28.

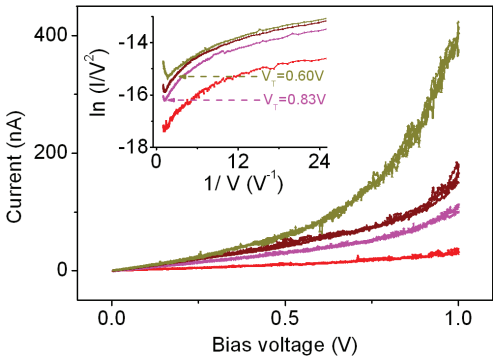

Figure.4.28: I/V curves of molecular junctions with varied number of entrapped 4,4' – thiobisbenzenethiol molecules at a defined gap size. Approximately 80% of the measured *I/V* responses fall into four sets of curves. The observed curves were not simple multiples of each other. The insert reveals that the transition voltage obviously depends on the number of entrapped molecules for this type of molecule.

These two observations indicate that π-stacking and stronger coupling exist between neighboring penyl groups. This finding is in agreement with observed intermolecular electron transport in metal-molecule-metal junctions reported by Wu *et. al*. Consequently, it can be concluded that the dependence of the transition voltage on the number of adjacent molecules in the junction has to be evaluated for each type of molecule separately. Nevertheless, with this work we clarified a misleading interpretation of experimental results recorded by conductive AFM (junctions with multiple molecules), and pointed out that single molecule junctions are required to distinguish between intra- and intermolecular electron transport.

For the explanation of the enhancement of field emission in single molecule junctions several aspects have to be considered if intermolecular transport can be neglected. At first, according to the full Simmons model, V_T will decrease as the tunneling distance decreases for narrow gaps, if one takes the image potential into account. However, the Simmons model is based on a rectangular barrier modified by an image potential, which does not in total take the particularities of molecules into account like molecule-electrode coupling (see below). Empirical models based on a coherent Landauer approach are in good agreement with V_T

characteristics at tunneling distances larger than 8 Å [33,69], but deviate for smaller gaps, see data reported here and Wang et al.[34]

Actually, the dependence of V_T on tunneling distance has been subject of theoretical and experimental investigations very recently, and seems to fall into different regimes. It was observed by Beebe et al. that V_T does not depend on the molecular length for different types of molecules which is in contradiction to the Simmons model excluding image potential. Later, Huisman et al. proposed a model (similar to Zotti et al.) which is based on a coherent Landauer approach which can explain that the transition voltage becomes length independent for gap sizes larger than 8Å. However, for smaller gap sizes the model predicts increasing V_T values. This prediction disagrees with the observations of Wang et al.[34] and the results presented here. Trouwborst et al. pointed out that Simmons model including image potential is providing a qualitatively correct description of $V_T(d)$ for molecule free junctions. The full Simmons model including image potential can also be used to describe the decrease of V_T with decreasing tunneling distance for molecule containing junctions at narrow gap sizes.

Furthermore, a possible explanation can be the increasing electric field for decreasing gap sizes. A change of the electrode distance by few Angstrom for sub nm gaps will result in an considerable alternation of the electric field strength in the junction, see figure 4.29. The geometry of the electrodes is assumed as a cone: bottom radius 5 nm, top radius 0.25 nm, height 9.5nm. The arrow length in the picture is proportional to the electrical field strength (V/m). The contour shows the value of electrical field on the electrode surface. The simulation was done by COMSOL and demonstrates that a few angstrom change of the gap size result a considerable alternation of the electrical field strength in the nanogap.

Density functional theory calculation also showed that increasing electric fields can alter the electronic structure of molecules and reduce their HOMO-LUMO gap.[107,108] Following this idea, one can assume that a decrease of the gap size leads to an enhancement of the electric field, resulting in a decrease of the tunneling barrier height. A smaller barrier height causes a shift of the transition voltage to lower bias voltages, which can be observed as an enhancement of field emission.

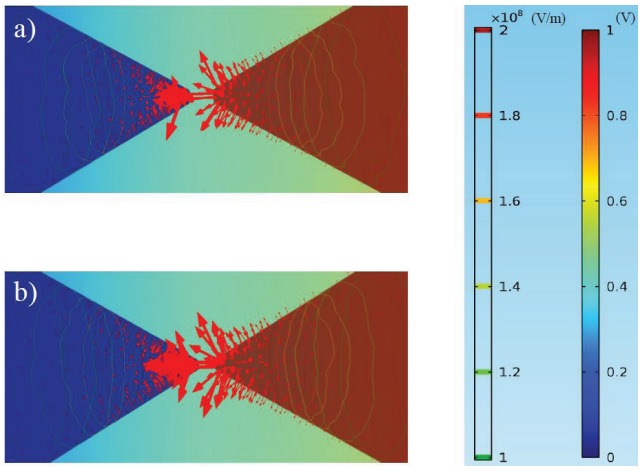

Figure 4.29: Simulation of the electrical field and potential distribution at two different gap sizes. a) 1.2 nm and b) 0.8 nm gap size between the two nanoelectrodes. 1 V voltage was applied to the right nanoelectrodes of a) and b) and the conjugated electrodes were connected to ground.

Another factor that should be considered is the junction distortion caused by their mechanical compression. When the gap size between the two nanoelectrodes is reduced, the sandwiched molecule in the junction experiences a certain compression force. The compression force will change the metal-molecule contact, which will affect the electronic structure of the junction, including the spatial distribution of the frontier orbits, the HOMO-LUMO gap, and transmission function.[35,109] This reconfiguration of the electronic structure can affect the electron transport characteristics and contribute to the enhanced field emission.

4.4 Molecular Junction Based on Metal Ion Bonding

In the past decade, not only the investigation of transport processes across a single molecule became feasible, also transport of charges between molecules via few or single transport channels has been reported. However, only little is known about electron transport via metal ions entrapped between ligand molecules, although metal ions play a crucial role for instance in biological charge transport. For metal complexes, it can be envisioned that the charge transport depends on nature of ligands and on the kind of metal ion entrapped between the ligands. Therefore, it is of fundamental interest to investigate if and how metal ions are influencing electron transport on the level of individual molecules.

4.4.1 Molecular Junctions Bridged by Metal Ion Complexes

In this chapter, metal-molecule-ion-molecule-metal junctions on the single molecule level were realized by mechanically controllable break junction experiments. Although the junction of metal complexes had been investigated by Tao *et al,* the molecule junction bridged by a metal ion had never been reported so far. In previous works on metal complexes, commonly several parallel electron pathways via ligand molecules and metal ion were presented.[110,111] Here, the metal-molecule-ion-molecule-metal junctions, in which all the current pass through the metal ion was realized for the first time. Within this chapter, we investigated the influence of different metal ion on conductivity, while leaving the ligands mainly unchanged.

For this purpose, we used 3,3'-dithiobis[N -(5-amino-5-carboxypentyl)propionamide-N',N' – diacetic acid] dihydrochloride, abbreviated as dithiobis (C_2-NTA), a simple aminooligocarboxylic acid, which can be used as general sequestering agent for many metal ions. Nitrilotriacetic acid (NTA) became already decades ago a mass product as softener for water and is more recently used for the purification of proteins due to its ability to form stable metal complexes with recombinant histidine tags. The superior ligand properties of NTA arise from their selective N donor and the presents of three general O donors which can form, by coordination, stable complexes with most metal ions. Here, we used this ability to form metal-molecule junctions that are bridged by different metal ions in order to investigate their influence on conductivity of the junction.

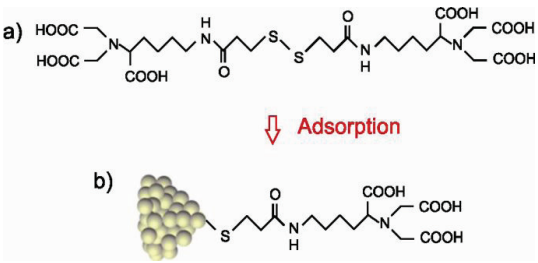

Figure 4.30: a) Molecule structure of 3,3' dithiobis [N-(5-amino-5-carboxypentyl propionamide) -N-N-diacetic acid] dihydrochloride, dithiobis (C_2-NTA), and b) surface tethered 3 thio N -(5-amino-5-carboxypentyl) propionamide-N',N' -diacetic acid molecule.

3,3'-Dithiobis[N -(5-amino-5-carboxypentyl)propionamide-N',N' –diacetic acid] dihydrochloride (Dithiobis (C_2-NTA)) was purchased from DOJINDO (Japan). During adsorption at the gold surface, the disulfide bond cleaves and Au-S bonds are formed at the metal-molecule interface as shown in figure 4.30. The carboxylic/amine groups at other terminus can bind either to metal ions or the gold surface of the opposing electrode.

The high precision of gap size tuning and the high mechanical stability of MCBJ were used to investigated metal-molecule-metal junctions that were bridged by the individual metal complex molecules. At first, the opening traces of bare gold wire were recorded, which was used as a reference system. The electrical conductance as a function of push rod movement during opening cycles is presented in figure 4.31(I). At the beginning of the breaking process, the gold wire shows ohmic dependence of the conductance on the wire diameter, until a discrete conductance values can be observed. The resulting plateaus at multiples of G_0 (due to atomic point-point contacts) pass into a sharp conductance drop after further elongation of the junction. This drop is caused by a sudden retraction of the Au atoms during the breaking process of the gold wire.[67] Finally, the traces develop into exponential decays of the conductance as function of electrode distance without any plateau of statistical weight.

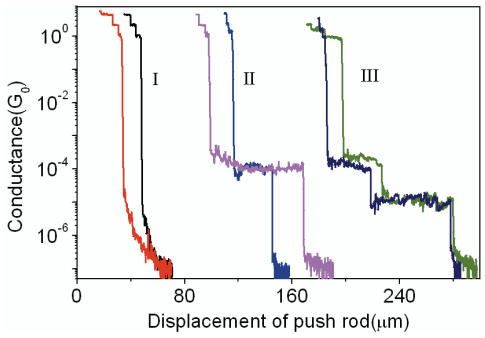

Figure 4.31: Conductance change as a function of push rod displacement. Three kinds of representative curves are shown: I) Breaking of a bare gold wire, no reproducible plateaus are observed after breaking the wire. II) Breaking of junctions modified by C2-NTA, typical plateaus are observed. III) Breaking of molecular junctions modified by C2-NTA and Ca^{2+} ions, two sets of plateaus are observed.

The picture changes, when the molecule of interest dithiobis (C_2-NTA) is applied to the junction. Within a self assembling process the molecules bind covalently to the gold electrode by cleaving the disulfide bridge and formation of Au-thiolate bonds. Breaking a metal junction modified by dithiobis (C_2-NTA) revealed the same plateaus at G_0 and the sharp conductance drop right when the break occurs. However, now additional clear plateaus near $1.1*10^{-4}$ G_0 appear as shown in figure 4.31(II). At these plateaus, the conductance was almost insensitive to changes of the electrode distance, which indicates that metal-molecule-metal junctions were present. Similar plateaus were observed for different types of molecules including molecules with thiol and carboxylic terminal groups.[110] It seems reasonable to assume that molecular bridges were formed with thiolate-Au bond at one terminus and carboxylic bond at the other. The actual conductance value of a certain metal-molecule-metal junction depends on their electronic properties (β value) and the contact resistance between molecule and electrode. The conductance observed for this molecules falls within the range of values reported for other short chain molecules.[110]

After the NTA containing junctions were characterized, metal ions were added. Additionally to the plateau located near $1.1*10^{-4}$ G_0, new stable junction configurations were observed at lower conductance. A representative opening trace is shown in figure 4.31 (III) for the addition of Ca^{2+}

ions. The recorded conductance of the second plateau is one order of amplitude smaller than the conductance of the first plateau. The two plateaus indicate that both metal-molecule-metal junction and metal-molecule-ion-molecule-metal junction can be obtained during the breaking process. After analyzing 500 individual traces of 5 different samples we observed in 60 % of all cases that both plateaus coexist.

When metal ions were introduced to the NTA modified metal junction, the N donor and the three O donors of the $–COO^-$ groups have the ability to form, by coordination, stable complexes with the metal ions (as depicted in figure 4.32). Moreover, all employed metal ions facilitate the formation of Me-$(NTA)_2$ complexes where two NTA molecules are tethered to one metal ion. The formation of bivalent complexes is a prerequisite to establish metal-molecule-ion-molecule-metal junctions when the nanoelectrodes were separated apart.

Charge transport characteristics of Ca^{2+} containing molecule junctions were shown in figure 4.33. Representative I/V curves recorded at the first conductance plateau (conductance $1.1*10^{-4}$ G_0, corresponding to metal-molecule-metal junctions) are shown in figure 4.33 a). At this initial state of the I/V-measurements, the junction was stable. The insert picture shows the $ln(I/V^2)$ versus $1/V$ plot corresponding to the I (V) curves at negative bias. The inflection point (transition voltage V_T), which is related to the effective barrier height, was found at 0.8V) I (V) curves recorded at the second conductance plateau (conductance $1.2*10^{-5}$ G_0, corresponding to metal-molecule-Ca^{2+}-molecule-metal junctions) are shown in figure 4.33 b). The $ln(I/V^2)$ versus $1/V$ presentation reveals a lower transition voltage V_T than in a), which can be attributed to a decreased tunneling barrier for ion containing junctions.

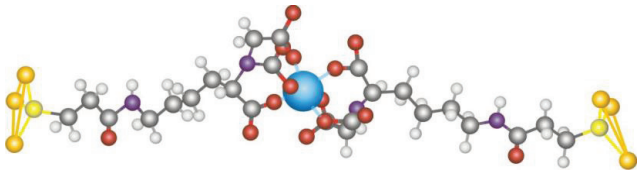

Figure 4.32: Schematic of metal-molecule-ion-molecule-metal junction based on ion coupling. Three O donors of the $–COO^-$ groups couple with metal ion and form stable complexes.

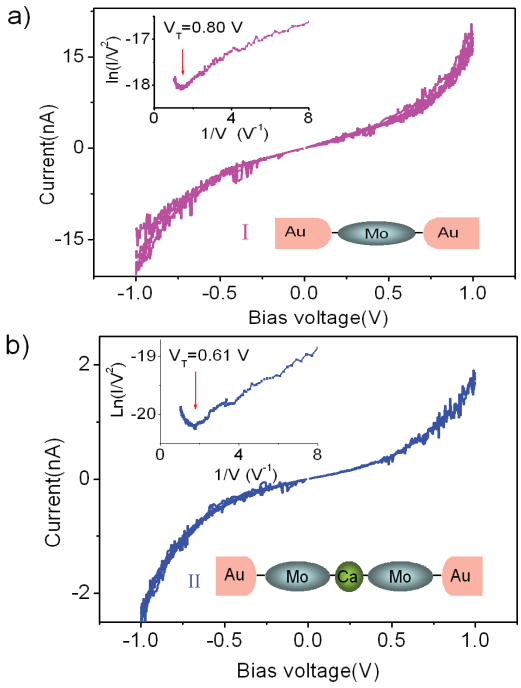

Figure 4.33: Charge transport characteristics of Ca^{2+} containing molecule junctions. a) Representative *I*/*V* curves recorded at the first conductance plateau (conductance $1.1*10^{-4}$ G_0, The insert picture shows the $ln(I/V^2)$ versus $1/V$ plot corresponding to the I (V) curves at negative bias. b) I (V) curves recorded at the second conductance plateau (conductance $1.2*10^{-5}$ G_0, corresponding to metal-molecule-Ca^{2+}-molecule-metal junctions).

The *I*/*V* responses exhibited a certain but not very pronounced asymmetry. Therefore, we conclude that the conductance is mainly determined by the transport through the molecule. Furthermore, it can be reasoned that the relatively symmetric shape might be due to the high number of available transport pathways for molecules with three carboxyl groups. The additional transport channels and the high flexibility of these molecules to adapt to optimal transport configurations may compensate the asymmetry in the *I*/*V* curves which is expected from the stronger thiol-gold coupling than the –COOH-gold coupling.

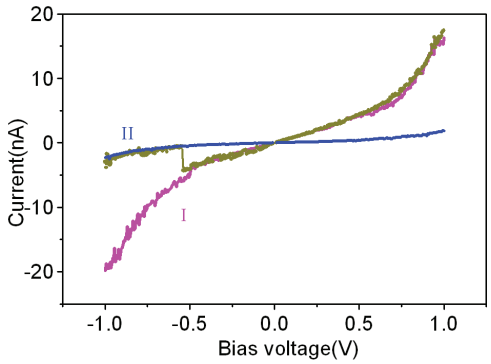

Figure 4.34: Transitions from a) to b) in figure 4.22 were occasionally observed, indicating metal-molecule-Ca^{2+}-molecule-metal junction exist after the breaking of metal-molecule-metal junction.

I/*V*-measurements presented in a) and b) were recorded at the same junction distance. However transitions from a) to b) was occasionally observed, as shown in figure 4.34 indicating two kind of the junction coexist.

4.4.2 Junctions Conductance Dependent on the Metal Ion

To determine the conductance of the junctions containing different metal ions, corresponding conductance histograms were calculated, figure 4.35. Each histogram was extracted from at least five different samples. Only the opening traces were used for data analysis. In the histograms of all investigated samples a peak at $1G_0$ can be found that originates from the breaking process of the metal wire. Figure 4.35a) shows the conductance histogram obtained from those samples where only C_2-NTA (ion free) was presented in the junction. Just one obvious peak (p_0^1) was observed at the histogram after breaking the metal wire.

In contrast, when metal ions were added to the junction (Ca^{2+} for figure b, Zn^{2+} for figure c, Ni^{2+} for figure d), each histogram displayed two obvious peaks. It is interesting to note that one set of peaks (p_0^1, p_0^2, p_0^3, p_0^4) was located almost at the same position in each histogram, indicating metal-molecule-metal junctions were frequently formed also when metal ions are present.

Furthermore, a second set of peaks (P_A, P_B, P_C) at low conductance values can be observed in the histogram. However, the position of these peaks is not constant but shifts depending on the kind of the metal ion. The displacement of the P_A, P_B, P_C indicates that these peaks are associated to the various metal ions and that metal-molecule-ion-molecule-metal junction were formed. It furthermore suggests that the ion has a significant influence on the conductance of the junction.

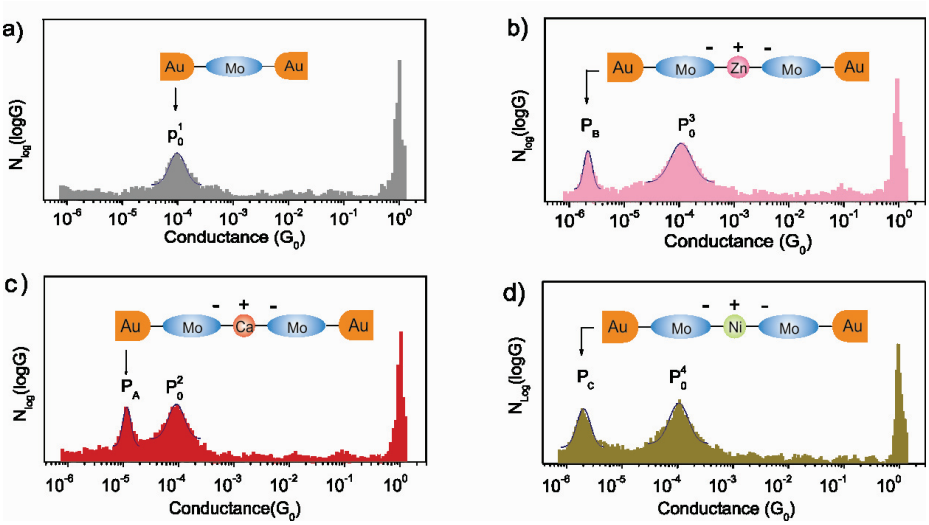

Figure 4.35: Log-histograms of measured conductance values obtained from four hundred successive opening cycles after: a) dithiobis (C_2-NTA) was applied to the junction. Here, only one peak can be clearly observed. b-d) Molecules bridged by Ca^{2+},Zn^{2+},Ni^{2+}, respectively. An additional peak is present. The peaks P_0^1, P_0^2, P_0^3 and P_0^4 are located at same position and can be assigned to the conductance of metal-molecule-metal junctions. The additional peaks of P_A, P_B, P_C are located at different positions indicating that metal-molecular-ion-molecule-metal junctions were formed. The black curves in the histograms are representing Gaussian-peak fits.

The conductance of the Ca^{2+} ion containing complex is significantly smaller than that of the bare C_2-NTA junction. This observation is reasonable since it can be assumed that the charge transport distance is increased for the complex. However, P_A is approximately one order of magnitude large than P_C although the junction length should be similar. Obviously, the metal ions alter the conductance specifically in the order of: $Ca^{2+} >> Zn^{2+} > Ni^{2+}$. Since all complexes are formed from the same ligands, one can assume that the conductance differences originate from the specific electron configuration of the different coordination complexes, which is in this case mainly defined by the nature of the metal ion.

The electron configuration of metal complexes is commonly exemplified by ligand field theory[a] . This theory describes the arrangement of ligands in space with respect to the orbitals of the metal ion and provides information about complex stability. The stability increases as a function of energy gap between bonding and antibonding orbitales and the occupation of these orbitals with electrons.

In the present case, we are considering three different complexes that are composed of one metal ion (all from the same period) with two positive charges and two C_2-NTA sequestering molecules. If we assume that the ligands are similarly arranged around the metal ion and the corresponding orbital symmetry sustains when the central metal ion is exchanged than one can consider the different metal complexes as isoelectronic complexes. A typical feature of isoelectronic complexes is that their energy gap between HOMO and LUMO (HOMO: highest occupied molecular orbital; LUMO: lowest unoccupied molecular orbital) depends on the atomic number of the central metal atom. With the increase of the atomic number and the positive charge of the metal ion, the energy gap increases. The increased energy gap also leads to an enhanced complex stability.[82] In terms of electron transport, the alignment of HOMO and LUMO with respect to the Fermi energy of the metal electrodes strongly influences the height of the tunneling barrier and therefore the transport of charges through the molecule. For stable metal complexes with large HOMO–LUMO gap, it is likely that they have a large tunneling barrier and show poor conductivity.

[a] H. L. Schläfer, G. Gliemann, *Basic Principles of Ligand Field Theory* Wiley Interscience, New York, **1969**, p. 15-45

This consideration can be applied to the results presented here. Ca-(C_2-NTA)$_2$ showed the highest conductivity among the investigated metal complexes, however its stability, represented by the complex constant, is the smallest. Table 4.2 summarizes the observed positions of the conductance peaks and complex constants (K_1) reported previously. The junction conductance of the Ca^{2+} containing complex is approximately one order of magnitude larger than those of Ni^{2+} and Zn^{2+} complexes. K_1 of Ni-(C_2-NTA)$_2$ and Zn-(C_2-NTA)$_2$ are similar and also the conductance does not differ much. At the same time their complex constant is 4 to 5 orders of magnitude larger than that of the Ca^{2+} complex.

Table 4.2: Type of junction, corresponding complexes constant, and assigned conductance values are shown in the table.

	Junction type[a]	Complexes constants [b]	Junction Conductance/G_0
1	Au-Mo-Au	No	$(1.1\pm0.5)\times10^{-4}$
2	Au-Mo-Ca^{2+}-Mo-Au	6.45	$(1.2\pm0.2)\times10^{-5}$
3	Au-Mo-Zn^{2+}-Mo-Au	10.66	$(2.3\pm0.2)\times10^{-6}$
4	Au-Mo-Ni^{2+}-Mo-Au	11.54	$(1.9\pm0.4)\times10^{-6}$

[a] Mo represents 3 thio N -(5-amino-5-carboxypentyl) propionamide-N',N' -diacetic acid. [b] Stability constants of NTA complexes (log K_1) were taken from Reference.[112]

All three metal ions are able to form metal complexes involving two nitrilotriacetic acid molecules.[112-114] However, since each of these molecules carries 4 possible ligand groups and each metal ion requires only 6 of them to form a stable complex it can not be excluded that one nitrilotriacetic acid molecules coordinates to two metal ions.[115] In the same manner it is possible that one metal ion forms bonds to more than two C_2-NTA molecules. It can be assumed that the molecules are densely packed at the electrode and the surface tethered nature of the ligand molecules may lead to adsorbate configurations that would not be thermodynamically preferred in bulk solution.[116] Therefore, it is reasonable to consider the observed conductance peaks as average over different bonding configurations and different transport channels. The data,

presented here, clearly demonstrate that the metal ion strong influence the conductance of the molecule junction as well as the properties of charge transport.

4.3.3 Calculation Based on Density Functional Theory

To better understand the electronic structure of the metal complex, density functional theory (DFT) calculations were performed with the dmol^3 simulation package, in which the local density approximation (LDA) with PWC (Perdew-Wang approaches for the correlation functional) was used.[117]

Here, the software of Material studio 5.0 (from the company of Accelrys) was used for the DFT calculation. Geometry optimization determines the minimum-energy structure of a molecule, starting from the initial geometry entered. After the geometry is minimized, any other requested properties are computed.

The structure optimization of Au-molecule-ion-molecule-Au system was performed by minimizing the total energy. The default convergence criteria of DMol^3 was applied, i.e., $2.0\times10^{-5}eV$ for the energy change per atom, 0.005 nm for the root-mean-square atomic displacement and 0.005 eV/nm for the root-mean-square residual force on movable atoms. Please note that $Ha\approx27.3\times ev$. The structure optimization process of Au-molecule-Ni^{2+}-molecule-Au system was shown in figure 4.36. The optimization process was also applied to Ca^{2+} and Zn^{2+}containing junctions.

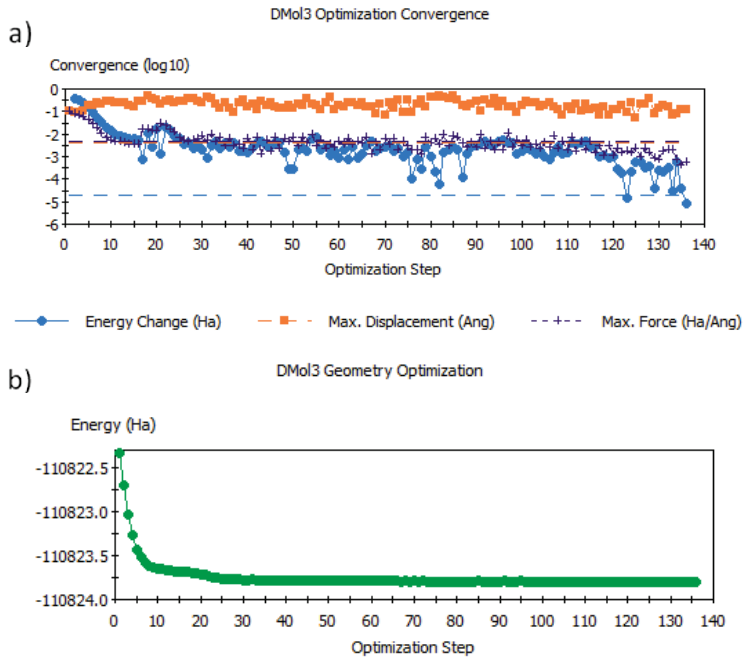

Figure 4.36: Structure optimization of Au-molecule-Ni^{2+}-molecule-Au junction. a) the energy change, maximum displacement and maximum force as a function of the optimization steps. b) the total energy of the junction as a function of the optimization step.

After structure optimization, the geometry of the molecule as well as the bond length between the sulfur and gold were changed. For the Au-molecule- Ni^{2+}-molecule-Au junction, the S-Au bond was calculated to be calculation 0.167 nm and the Ni-O bond length was calculated to be 0.1.87 nm. For Ca^{2+} containing junction and Zn^{2+} containing junction the Ca-O bond is calculated to be 0.185 nm and Zn-O bond was calculated to be 0.193 nm.

After the geometry is successfully minimized, the total electron density and wave function intensity of the HOMO and LUMO were calculated. At last the energy gap between the Femi level and the nearest molecular orbital of three different molecule junctions were estimated.

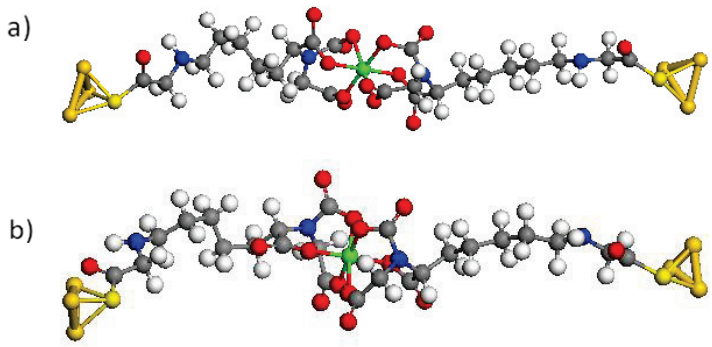

Figure 4.37: The structure of Ni^{2+} contain junction before a) and b)after geometry optimization.

Total electron density isosurfaces, which describe the surface of an molecule for a defined electron density, in the Ni^{2+} contain junction is shown in figure 4.38. In this plot, the isovalue of 0.95 was choosen for isosurface. The electron density isosurfaces demonstrate that molecular orbital are spread over the contact region indicating a strong interaction with the electrodes. The electron density around the center metal ion is almost independent of other atoms indicating the metal ion play important role in the electron transport. There is no obviously difference between three kinds of junctions, therefore only Ni^{2+} contain junction is presented.

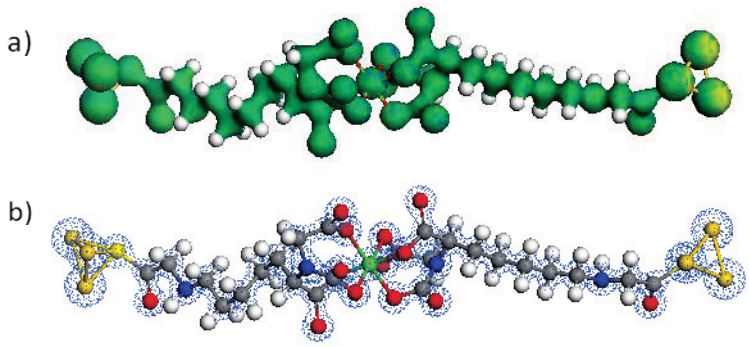

Figure 4.38:. Total electron density isosurfaces of the Ni^{2+} containing junction, a) shown as solid surface, b) shown in dots style.

Wave function intensity of the HOMO and LUMO are shown in figure 4.39. Blue indicates regions with positive and yellow with negative wavefunction amplitude. The graphic demonstrate that the value of wave function intensity is high around the center Ni^{2+} ion for LUMO. In contrast, wave function intensity is low in HOMO. The high wavefunction identity of LUMO indicates that the metal ion strongly affects the molecule orbital.

The *ab initio* calculation shows that the nearest molecule orbital to the Femi level is the HOMO for all the three type of junction. The Ca^{2+} containing junction has the smallest energy gap. In contrast the Ni^{2+} contain junction has the biggest energy gap. Since bigger energy gap will result in the smaller conductance, the calculated data indicated that the conductance order should be: Ca^{2+} containing junction > Zn^{2+} containing junction > Ni^{2+} containing junction. The order of the energy gaps obtained *by ab initio* calculated is qualitatively agrees with the experimental data.

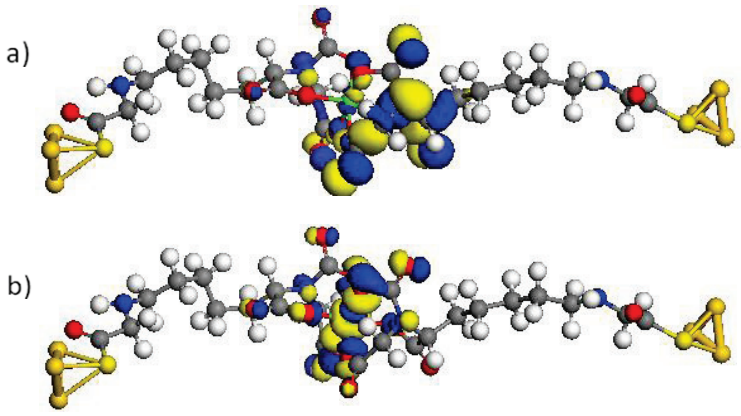

Figure.39: Wave function intensity of the a) HOMO and b) LUMO in the Ni^{2+} contain junctions.

Table 4.3: Energy level of HOMO and LUMO in three types of junctions

Molecular Junctions	E_F (ev)	HOMO (ev)	LUMO (ev)	Energy gap(ev)
Ca^{2+} contain	-5.157	-5.361	-4.511	0.204
Zn^{2+} contain	-4.922	-5.157	-4.250	0.235
Ni^{2+} contain	-4.940	-5.189	-4.693	0.259

Since in employed molecule also take gold atoms as electrode contacts into account, a Femi level could be derived for all investigated systems. Based on the obtained Femi level the energy gap could be calculated. However the energy gap shown in table 4.3 seems to be underestimated in comparison with experimental data. For a better agreement, more gold atoms should be taken into account.

Chapter 5

Summary and Outlook

Charge transport at the single molecule level was investigated in the scope of this work by means mechanically controllable break junction experiments with high stability. We concentrate ont the aspects that are important for electrical characterization of bioelectronics junctions. These aspects are the noise characterization of the molecular junction, the features of electron transport across model molecules in narrow electrode gaps, and the influence of the metal ion on the electrical properties of metal complexes.

Noise Characterization of Molecular Junctions

We measured and compared the electronic noise of molecule-free and single-molecule-containing mechanically controllable break junctions. Both junctions revealed typical $1/f$ noise characteristics. An additional $1/f^2$ noise component was clearly observed only in metal/molecule/metal junctions, when a single molecule bridged the nanoelectrodes. Results of noise spectra studies of different molecules demonstrate that the characteristic frequency of the $1/f^2$ noise component is independent of molecule's bonding strength to the electrode and correlates with the lock-in current amplitudes.

We also analyzed the character of the time-dependent voltage fluctuations. The registered $1/f^2$ electric noise component, relevant to a single bridging molecule, is interpreted as the manifestation of a dynamic reconfiguration of molecular coupling to the metal electrodes. The changes occur without complete bond breaking and involve near configuration states with very similar electric properties. Using the fact of existence of strongly distinct characteristic times in the system, we developed a phenomenological model that couples the charge transfer via a single

molecule with its reconfiguration and describe the $1/f^2$ noise of a single molecule. The $1/f^2$ noise component found can be used to quantitatively study properties of individual electrically addressed molecules.

Gap Size Dependent Transition From Direct Tunneling to Field Emission

Although the transport between parallel molecules was unprobable in the single molecular junction, surprisingly, a shifting of V_T was observed as the molecular junction was compressed. I/V measurements with different numbers of molecules in the junction at a given gap size revealed that intermolecular electron transport between adjacent molecules was of minor importance and alkanedithiols molecules can be considered as individual transport channels. The presented observations lead to the conclusion that the distance change between the electrodes and associated alternations of the molecular electronic structure rather than inter-molecular tunneling result in the enhancement of field emission for alkanedithiols.

Molecular Junctions Bridged by Metal Ion Complexes

We have demonstrated that surface tethered nitrilotriacetic acid molecules can form stable metal-molecule-ion-molecule-metal junction with different metal ions. The electrical conductance of molecular junctions with various metal ions was investigated. A statistical analysis of the recorded conductance traces revealed that the coupling efficiency between the ion and ligand groups depends strongly on the type of the coupling ion with the order: $Ca^{2+}>>Zn^{2+}>Ni^{2+}$. The conductance was found to be inversely dependent on the complex stability.

Based on DFT calculation, the wave function density of the HOMO and LUMO were obtained. The order of the energy gap obtained by *ab initio* calculation perfectly agrees with the experimental data, in which Ca^{2+} containing junction have the smallest energy gap followed by Zn^{2+} complexes, and Ni^{2+} compounds with the largest band gap. The observed relation between type of metal ion and conductivity of molecular junctions may help to elucidate the biological charge transport characteristics and pave the way for novel strategies to design molecular based devices.

Although MCBJ method can not obtain the image of the sample surface as scanning probe methods, the mechanically controllable break junction show powerful ability to investigate the properties of single molecule in the aspects of noise characterization, conductance, and electron transport. For a further investigation, several aspects should be taken into account.

First of all, the device can be modified to be more powerful. For instance, a gate electrode can be added beside the source-drain electrodes. Such a three-terminal device can not only adjust the number of trapped molecules, but also can directly modulate the transport current through the molecule. In this way, the single molecule field effect transistor can be obtained.

Second, although we have demonstrated that intermolecular electron transport between adjacent molecules was of minor importance for alkanedithiols molecules, and such kind of molecules can be considered as individual transport channels, other kind of molecules, for instance, those containing phenyl groups which allow pi-stacking and larger coupling between neighboring molecules, have to be evaluated.

This thesis is only the first step to investigate the electron transport from model molecules to bio-molecules. The investigation of electron transport in biological systems (such as peptides, and proteins) will be more challenging. For example, some types of peptide have many binding sites along the molecule's backbone, and the corresponding complicated bonding configuration makes it hard to determine the conductance of the peptide. Furthermore, many bio-molecules can only

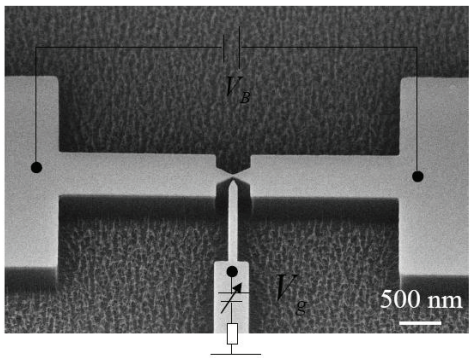

Figure 5.1: Single molecular field effect transistor (type II with a side gate)

be investigated *in situ.* The realization of *in situ* break junction experiments requires large endeavors to isolate the electrode leads on a flexible substrate, to attach a deformable cell above the chip, to precisely control the potential at the nanoelectrodes, and to link the asymmetric biomolecules reproducibly into nanogap. This work will be addressed in the future.

Appendix A

Additional Images

Electromigration Break the Junction

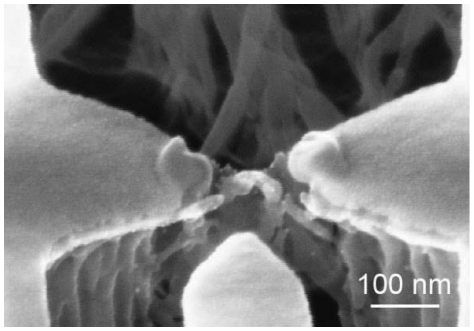

Figure A.1: A nano gap was shown when a voltage above 1 V was applied to the gold wire. The constriction (40nm×40 nm) fabricated by e-beam lithography can be easily broken down by the applied voltage. Strong electron migration cause the melting of the. Please note, even the static electric force carried by the human body was high enough to destroy the constriction. Therefore one must make sure that the chip and MCBJ set up is carefully connected to the ground and discharged before the electrical measurement.

Surface Image

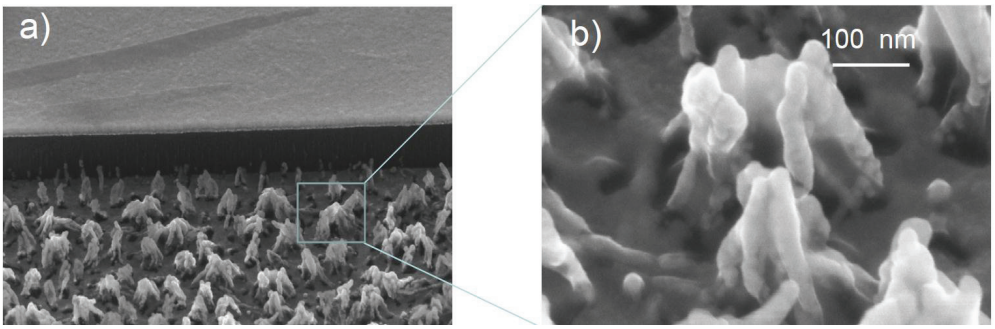

Figure A.2: SEM picture of the junction area. A grass shape was formed after etching the polyimide with CHF_3 and O_2. The SEM picture was taken after sputtering 2 nm Ti on the chip everywhere in order to obtain high resolution picture.

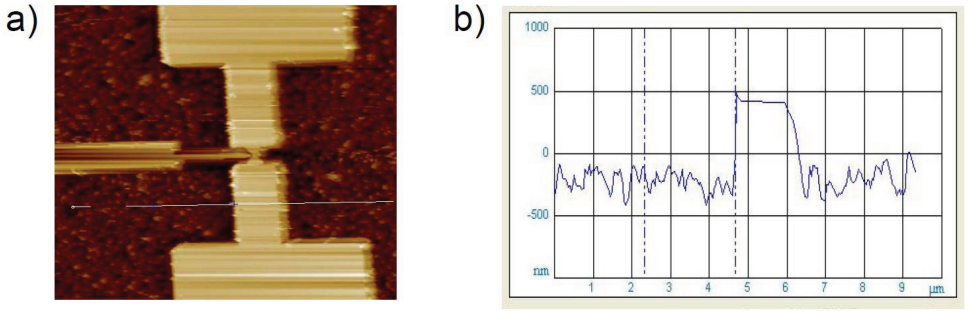

Figure A.3: The AFM picture of the junction area shows that the polyimide surface is not smooth, and the height of the electrode above the isolating layer (the same as etching depth) is about 700 nm. The profile of b) was obtained along the direction presented in a with white line.

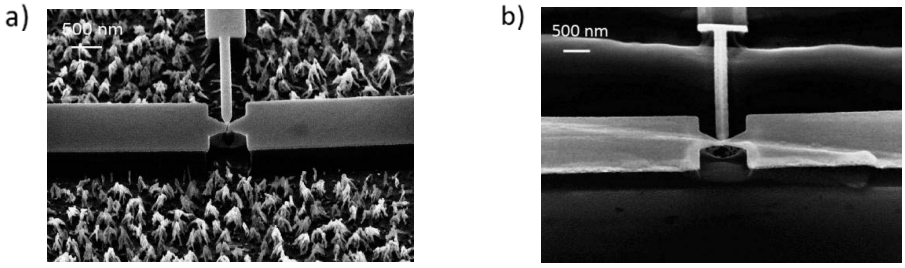

Figure A.4: In order to obtain a smooth surface, a)Si_3N_4 was used in stead of polyimide b). Tthe isolating layer (Si_3N_4) was etched in such condition: gas mixture 15CF_4 / 30 O_2, power 75 w, DC bias 319 V, gas pressure 150 mTor, etching time 10 minutes.

Calcium Binding to Oligopepties

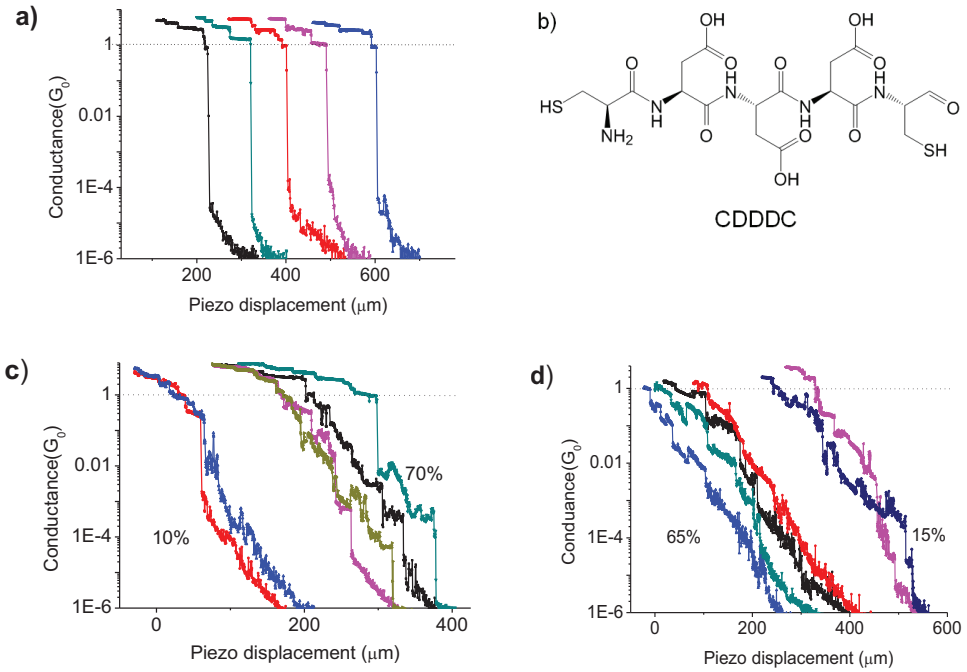

Figure A.5: Peptide containing break junction. a) The braking of bare gold wire as a reference system. b) Structure of the peptide with sequence 3D'. c) The breaking of a junction modified by self-assembled '3D' on the electrode surface. Because of the complicated bonding configuration, two types of curves were observed: 'almost continuously decreasing curves' and 'stepped curves'. The ratio between the two types of curves changed after the Ca^{2+} ions were introduced to the junction, see d). The change in ratio was attributed to the conformational changes induced by Ca^{2+} binding to the molecule.

Experiments Combined SERS and MCBJ

One major problem of MCBJ is that one is using mainly electrical measurements to characterize the junctions. SERS is the rare methods that provide spectroscopic information of the molecular junctions.

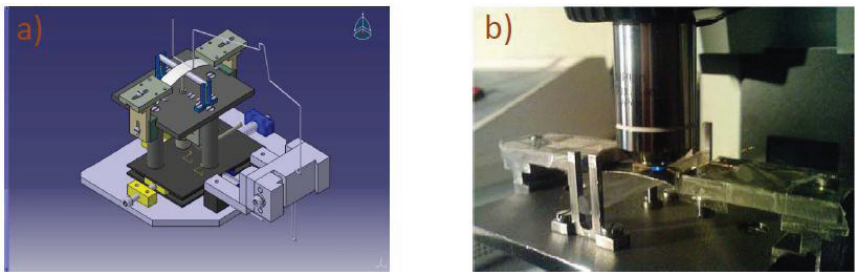

Figure 3.6: a) Schematic drawing of the experimental setup of combined Raman spectrometer and mechanical controllable break junction. b) The setup of Raman spectrometer combined with MCBJ. A laser beam focused on the junction area can be seen.

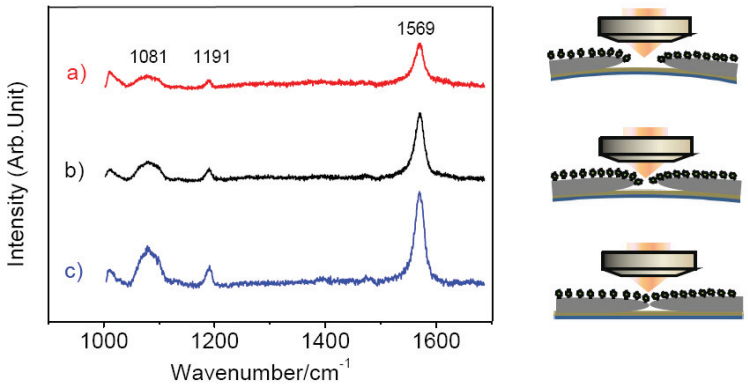

Figure A.7: a) Raman spectroscopy of 1,4-benzendithiol in the junction area during the process of bending the chip. The gap size between the two nanoelectrode is approximately a) 3nm, b) 0.6nm, c) 0.3 nm respectively. Laser: 488nm.

Table 4.3: Raman spectral data and vibrational assignment of Benzenedithiol on silver electrode surface

SERS	Vibrational assignments
1593 sh or vs	Benzene ring vibration[118-120]
1566/1570 vs or m	8a(Ag)-in plane benzene ring vibration[118-120]
1186 ms	9a(Ag)-in plane benzene ring vibration[118-120]
1076 s	ν (CS,CC) involving Ag symmetry[121]
833 m	CH deformation mode[118-120]
819 m	17b(B_{3u}) out of plane CH deformation mode[118-120]
749 w	7a(Ag) in plane CH deformation mode[118-120]
738 w	in plane CH deformation mode[118-120]
491 w	16b(B_{3u}) v(CS)[118-122]
357 m	ν (Ag-S)[123-125]

Abbreviations used: v, very; s, strong; m, moderate; w, weak; br, broad; sh, shoulder

The SH stretching and the CSH bending bands are completely absent in the SERS spectrum. This implies that BDT adsorbs on the silver surface as dithiolate after losing both of its thiol protons. With the two sulfur atoms being coordinated to the silver surface, the benzene ring of adsorbed BDT will assume a flat stance with respect to the silver surface. Since the bandwidths of the benzene ring modes such as 8a and 9a appearing at 1566 cm-1 and 11186cm-1, respectively were broader a direct surface-ring-orbital interaction[118,120] might also be involved in the surface adsorption of BDT on Ag. The absence of the free SH stretching vibrational modes (~915 cm-1, ~2560 cm-1)[122] suggest that the benzenedithiol adsorbs to the Ag surface via two S-Ag linkages.[123-125]

Appendix B

Pattern Design

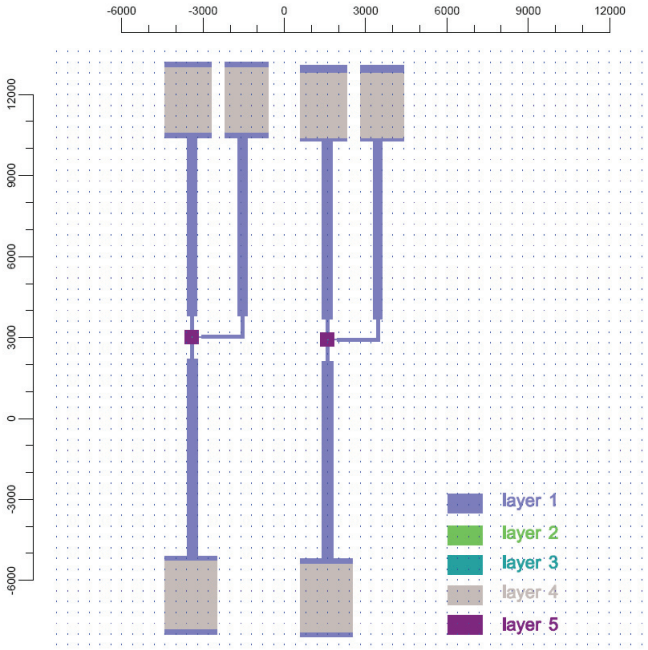

Figure A.5: A pattern design by the Clewin 4.0. The layer design facilitates the e-beam writing process. Layer 1 and layer 2 were design for the first e-beam writing (layer 1 is designed for coarse structure, layer 2 is designed for fine structure). Layer 3, layer 4 and layer 5 were design for the second time e-beam writing (layer 3 produced a circle, layer 4 uncovered electrodes for the out side bonding, and layer 5 provided a mark for the alignment).

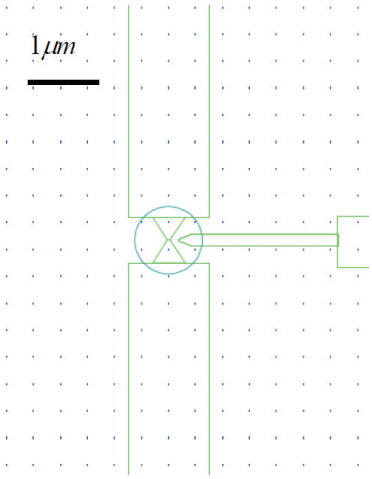

Figure A.6: A close look of the Pattern designed (layer 2 and layer 3). A third electrode was design beside the gold wire.

Appendix C

I-V Curves Fitting program

We tried to find the energy barrier of 11-mercaptoundecanoicacid (MUA) by fitting the I-V curve using the Simmons equation according to Wang's method.[126] The Simmons equation is as follows:

$$I = \frac{Ae}{4\pi^2 \hbar d^2}\left\{(\phi_B - \frac{eV}{2}) * \exp\left[-\frac{2(2m)^{\frac{1}{2}}}{\hbar}\alpha(\phi_B - \frac{eV}{2})^{\frac{1}{2}} d\right] - (\phi_B + \frac{eV}{2}) * \exp\left[-\frac{-2(2m)^{\frac{1}{2}}}{\hbar}\alpha(\phi_B + \frac{eV}{2})^{\frac{1}{2}} d\right]\right\}$$

Here , A is the cross section which pass the current. d is the gap size, m is the electron effective mass, ϕ_B is the barrier height, and V is the applied bias. For molecular systems, the Simmons model has been modified with a parameter α. α is a adjustable parameter that is introduced to provide either a way of applying the rectangular barrier tunneling to a non-rectangular barrier tunneling system or an adjustment to account for the effective mass of the tunneling electrons through a rectangular barrier.

In the junction, the parameters of a, d and m were fixed. The ϕ, α were unkonw. By fitting the *I-V* curves we can obtain these parameters. The fitting minimization analysis was performed with the help of this equation:

$$\Delta(\phi_B, \alpha) = (\sum \left| I_{\exp V} - I_{cal,V} \right|^2)^{1/2}$$

The optimum parameter should result in minimized Δ. A program based on Mat Lab was written for this process.

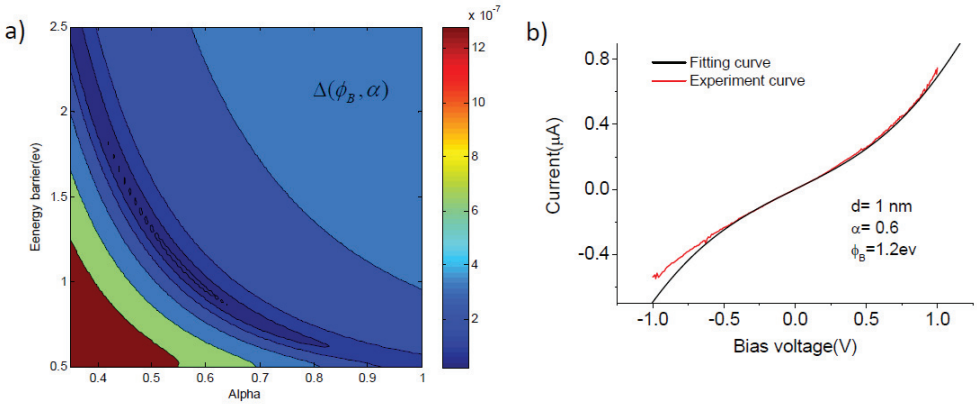

Figure C.1: (a) optimum parameter for fitting the *I/V* response of BDT was: $\alpha = 0.6$, ϕ_B=1.2 *ev* for BDT. (b) The fitted *I-V* curves with optimum parameters.

Program for Simmons fit based on Matlab

```
p0 = e1^2*power(4*pi^2*hbar,-1);
p1 = p0*(s1^2)/(d1^2);
p2 = -2*(2*m2*e1)^0.5/hbar;

dim = size(ndata);
dim1 = find(ndata(:,2)<0);
maxmum = max(ndata(dim1,2));
dim2 = find(ndata(:,2)==maxmum);

i=0;
for faib=f1:step:f2
    i=i+1;
    j=0;
    faib1(i) = faib;
    for alpha=a1:step1:a2
        j=j+1;
        k=0;
        k1=0;
        alpha1(j) = alpha;
        H(i,j) = 0.0;
        H1(i,j) = 0.0;
        for m = 1:dim2
            k=k+1;
            v=ndata(m,2);
            p4=faib-v/2;
```

```
            p5=faib+v/2;
            J(i,j,k) = p1*(p4*exp(p2*alpha*p4^0.5*d1)- ...
                p5*exp(p2*alpha*p5^0.5*d1));
            H(i,j) =  H(i,j) + power(J(i,j,k)-ndata(m,1),2);
        end
        for m = dim2+1:dim(1)
            k1=k1+1;
            v=ndata(m,2);
            p4=faib-v/2;
            p5=faib+v/2;
            J1(i,j,k1) = p1*(p4*exp(p2*alpha*p4^0.5*d1)- ...
                p5*exp(p2*alpha*p5^0.5*d1));
            H1(i,j) =  H1(i,j) + power(J1(i,j,k1)-ndata(m,1),2);
        end
        H(i,j) = sqrt(H(i,j));
        H1(i,j) = sqrt(H1(i,j));
    end
end

dim3 = size(H);
minimum = H(1,1);
m = 1;
n = 1;
for i=1:dim3(1)
    for j=1:dim3(2)
        if(minimum > H(i,j))
            minimum = H(i,j);
            m = i;
            n = j;
        end
    end
end

dim4 = size(H1);
minimum1 = H1(1,1);
m1 = 1;
n1 = 1;
for i=1:dim4(1)
    for j=1:dim4(2)
        if(minimum1 > H1(i,j))
            minimum1 = H1(i,j);
            m1 = i;
            n1 = j;
        end
    end
end

set(handles.edit13, 'String', faib1(1,m));
set(handles.edit15, 'String', alpha1(1,n));
set(handles.edit17, 'String', faib1(1,m1));
set(handles.edit19, 'String', alpha1(1,n1));
% If the variables with minimum value are more than one,
[p,q] = find(J==minimum);
[p1,q1] = find(J1==minimum1);

save matlab.mat;
```

```
figure(1);
hold on
plot(ndata(1:dim2,2),ndata(1:dim2,1),'b');
J2(1,:) = J(m,n,:);
plot(ndata(1:dim2,2),J2,'r');
xlabel('Bias voltage (V)');
ylabel('Tunneling current (A)');
title('\it{I-V curve}');

figure(2);
hold on
plot(ndata(dim2+1:dim(1),2),ndata(dim2+1:dim(1),1),'b');
J3(1,:) = J1(m1,n1,:);
plot(ndata(dim2+1:dim(1),2),J3,'r');
xlabel('Bias voltage (V)');
ylabel('Tunneling current (A)');
title('\it{I-V curve}');

v=[10^(-9), 10^(-8), 6*10^(-8), 1.6*10^(-7), 3.2*10^(-7), 6.4*10^(-7), 1*10^(-
6)];
figure(3);
contourf (alpha1(1,:),faib1(1,:), H, v);
xlabel('\alpha');
ylabel('\phi_{B} (eV)');
title('\it{\Delta(\phi_{B},\alpha)}');


figure(4);
contourf(alpha1(1,:),faib1(1,:),  H1, v);
xlabel('\alpha');
ylabel('\phi_{B} (ev)');
title('\it{\delta(\phi_{B},\alpha)}');
```

Appendix D

Abbreviation

I	Current
J	Current density
V	Voltage
R	Resistance
β	Tunneling Decay Constant
ϕ	Barrier Height
BE	Bioelectronic
AFM	Atomic Force Microscopy
BDT	Benzenedithiol
BDA	Benzenediamino
DFT	Density Function Theory
EBL	Electron Beam Lithography
GGA	Generalized Ggradient Approximation
MUA	Mercapto-undecanoic Acid

ODT	Octanedithiol
RIE	Reactive Ion Etching
SAM	Self-assembled Monolayers
SEM	Scanning Electron Microscopy
PDMS	Polydimethylsiloxane
PMMA	Poly(mehthylmethacrylate)
PVD	Physical Vapor Deposition
LDA	Local Density Approximation
ETOH	Ethanol
HOMO	Highest Occupied Molecular Orbital
LUMO	Lowest Unoccupied Molecular Orbital
SERS	Surface Enhanced Raman Spectroscopy
TERS	Tip Enhance Raman Spectroscopy
MCBJ	Mechanically Controllable Break Juncion
PECVD	Plasma Enhanced Chemical Vapor Deposition
MATLAB	Matrix Laboratory
C2-NTA	3,3'-dithiobis[N -(5-amino-5-carboxypentyl)propionamide-N',N' –diacetic acid] dihydrochloride

Reference List

1. Aviram, A.; Ratner, M. A. *Chemical Physics Letters* **1974,** *29* (2), 277-283.

2. Chen, F.; Hihath, J.; Huang, Z. F.; Li, X. L.; Tao, N. J. *Annual Review of Physical Chemistry* **2007,** *58*, 535-564.

3. Dujardin, E.; Derycke, V.; Goffman, M. F.; Lefevre, R.; Bourgoin, J. P. *Applied Physics Letters* **2005,** *87* (19).

4. Haiss, W.; Albrecht, T.; van Zalinge, H.; Higgins, S. J.; Bethell, D.; Hobenreich, H.; Schiffrin, D. J.; Nichols, R. J.; Kuznetsov, A. M.; Zhang, J.; Chi, Q.; Ulstrup, J. *Journal of Physical Chemistry B* **2007,** *111* (24), 6703-6712.

5. Liu, K.; Wang, X. H.; Wang, F. S. *Acs Nano* **2008,** *2* (11), 2315-2323.

6. York, R. L.; Slowinski, K. *Journal of Electroanalytical Chemistry* **2003,** *550*, 327-336.

7. Nishino, T.; Negishi, R.; Kawao, M.; Nagata, T.; Ozawa, H.; Ishibashi, K. *Nanotechnology* **2010,** *21* (22).

8. Yu, H. Y.; Ah, C. S.; Baek, I. B.; Kim, A.; Yang, J. H.; Ahn, C. G.; Park, C. W.; Kim, B. H. *Etri Journal* **2009,** *31* (4), 351-356.

9. Martin, S.; Giustiniano, F.; Haiss, W.; Higgins, S. J.; Whitby, R. J.; Nichols, R. J. *Journal of Physical Chemistry C* **2009,** *113* (43), 18884-18890.

10. Park, C. W.; Lim, J. W.; Yu, H. Y.; Pi, U. H.; Ryu, M. K.; Choi, S. Y. *Japanese Journal of Applied Physics Part 1-Regular Papers Brief Communications & Review Papers* **2006,** *45* (5A), 4293-4295.

11. Zhao, Y.; Chu, J.; Li, S. H.; Chen, Y.; Sheng, G. P.; Chen, Y. P.; Li, W. W.; Liu, G.; Tian, Y. C.; Xiong, Y.; Yu, H. Q. *Chemical Engineering Journal* **2011,** *170* (2-3), 440-444.

12. Baik, J. M.; Lee, S. J.; Moskovits, M. *Nano Letters* **2009,** *9* (2), 672-676.

13. French, R. W.; Marken, F. *Journal of Solid State Electrochemistry* **2009,** *13* (4), 609-617.

14. Baik, J. M.; Lee, S. J.; Moskovits, M. *Nano Letters* **2009,** *9* (2), 672-676.

15. Voets, J.; Keijsers, R. J. P.; Shklyarevskii, O. I.; vanKempen, H. *Physical Review B* **1996,** *53* (3), 1072-1075.

16. Zhou, C.; Muller, C. J.; Deshpande, M. R.; Sleight, J. W.; Reed, M. A. *Applied Physics Letters* **1995,** *67* (8), 1160-1162.

17. Liu, S. P.; Weisbrod, S. H.; Tang, Z.; Marx, A.; Scheer, E.; Erbe, A. *Angewandte Chemie-International Edition* **2010,** *49* (19), 3313-3316.

18. Taniguchi, M.; Tsutsui, M.; Yokota, K.; Kawai, T. *Nanotechnology* **2009,** *20* (43).

19. Parks, J. J.; Champagne, A. R.; Hutchison, G. R.; Flores-Torres, S.; Abruna, H. D.; Ralph, D. C. *Physical Review Letters* **2007,** *99* (2).

20. Fernandez-Seivane, L.; Garcia-Suarez, V. M.; Ferrer, J. *Physical Review B* **2007,** *75* (7).

21. Tian, J. H.; Liu, B.; Li, X. L.; Yang, Z. L.; Ren, B.; Wu, S. T.; Tao, N. J.; Tian, Z. Q. *Journal of the American Chemical Society* **2006,** *128* (46), 14748-14749.

22. Kolesnychenko, O. Y.; Toonen, A. J.; Shklyarevskii, O. I.; van Kempen, H. *Applied Physics Letters* **2001,** *79* (17), 2707-2709.

23. Bezrukov, S. M.; Winterhalter, M. *Physical Review Letters* **2000,** *85* (1), 202-205.

24. Djukic, D.; van Ruitenbeek, J. M. *Nano Letters* **2006,** *6*, 789-793.

25. Kornyshev, A. A.; Kuznetsov, A. M. *Journal of Physics-Condensed Matter* **2008,** *20* (37).

26. Ochs, R.; Secker, D.; Elbing, M.; Mayor, M.; Weber, H. B. *Faraday Discussions* **2006,** *131*, 281-289.

27. Seeker, D.; Weber, H. B. *Physica Status Solidi B-Basic Solid State Physics* **2007,** *244* (11), 4176-4180.

28. Solomon, G. C.; Gagliardi, A.; Pecchia, A.; Frauenheim, T.; Di Carlo, A.; Reimers, J. R.; Hush, N. S. *Nano Letters* **2006,** *6*, 2431-2437.

29. Wu, Z. M.; Wu, S. M.; Oberholzer, S.; Steinacher, M.; Calame, M.; Schonenberger, C. *Physical Review B* **2008,** *78* (23).

30. Ochs, R.; Secker, D.; Elbing, M.; Mayor, M.; Weber, H. B. *Faraday Discussions* **2006,** *131*, 281-289.

31. Nitzan, A.; Ratner, M. A. *Science* **2003,** *300* (5624), 1384-1389.

32. Cui, X. D.; Primak, A.; Zarate, X.; Tomfohr, J.; Sankey, O. F.; Moore, A. L.; Moore, T. A.; Gust, D.; Harris, G.; Lindsay, S. M. *Science* **2001,** *294* (5542), 571-574.

33. Kushmerick, J. G.; Naciri, J.; Yang, J. C.; Shashidhar, R. *Nano Letters* **2003,** *3* (7), 897-900.

34. Wang, G.; Kim, T. W.; Jo, G.; Lee, T. *Journal of the American Chemical Society* **2009,** *131* (16), 5980-5985.

35. Frederiksen, T.; Munuera, C.; Ocal, C.; Brandbyge, M.; Paulsson, M.; Sanchez-Portal, D.; Arnau, A. *Acs Nano* **2009,** *3* (8), 2073-2080.

36. Bala, T.; Prasad, B. L. V.; Sastry, M.; Kahaly, M. U.; Waghmare, U. V. *Journal of Physical Chemistry A* **2007,** *111* (28), 6183-6190.

37. Ramasarma, T. *Indian Journal of Biochemistry & Biophysics* **1999,** *36* (6), 379-397.

38. Albrecht, T.; Guckian, A.; Ulstrup, J.; Vos, J. G. *Nano Letters* **2005,** *5* (7), 1451-1455.

39. Parks, J. J.; Champagne, A. R.; Costi, T. A.; Shum, W. W.; Pasupathy, A. N.; Neuscamman, E.; Flores-Torres, S.; Cornaglia, P. S.; Aligia, A. A.; Balseiro, C. A.; Chan, G. K. L.; Abruna, H. D.; Ralph, D. C. *Science* **2010,** *328* (5984), 1370-1373.

40. Levesque, J.; Zeidler, D.; Marangos, J.; Corkum, P.; Villeneuve, D. *Physical Review Letters* **2007,** *98* (18).

41. Maruyama, T.; Machida, Y.; Sugatani, S.; Tsuchikawa, H.; Hoshino, H.; Ito, M.; Tago, H.; Chau, L. L.; Lee, S.; Komami, H. *Journal of Vacuum Science & Technology B* **2009,** *27* (6), 2532-2536.

42. Gorelick, S.; Guzenko, V. A.; Vila-Comamala, J.; David, C. *Nanotechnology* **2010,** *21* (29).

43. Ingino, J.; Owen, G.; Berglund, C. N.; Browning, R.; Pease, R. F. W. *Journal of Vacuum Science & Technology B* **1994,** *12* (3), 1367-1371.

44. Minagawa, S.; Saito, T.; Gejyo, T. *Journal of the American Ceramic Society* **1968,** *51* (9), 532-&.

45. Pearce, M. L.; Marek, R. W. *Journal of the American Ceramic Society* **1968,** *51* (2), 84-&.

46. Pearce, M. L.; Marek, R. W. *Journal of the American Ceramic Society* **1968,** *51* (6), 355-&.

47. Feuerstein, A.; Knapp, J.; Taylor, T.; Ashary, A.; Bolcavage, A.; Hitchman, N. *Journal of Thermal Spray Technology* **2008,** *17* (2), 199-213.

48. Birnbaum, K.; Gutknecht, N. *Lasers in Medical Science* **2010,** *25* (4), 595-603.

49. Jepson, M.; Liu, X.; Bell, D.; Ferranti, D.; Inkson, B.; Rodenburg, C. *Microscopy and Microanalysis* **2011,** *17* (4), 637-642.

50. Hush, N. S. *Molecular Electronics Iii* **2003,** *1006*, 1-20.

51. Evans, M. G.; Gergely, J. *Biochimica et Biophysica Acta* **1949,** *3* (2), 188-197.

52. Chen, J.; Reed, M. A.; Rawlett, A. M.; Tour, J. M. *Science* **1999,** *286* (5444), 1550-1552.

53. Wang, W. Y.; Lee, T.; Reed, M. A. *Reports on Progress in Physics* **2005,** *68* (3), 523-544.

54. von Wrochem, F.; Gao, D. Q.; Scholz, F.; Nothofer, H. G.; Nelles, G.; Wessels, J. M. *Nature Nanotechnology* **2010,** *5* (8), 618-624.

55. Maltsev, Y. U. S.; Shevchenko, V. D.; Chernin, M. M. Thermal relay|uses gas heating and cooling within thermocouple junctions to displace contact closing mercury droplet. SU917223-B.

56. Bratkovski, A. M.; Kornilovich, P.; Williams, R. S.; Zhang, X. Bistable molecule for crossed-wire device, is present in at least one connector species of crossed-wire device. US2002130317-A1; US6624002-B2.

57. Bratkovski, A. M.; Kornilovich, P.; Williams, R. S.; Zhang, X. New bistable molecule for use in forming micro-scale or nano-scale crossed-wire device. US2003089920-A1.

58. Bratkovski, A.; Zhang, X.; Williams, R. S.; Bratovski, A. Stabilization of configurable molecular switchable devices in cross-bar geometry involves providing junction with

connector species having molecule of active dipole(s). US2002113229-A1; KR2003061850-A; US6663797-B2.

59. Kushmerick, J. G.; Naciri, J.; Yang, J. C.; Shashidhar, R. *Nano Letters* **2003,** *3* (7), 897-900.

60. Bergren, A. J.; Harris, K. D.; Deng, F. J.; McCreery, R. L. *Journal of Physics-Condensed Matter* **2008,** *20* (37).

61. Joachim, C.; Gimzewski, J. K. *Chemical Physics Letters* **1997,** *265* (3-5), 353-357.

62. Guisinger, N. P.; Greene, M. E.; Basu, R.; Baluch, A. S.; Hersam, M. C. *Nano Letters* **2004,** *4* (1), 55-59.

63. Qiu, X. H.; Nazin, G. V.; Ho, W. *Physical Review Letters* **2004,** *93* (19).

64. Piva, P. G.; DiLabio, G. A.; Pitters, J. L.; Zikovsky, J.; Rezeq, M.; Dogel, S.; Hofer, W. A.; Wolkow, R. A. *Nature* **2005,** *435*, 658-661.

65. Krans, J. M.; Vanruitenbeek, J. M.; Fisun, V. V.; Yanson, I. K.; Dejongh, L. J. *Nature* **1995,** *375* (6534), 767-769.

66. Muller, C. J.; Vanruitenbeek, J. M.; Dejongh, L. J. *Physica C* **1992,** *191* (3-4), 485-504.

67. Zhou, C.; Muller, C. J.; Deshpande, M. R.; Sleight, J. W.; Reed, M. A. *Applied Physics Letters* **1995,** *67* (8), 1160-1162.

68. Holmlin, R. E.; Haag, R.; Chabinyc, M. L.; Ismagilov, R. F.; Cohen, A. E.; Terfort, A.; Rampi, M. A.; Whitesides, G. M. *Journal of the American Chemical Society* **2001,** *123* (21), 5075-5085.

69. Beebe, J. M.; Kim, B.; Gadzuk, J. W.; Frisbie, C. D.; Kushmerick, J. G. *Physical Review Letters* **2006,** *97* (2).

70. Beebe, J. M.; Kim, B.; Frisbie, C. D.; Kushmerick, J. G. *Acs Nano* **2008,** *2* (5), 827-832.

71. Huisman, E. H.; Guedon, C. M.; van Wees, B. J.; van der Molen, S. J. *Nano Letters* **2009,** *9* (11), 3909-3913.

72. Lo, H. Y.; Li, Y.; Chao, H. Y.; Tsai, C. H.; Pan, F. M. *Nanotechnology* **2007,** *18*.

73. Chiu, P. W.; Roth, S. *Applied Physics Letters* **2008,** *92* (4).

74. Kiguchi, M.; Miura, S.; Takahashi, T.; Hara, K.; Sawamura, M.; Murakoshi, K. *Journal of Physical Chemistry C* **2008,** *112* (35), 13349-13352.

75. Zhou, C.; Deshpande, M. R.; Reed, M. A.; Jones, L.; Tour, J. M. *Applied Physics Letters* **1997,** *71* (5), 611-613.

76. Zhou, C.; Deshpande, M. R.; Reed, M. A.; Jonesll, L.; Tour, J. M. *Applied Physics Letters* **1997,** *71* (19), 2857.

77. Luo, K.; Chae, D. H.; Yao, Z. *Nanotechnology* **2007,** *18*.

78. Choi, S. H.; Kim, B.; Frisbie, C. D. *Science* **2008,** *320* (5882), 1482-1486.

79. Pernicone, N. C.; Geri, J. B.; York, J. T. *Journal of Chemical Education* **2011,** *88* (9), 1323-1327.

80. Varadwaj, P. R.; Cukrowski, I.; Perry, C. B.; Marques, H. M. *Journal of Physical Chemistry A* **2011,** *115* (24), 6629-6640.

81. Klokishner, S. I.; Reu, O.; Chan-Thaw, C. E.; Jentoft, F. C.; Schloegl, R. *Journal of Physical Chemistry A* **2011,** *115* (28), 8100-8112.

82. Zheng, K. C.; Wang, J. P.; Shen, Y.; Kuang, D. B.; Yun, F. C. *Journal of Physical Chemistry A* **2001,** *105* (30), 7248-7253.

83. Parker, J. F.; Kacprzak, K. A.; Lopez-Acevedo, O.; Hakkinen, H.; Murray, R. W. *Journal of Physical Chemistry C* **2010,** *114* (18), 8276-8281.

84. Bosman, G.; Zijlstra, R. J. J. *Solid-State Electronics* **1982,** *25* (4), 273-280.

85. Rogers, C. T.; Buhrman, R. A. *Physical Review Letters* **1984,** *53* (13), 1272-1275.

86. Guise, O. L.; Ahner, J. W.; Jung, M. C.; Goughnour, P. C.; Yates, J. T. *Nano Letters* **2002,** *2* (3), 191-193.

87. Sorensen, A. H.; Hvid, U.; Mortensen, M. W.; Morch, K. A. *Review of Scientific Instruments* **1999,** *70* (7), 3059-3067.

88. Park, J.; Hong, T.; Lee, N.; Kim, K.; Seo, Y. *Current Applied Physics* **2011,** *11* (6), 1332-1336.

89. Macdonald, J. R.; Barlow, C. A. *Journal of Chemical Physics* **1962,** *36* (11), 3062-&.

90. Zhou, C.; Muller, C. J.; Deshpande, M. R.; Sleight, J. W.; Reed, M. A. *Applied Physics Letters* **1995,** *67* (8), 1160-1162.

91. Gruter, L.; Gonzalez, M. T.; Huber, R.; Calame, M.; Schonenberger, C. *Small* **2005,** *1* (11), 1067-1070.

92. Kang, Z. Y.; Song, H.; Yang, Z. M.; Ding, B. J. *Rare Metal Materials and Engineering* **2005,** *34* (5), 680-683.

93. Xiao, X. Y.; Xu, B. Q.; Tao, N. J. *Nano Letters* **2004,** *4*, 267-271.

94. Kiguchi, M.; Miura, S.; Takahashi, T.; Hara, K.; Sawamura, M.; Murakoshi, K. *Journal of Physical Chemistry C* **2008,** *112* (35), 13349-13352.

95. Reddy, P.; Jang, S. Y.; Segalman, R. A.; Majumdar, A. *Science* **2007,** *315* (5818), 1568-1571.

96. Song, H.; Kim, Y.; Jang, Y. H.; Jeong, H.; Reed, M. A.; Lee, T. *Nature* **2009,** *462* (7276), 1039-1043.

97. Kim, Y.; Song, H.; Kim, D.; Lee, T.; Jeong, H. *Acs Nano* **2010,** *4* (8), 4426-4430.

98. Chang, S. A.; He, J.; Lin, L. S.; Zhang, P. M.; Liang, F.; Young, M.; Huang, S.; Lindsay, S. *Nanotechnology* **2009,** *20* (18).

99. Kihira, Y.; Shimada, T.; Matsuo, Y.; Nakamura, E.; Hasegawa, T. *Nano Letters* **2009,** *9* (4), 1442-1446.

100. Mishchenko, A.; Vonlanthen, D.; Meded, V.; Burkle, M.; Li, C.; Pobelov, I. V.; Bagrets, A.; Viljas, J. K.; Pauly, F.; Evers, F.; Mayor, M.; Wandlowski, T. *Nano Letters* **2010,** *10* (1), 156-163.

101. Landau, L. D.; Lifshits, E. M. *Doklady Akademii Nauk Sssr* **1955,** *100* (4), 669-672.

102. Scott, A. M.; Miura, T.; Ricks, A. B.; Dance, Z. E., X; Giacobbe, E. M.; Colvin, M. T.; Wasielewski, M. R. *Journal of the American Chemical Society* **2009,** *131* (48), 17655-17666.

103. Augustyn, K. E.; Merino, E. J.; Barton, J. K. *Proceedings of the National Academy of Sciences of the United States of America* **2007,** *104* (48), 18907-18912.

104. Sheu, S. Y.; Schlag, E. W.; Yang, D. Y.; Selzle, H. L. *Journal of Physical Chemistry A* **2001,** *105* (26), 6353-6361.

105. Song, H.; Lee, H.; Lee, T. *Journal of the American Chemical Society* **2007,** *129* (13), 3806-+.

106. Xu, B. Q. *Small* **2007,** *3* (12), 2061-2065.

107. Basch, H.; Ratner, M. A. *Journal of Chemical Physics* **2004,** *120* (12), 5761-5770.

108. Kan, R. R.; Liu, H. M.; Ye, Y. F.; Li, P.; Yin, X.; Zhao, J. W. *Acta Physico-Chimica Sinica* **2007,** *23* (5), 671-675.

109. Gao, W.; Zhao, M.; Jiang, Q. *Applied Surface Science* **2009,** *255* (22), 9259-9263.

110. Chen, F.; Li, X. L.; Hihath, J.; Huang, Z. F.; Tao, N. J. *Journal of the American Chemical Society* **2006,** *128* (49), 15874-15881.

111. Chen, I. W. P.; Fu, M. D.; Tseng, W. H.; Yu, J. Y.; Wu, S. H.; Ku, C. J.; Chen, C. H.; Peng, S. M. *Angewandte Chemie-International Edition* **2006,** *45* (35), 5814-5818.

112. Anderegg, G. *Pure and Applied Chemistry* **1982,** *54* (12), 2693-2758.

113. Choi, K. Y.; Choi, S. N.; Hong, C. P. *Journal of Inclusion Phenomena and Macrocyclic Chemistry* **2001,** *40* (1-2), 67-71.

114. Conti, M.; Falini, G.; Samori, B. *Angewandte Chemie-International Edition* **2000,** *39* (1), 215-+.

115. Whitlow, S. H. *Acta Crystallographica Section B-Structural Crystallography and Crystal Chemistry* **1972,** *B 28* (6), 1914-&.

116. Mayer, D.; Ataka, K.; Heberle, J.; Offenhausser, A. *Langmuir* **2005,** *21* (19), 8580-8583.

117. Perdew, J. P.; Wang, Y. *Physical Review B* **1992,** *45* (23), 13244-13249.

118. Cho, S. H.; Han, H. S.; Jang, D. J.; Kim, K.; Kim, M. S. *Journal of Physical Chemistry* **1995,** *99* (26), 10594-10599.

119. Griffith, W. P.; Koh, T. Y. *Spectrochimica Acta Part A-Molecular and Biomolecular Spectroscopy* **1995,** *51* (2), 253-267.

120. Gao, P.; Weaver, M. J. *Journal of Physical Chemistry* **1985,** *89* (23), 5040-5046.

121. Haynes, C. L.; Yonzon, C. R.; Zhang, X. Y.; Van Duyne, R. P. *Journal of Raman Spectroscopy* **2005,** *36* (6-7), 471-484.

122. Kandori, H.; Kinoshita, N.; Shichida, Y.; Maeda, A.; Needleman, R.; Lanyi, J. K. *Journal of the American Chemical Society* **1998,** *120* (23), 5828-5829.

123. Haynes, C. L.; Van Duyne, R. P. *Journal of Physical Chemistry B* **2003,** *107* (30), 7426-7433.

124. Joo, S. W.; Han, S. W.; Kim, K. *Journal of Colloid and Interface Science* **2001,** *240* (2), 391-399.

125. Lim, J. K.; Kwon, O.; Joo, S. W. *Journal of Physical Chemistry C* **2008,** *112* (17), 6816-6821.

126. Wang, W. Y.; Lee, T.; Reed, M. A. *Reports on Progress in Physics* **2005,** *68* (3), 523-544.

1. **Soft Matter**
   From Synthetic to Biological Materials
   Lecture manuscripts of the 39th IFF Spring School March 3 – 14, 2008
   Jülich, Germany
   edited by J.K.G. Dhont, G. Gompper, G. Nägele, D. Richter, R.G. Winkler (2008),
   c. 1000 pages
   ISBN: 978-3-89336-517-3

2. **Structural analysis of diblock copolymer nanotemplates using grazing incidence scattering**
   by D. Korolkov (2008), III, 167 pages
   ISBN: 978-3-89336-522-7

3. **Thermal Nonequilibrium**
   Thermal forces in fluid mixtures
   Lecture Notes of the 8th International Meeting on Thermodiffusion,
   9 – 13 June 2008, Bonn, Germany
   edited by S. Wiegand, W. Köhler (2008), 300 pages
   ISBN: 978-3-89336-523-4

4. **Synthesis of CMR manganites and ordering phenomena in complex transition metal oxides**
   by H. Li (2008), IV, 176 pages
   ISBN: 978-3-89336-527-2

5. **Neutron Scattering**
   Lectures of the JCNS Laboratory Course held at the Forschungszentrum Jülich and the research reactor FRM II of TU Munich
   edited by R. Zorn, Th. Brückel, D. Richter (2008), ca. 500 pages
   ISBN: 978-3-89336-532-6

6. **Ultrafast Magnetization Dynamics**
   by S. Woodford (2008), 130 pages
   ISBN: 978-3-89336-536-4

7. **Role of Surface Roughness inTribology: from Atomic to Macroscopic Scale**
   by C. Yang (2008), VII, 166 pages
   ISBN: 978-3-89336-537-1

8. **Strahl- und Spindynamik von Hadronenstrahlen in Mittelenergie-Ringbeschleunigern**
   von A. Lehrach (2008), II, 171 Seiten
   ISBN: 978-3-89336-548-7

9. **Phase Behaviour of Proteins and Colloid-Polymer Mixtures**
   by C. Gögelein (2008), II, 147 pages
   ISBN: 978-3-89336-555-5

10. **Spintronics – From GMR to Quantum Information**
    Lecture Notes of the 40th IFF Spring School March 9 – 20, 2009
    Jülich, Germany
    edited by St. Blügel, D. Bürgler, M. Morgenstern, C. M. Schneider,
    R. Waser (2009), c. 1000 pages
    ISBN: 978-3-89336-559-3

11. **ANKE / PAX Workshop on SPIN Physics**
    JINR, Dubna, Russia / June 22. – 26, 2009
    Org. Committee: A. Kacharava, V. Komarov, A. Kulikov, P. Lenisa, R. Rathmann,
    H. Ströher (2009), CD-ROM
    ISBN: 978-3-89336-586-9

12. **Entwicklung einer Nanotechnologie-Plattform für die Herstellung Crossbar-basierter Speicherarchitekturen**
    von M. Meier (2009), 135 Seiten
    ISBN: 978-3-89336-598-2

13. **Electronic Oxides –**
    Correlation Phenomena, Exotic Phases and Novel Functionalities
    Lecture Notes of the 41st IFF Spring School March 8 – 19, 2010
    Jülich, Germany
    edited by St. Blügel, T. Brückel, R. Waser, C.M. Schneider (2010), ca. 1000 pages
    ISBN: 978-3-89336-609-5

14. **4th Georgian-German School and Workshop in Basic Science**
    Tbilisi, Georgia / May 3 – 7, 2010
    Org. Committee: E. Abrosimova, R. Botchorishvili, A. Kacharava, M. Nioradze,
    A. Prangishvili, H. Ströher (2010); CD-ROM
    ISBN: 978-3-89336-629-3

15. **Neutron Scattering**
    Lectures of the JCNS Laboratory Course held at Forschungszentrum Jülich and the research reactor FRM II of TU Munich
    edited by Th. Brückel, G. Heger, D. Richter, G. Roth and R. Zorn (2010),
    ca 350 pages
    ISBN: 978-3-89336-635-4

16. **Ab *initio* investigations of magnetic properties of ultrathin transition-metal films on *4d* substrates**
    by A. Al-Zubi (2010), II, 143 pages
    ISBN: 978-3-89336-641-5

17. **Investigation of a metal-organic interface realization and understanding of a molecular switch**
    by O. Neucheva (2010), 134 pages
    ISBN: 978-3-89336-650-7

18. **Reine Spinströme in lateralen Spinventilen, *in situ* Erzeugung und Nachweis**
von J. Mennig (2010), V, 95 Seiten
ISBN: 978-3-89336-684-2

19. **Nanoimprint Lithographie als Methode zur chemischen Oberflächenstrukturierung für Anwendungen in der Bioelektronik**
von S. Gilles (2010), II, 169 Seiten
ISBN: 978-3-89336-686-6

20. **Macromolecular Systems in Soft- and Living-Matter**
Lecture Notes of the 42nd IFF Spring School 2011 February 14 – 25, 2011 Jülich, Germany
edited by J. K.G. Dhont, G. Gompper, P. R.Lang, D. Richter, M. Ripoll, D. Willbold, R. Zorn (2011), ca. 1000 pages
ISBN: 978-3-89336-688-0

21. **The spin structure of magnetic nanoparticles and in magnetic nanostructures**
by S. Disch (2011), V, 342 pages
ISBN: 978-3-89336-704-7

22. **Element-selective and time-resolved magnetic investigations in the extreme ultraviolet range**
by P. Grychtol (2011), xii, 144 pages
ISBN: 978-3-89336-706-1

23. **Spin-Transfer Torque Induced Dynamics of Magnetic Vortices in Nanopillars**
by V. Sluka (2011), 121 pages
ISBN: 978-3-89336-717-7

24. **Adsorption von Phthalocyaninen auf Edelmetalloberflächen**
von I. Kröger (2011), vi, 206 Seiten
ISBN: 978-3-89336-720-7

25. **Time-Resolved Single Molecule FRET Studies on Folding/Unfolding Transitions and on Functional Conformational Changes of Phosphoglycerate Kinase**
by T. Rosenkranz (2011), III, 139 pages
ISBN: 978-3-89336-721-4

26. **NMR solution structures of the MIoK1 cyclic nucleotide-gated ion channel binding domain**
by S. Schünke (2011), VI, (getr. pag.)
ISBN: 978-3-89336-722-1

27. **Neutron Scattering**
Lectures of the JCNS Laboratory Course held at Forschungszentrum Jülich and the research reactor FRM II of TU Munich
edited by Th. Brückel, G. Heger, D. Richter, G. Roth and R. Zorn (2011), ca 350 pages
ISBN: 978-3-89336-725-2

28. **Neutron Scattering**
Experiment Manuals of the JCNS Laborator Course held at Forschungszentrum Jülich and the research reactorFRM II of TU Munich
edited by Th. Brückel, G. Heger, D. Richter, G. Roth and R. Zorn (2011), ca. 180 pages
ISBN: 978-3-89336-726-9

29. **Silicon nanowire transistor arrays for biomolecular detection**
by X.T.Vu (2011), vii, 174 pages
ISBN: 978-3-89336-739-9

30. **Interactions between parallel carbon nanotube quantum dots**
by K. Goß (2011), viii, 139 pages
ISBN: 978-3-89336-740-5

31. **Effect of spin-orbit scattering on transport properties of low-dimensional dilute alloys**
by S. Heers (2011), viii, 216 pages
ISBN: 978-3-89336-747-4

32. **Charged colloids and proteins: Structure, diffusion, and rheology**
by M. Heinen (2011), xii, 186 pages
ISBN: 978-3-89336-751-1

33. **Scattering Methods for Condensed Matter Research: Towards Novel Applications at Future Sources**
Lecture Notes of the 43rd IFF Spring School 2012
March 5 – 16, 2012 Jülich, Germany
edited by M. Angst, T. Brückel, D. Richter, R. Zorn ca. 1000 pages
ISBN: 978-3-89336-759-7

34. **Single-Site Green Function of the Dirac Equation for Full-Potential Electron Scattering**
by P. Kordt (2012), 138 pages
ISBN: 978-3-89336-760-3

35. **Time Resolved Single Molecule Fluorescence Spectroscopy on Surface Tethered and Freely Diffusing Proteins**
by D. Atta (2012), iv, 126 pages
ISBN: 978-3-89336-763-4

36. **Fabrication and Utilization of Mechanically Controllable Break Junction for Bioelectronics**
by D. Xiang (2012), 129 pages
ISBN: 978-3-89336-769-6

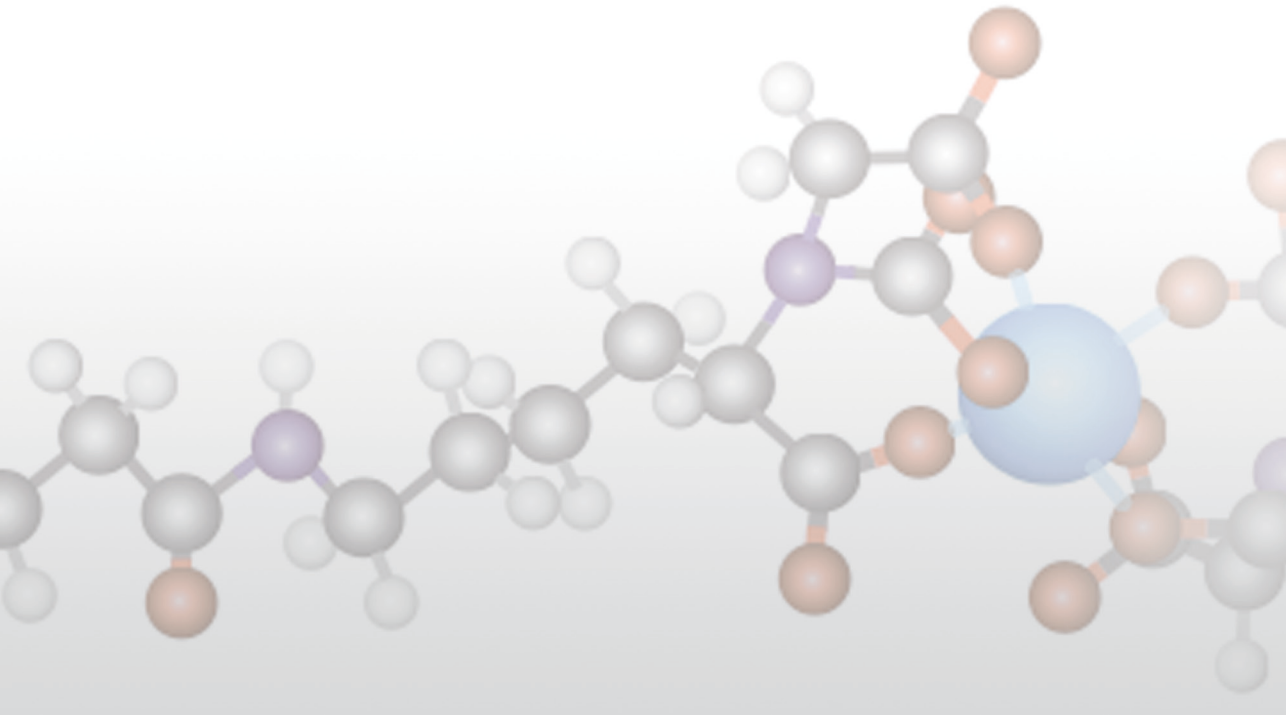

Schlüsseltechnologien / Key Technologies
Band / Volume 36
ISBN 978-3-89336-769-6

JÜLICH
FORSCHUNGSZENTRUM